Detection of Smoke and Dust Aerosols Using Multi-sensor Satellite Remote Sensing
Measurements

A dissertation submitted in partial fulfillment of the requirements for the degree of
Doctor of Philosophy at George Mason University

By

Yong Xie
Master of Electronics
Nanjing Normal University, P. R. China, 2004

Co-Director: Dr. John J. Qu, Associate Professor
Co-director: Dr. Jack Xiong
Department of Geography and GeoInformation Sciences

Spring Semester 2009
George Mason University
Fairfax, VA

DEDICATION

This is dedicated to my family, who offered me unconditional love and support throughout the course of this dissertation.

ACKNOWLEDGEMENTS

TABLE OF CONTENTS

LIST OF TABLES

LIST OF FIGURES

LIST OF ABBREVIATIONS

AI	Aerosol Index
AOD	Aerosol Optical Depth
AOT	Aerosol Optical Thickness
ASTER	Advanced Spaceborne Thermal Emission and Reflection Radiometer
ATBD	Algorithm Theoretical Basis Documents
AVHRR	Advanced Very High Resolution Radiometer
BBR	Band-to-Band Registration
BT	Bright Temperature
BTD	Bright Temperature Difference
CALIPSO	Cloud-Aerosol Lidar and Infrared Pathfinder Satellite Observation
EOS	Earth Observing System
FPA	Focal Plane Assemblies
IFOV	Instantaneous Field Of View
MCST	MODIS Characterization Support Team
MISR	Multiangle Imaging SpectroRadiometer
MODIS	MODoderate resolution Imaging Spectroradiometer
NASA	National Aeronautics and Space Administration
NDDI	Normalized Difference Dust Index
NDSI	Normalized Difference Snow Index
NDVI	Normalized Difference Vegetation Index
NMDI	Normalized Multi-band Drought Index
NI	Normalized Index
NIR	Near Infrared
L1B	Level 1B
LWIR	Long Wavelength Infrared
OMI	Ozone Monitoring Instrument
RGB	Red, Blue, Green
RSB	Reflective Solar Band
SIS	Spherical Integration Source
SMIR	Short- and Middle- Wavelength Infrared
SWIR	Short Wavelength Infrared
SRCA	The Spectro-Radiometric Calibration Assembly
SZA	Solar Zenith Angle
TEB	Thermal Emissive Band
UVAI	UV Aerosol Index

VFM	Vertical Feature Mask
VIS	Visible
VNIR	Visible-Near Infrared

ABSTRACT

DETECTION OF SMOKE AND DUST AEROSOLS USING MULTI-SENSOR SATELLITE REMOTE SENSING MEASUREMENTS

Yong Xie, Ph.D.

George Mason University, 2009

Co-Dissertation Director: Dr. John J. Qu ; Dr. Jack Xiong

Every year a large amount of aerosols released from wildfires and dust storms into the atmosphere may have potential impacts on the climate, environment, and air quality. Detecting smoke and dust aerosols and monitoring their movements and evolutions in a timely manner is a very meaningful task. Satellite remote sensing has been demonstrated as an effective means for the observation of these two kinds of aerosols. In this dissertation, an algorithm based on the multi-spectral technique for detecting smoke and dust aerosols is developed, by combining measurements of MODoderate resolution Imaging Spectroradiometer (MODIS) reflective solar bands and thermal emissive bands.

Data from smoke/dust events occurred during last several years are collected visually as training data for spectral and statistical analyses. According to the spectral curves of various scene types (aerosols, cloud, vegetation, and water et al.), a series of spectral bands is selected jointly or separately and corresponding thresholds are defined for scene classification step by step. The multi-spectral algorithm is applied mainly to detect smoke plumes in the United States and dust storms in Asia. The detection results

are validated not only visually with MODIS true color images, but also quantitatively with products of, Ozone Monitoring Instrument (OMI) and Cloud-Aerosol Lidar and Infrared Pathfinder Satellite Observation (CALIPSO). The validations show that this multi-spectral detection algorithm is suitable to monitor smoke and dust in the selected study areas. The accuracy is quite good in most cases. Additionally, this algorithm can be used to detect smoke and dust aerosols at the areas near clouds even mixed with clouds.

Detection of dust aerosol with multi-sensor satellite remote sensing measurements, MODIS and CALIPSO, is also performed tentatively in this dissertation. After spatial registration, the dust layers are identified combining CALIPSO Vertical Feature Mask product and measurements of MODIS brightness temperature difference between 12 and 11-µm bands. Based on detecting results, the three-dimension information of dust aerosols is summarized.

Additionally, the impacts of the mis-registration on the L1B data and dust aerosol detection results are assessed. The relative errors caused by mis-registration on L1B data are generally less than a few tenths of a percent. The impacts on dust detection results are relative large, usually has the trend as negligible at the homogeneous and semi-homogeneous areas, but large at the non-homogeneous areas.

CHAPTER 1

INTRODUCTION

This dissertation is aiming to develop a multi-spectral algorithm for detecting smoke and dust aerosols in a timely manner with MODoderate resolution Imaging Spectroradiometer (MODIS) measurements. According to the spectral and statistical analyses, a new combination of multiple visible (VIS), near infrared (NIR), and short- and long-wave infrared bands is selected for smoke and dust detections. The results are validated not only visually with MODIS RGB (Red, Green, and Blue) true color images, but also quantitatively with multi-sensor measurements, such as Ozone Monitoring Instrument (OMI) and Cloud-Aerosol Lidar and Infrared Pathfinder Satellite Observation (CALIPSO). On the other hand, detection of dust and smoke with multi-sensor measurements, MODIS and CALIPSO, is also executed in this dissertation. The three dimensional information of dust aerosol is obtained by combining both sensors' measurements. Additionally, sensitivity analysis is performed to estimate the impact of MODIS spatial characterization change on Level 1B (L1B) measurements and dust detection results.

1.1 Importance of Studying Smoke and Dust Aerosols

The study of atmospheric aerosols has become a very interesting topic in recent years because of the evidence of their impacts on climate change (Estelles et al., 2007). The aerosol, deserving the same consideration as greenhouse gases, plays important roles in atmospheric chemistry, cloud microphysics, temperature, and radiation balance in the lower atmosphere (Li et al., 2001). Smoke from wildfires and dust storm are two kinds of frequently occurred natural phenomena over the continents. They may have potential impacts on the climate, environment, and air quality. Particulate matter from smoke is the major pollutant of concern, which is a general term for a mixture of solid particles and liquid droplets found in the air.

Dust storm, usually aroused in arid and semi-arid regions, can carry large quantity of dust and move forward like an overwhelming tide to destroy crop plants, ruin the mining and communication facilities, weather vestiges, damage small villages, reduce visibility and human's daily activity, and impact the aircraft and road transportation. It pollutes the atmosphere and air quality, influences cloud formation (James et al., 2007), obscures the sunlight, and reduces the temperature. Some dust storm can suspend on the air for several days and travel by the wind far from the place where it originated. Recently, several researches observed that the heavy dust storm can impact the formation and evolution of hurricane (Dunion and Velden, 2004; Wu et al., 2006).

1.2 Statement of Problems

Due to the importance of smoke and dust aerosols in climate, environment, air

quality, and daily life, detection of smoke and dust aerosols is a very meaningful task. In present, various satellite remote sensors were launched in the sky for diversities of applications. However, not all sensors are suitable for monitoring smoke and dust aerosols. MODIS is an instrument suitable for this task because of its good spectral, spatial, and temporal resolutions: 1) it observes the Earth using 20 Reflective Solar Bands (RSBs) and 16 Thermal Emissive Bands (TEBs) with wavelength range 0.4 ~ 14.2 μm; 2) the spatial resolution is up to 1 km for most bands, which is high enough to monitor smoke from wildfires and dust storm events; 3) four measurements can be obtained for the same location every day except small gaps in the equatorial areas. Additionally, the MODIS Characterization Support Team (MCST) gives both financial and technical supports to study the correlation between measurements/products and MODIS sensor characterization. It is a great chance to evaluate the uncertainties from instrument itself. Consequently, MODIS is picked up as the major sensor for smoke and dust detection in this dissertation.

Currently, several approaches have been developed for smoke and dust detections using MODIS measurements. However, most of them detect smoke/dust aerosols only with measurements of either RSBs or TEBs. And in most of approaches, the cloud mask product (Ackerman et al., 2002) is used directly, which may misclassify smoke and dust as cloud in some conditions, hence leading to low quality detection results. The detail review of each approach is given in the chapter two. Therefore, I developed an approach based on the multi-spectral technique for detecting smoke and dust aerosols combining both MODIS RSB and TEB measurements.

1.3 Objectives and Scopes

The main objectives of this dissertation are seeking to develop an approach for detecting smoke and dust aerosols at given areas (smoke plumes in USA and dust storms in Asia) based on the spectral and statistical analyses. The specific objectives are listed as follows:

1) To develop an approach based on multi-spectral technique for detecting smoke and dust aerosols combining measurements of both MODIS RSBs and TEBs.

2) To detect dust storm using multi-sensor measurements.

3) To assess the potential impact of MODIS spatial characterization change on the L1B measurement and smoke/dust detection results.

1.4 Organization of Dissertation

This dissertation consists of eight chapters. In order to better understand the study, the background and literature review are given in the first two chapters. The next five chapters present various works related to objectives of the dissertation. The summary and discussion of future directions are summarized in last chapter.

Chapter 1 gives the general introduction, including the importance of detecting smoke and dust aerosols, problems of detection approaches, research objectives, major data sources and principle results of the dissertation.

Chapter 2 reviews the approaches of smoke and dust detection used in past and present, as well as advantages and limitations of each approach.

In Chapter 3, the spectral analysis on the basis of hyper-spectral measurements and

basic radiative transfer model is performed. According to spectral curves of various scene types, a multi-spectral algorithm for automated monitoring smoke is developed. The algorithm is applied to smoke plumes occurred from 2007 Georgia Fire and California Fire in United States. The observation of smoke movement and growth by combining two MODIS instruments is also presented in this chapter.

The algorithm for monitoring Asian dust storms with MODIS measurements is discussed in Chapter 4. The whole process of algorithm development is similar to that of smoke detection.

Detecting dust aerosol with MODIS and CALIPSO measurements is given in Chapter 5. CALIPSO provides the vertical information about aerosols and clouds. It has the capability of separating aerosol from ground surface. Furthermore, it is easy to discriminate dust from cloud with MODIS thermal emissive bands. Therefore, with the cooperation of both sensors, the dust aerosol can be detected more accurately.

In Chapter 6, the quantitative validation of smoke and dust detection with OMI and CALIPSO is executed.

The potential impacts on aerosol detection caused by MODIS on-orbit spatial characterization are introduced in Chapter 7. Mis-registration between MODIS bands and Focal Plane Assemblies (FPAs) has been observed, which can produce undesired impact on L1B measurements and aerosol detection. With on-orbit spatial characterization results, the sensitivity analysis is performed to investigate the impact of mis-registration on L1B and aerosol detection.

Chapter 8 summarizes the results from the previous chapters and gives limitations,

originalities, and discussions of future directions.

1.5 Major Data Sources

The major datasets used in this dissertation include MODIS L1A Geolocation and MODIS L1B calibrated radiance, MODIS L2 aerosol product, MODIS L2 fire product, OMI Aerosol Index (AI), CALIPSO Lidar L1B profiles, CALIPSO L2 product, and Hyperion measurement. The usages of these datasets in the study are described in details as follows:

1) MODIS L1A geolocation data

MODIS L1A file records geolocation data (latitude and longitude) at 1 km resolution which is used for projecting the images. The land/sea mask, another important parameter in L1A file, is selected for identifying smoke over land and ocean.

2) MODIS L1B calibrated radiance

The L1B dataset contains calibrated radiances of 36 bands. Usually, the reflectance of RSBs is calculated from digital number with Solar Zenith Angle (SZA) correction, and the Brightness Temperature (BT) of TEBs is converted from radiance. The major MODIS measurements for detection of smoke and dust aerosols in chapter 3 and 4 are the Version 5 L1B dataset.

3) MODIS L2 aerosol product

The MODIS aerosol product retrieves the Aerosol Optical Thickness (AOT) over the oceans and the continents. The resolution of daily product is 10 km (at nadir). Recently, the aerosol product adopts the deep-blue technique to get AOT over bright land areas.

The AOT product is selected for the comparison with detecting results.

4) MODIS thermal anomalies, fires, and biomass burning product

The MODIS thermal anomalies product includes fire occurrence (day/night) and fire location, that are plotted in the smoke images for locating the origination of the plume. The fire product is retrieved daily at 1 km resolution.

5) Hyperion measurement

Hyperion is a hyperspectral instrument with 220 spectral channels. The measurements from different channel are used for spectral analysis of smoke plume.

6) OMI AI

The OMI UVAI is an effective index to reflect the presence of absorbing aerosols. Therefore, UVAI product is adopted for the quantitative validation of smoke and dust detection in Chapter 6.

7) CALIPSO dataset

The CALIPSO Lidar L1B profile (version 2.01) provids the total attenuated backscatter signal at 532 nm and 1064 nm, perpendicular attenuated backscatter signal at 532 nm, aerosol type, geolocation, altitude, elevation of surface, temperature, pressure, calibration parameters, and so on. The VFM (Vertical Feature Mask) (Vaughan et al., 2004), one of CALIPSO level 2 products, provides the scene classification in a 16-bit integer for each altitude resolution element. In Chapter 5, CALIPSO measurement is used for dust detection by jointing with MODIS. The quantitative validation of dust detection is also performed with CALIPSO in Chapter 6.

1.6 Principal Results

The principle results of this dissertation include developing an algorithm based on multi-spectral technique for detecting smoke and dust aerosols combining MODIS RSBs and TEBs; discussing the feasibility of dust detection with multi-sensor measurements; and assessing the impact of sensor calibration and characterization on detection results.

1) The multi-threshold algorithm for automatically detecting smoke and dust aerosols is developed by combining measurements of both MODIS RSBs and TEBs. The spectral curves of various scene types are derived statistically from large amount of training dataset collected at the selected areas within last several years. With the spectral and statistical analyses, the appropriate bands are selected and proper thresholds are decided for eliminating unwanted pixels step by step. The algorithm is applied mainly to detect smoke plumes in USA and dust storms in Asia. The results are validated not only with MODIS true color images but also with products of OMI and CALIPSO, showing that the algorithm works well in the given areas with small errors. Pairs of measurements from both Terra and Aqua MODIS in consecutive days give the basic dynamic information about smoke and dust, which are helpful for estimating the spread direction, and magnitude change of these two types of aerosols.

2) The tentative experiment for detecting dust aerosol with multi-sensor, CALIPSO and MODIS, is performed. Since both sensors are operated in the same orbit with similar local equatorial crossing time, the temporal mis-registration is ignored in this dissertation. With the spatial registration, the dust aerosol is accurately identified by jointing the vertical information of CALIPSO measurements with MODIS thermal emissive

measurements.

3) Finally, the uncertainty from sensor spatial characterization on dust storm detection result is assessed. With the on-orbit spatial characterization, mis-registration has been observed between MODIS bands and FPAs. The mis-registration affects the quality of not only L1B measurements but also dust aerosol detection results. The impacts of mis-registration on L1B measurements are relative small, but large on dust aerosol detection, about 3% in select cases. This assessment is very valuable for sensors without on-orbit spatial characterization capability.

Table 1.1: Datasets and Sources

Dataset	Data Source	Link
MODIS L1A geolocation	LAADS[1]	http://ladsweb.nascom.nasa.gov/
MODIS L1B calibrated radiance	LAADS[1]	http://ladsweb.nascom.nasa.gov/
MODIS L2 Aerosol	EDG[2]	http://edcimswww.cr.usgs.gov/pub/imswelcome/
MODIS fire product	EDG[2]	http://edcimswww.cr.usgs.gov/pub/imswelcome/
Hyperion data	USGS[3]	http://eo1.usgs.gov/samplefire.php
OMI AI	GES DAAC[4]	http://daac.gsfc.nasa.gov/Aura/OMI/index.shtml
CALIPSO dataset	ASDC[5]	http://eosweb.larc.nasa.gov/JORDER/ceres.html

1 LAADS: Level 1 and Atmosphere Archive and Distribution System
2 EDG: Earth Observing System Data Gateway
3 USGS: U.S. Geological Survey
4 GES DAAC: Goddard Earth Science Distributed Active Archive Center
5 ASDC: Atmospheric Science Data Center

CHAPTER 2

REVIEW OF APPROACHES FOR DETECTING SMOKE AND DUST

AEROSOLS

In the past, several approaches for detecting smoke and dust aerosols using satellite remote sensing measurements have been developed, tested, and validated based on the different techniques. This chapter focuses on the review of different approaches so as to find their physical principles, and their advantages and limitations, which are beneficial for the development of a new robust algorithm.

2.1 Approaches of Smoke Aerosol Detection

Smoke plume from biomass burning can generate forcing of climate by changing cloud microphysics and reflectance of sunlight (Kaufman and Fraser, 1997). The smoke particle is a good scatter of sunlight in visible spectrum and therefore reduces the visual visibility. There are two kinds of climatic impacts by smoke: one is warming effect on the atmosphere because smoke acts like greenhouse gases, and the other is cooling effect because smoke particulate is an excellent absorber and scatter of incoming solar radiation (Li, 1998).

Satellite remote sensing has been demonstrated as a feasible tool for the

identification of smoke plume (Chung and Le, 1984). Among various techniques, visible imagery approach is a fast and easy way to visually identify smoke, by assigning three bands (or band combination) as the red, green, and blue channel respectively to generate either true color or false color images (Chung and Le, 1984; Kaufman et al., 1990; Randriambelo et al., 1998; Chrysoulakis and Opie, 2004, Chrysoulakis and Cartalis, 2003). For example, MODIS RGB true color images are generated with bands 1, 4 and 3 jointly. On the other hand, the combination of several bands may act as one band to generate images. Christopher and Chou (1997) used the normalized ratio of Advanced Very High Resolution Radiometer (AVHRR) band 1 and 4 to represent the green channel to produce an image. Then this image was used to compute several textural measures for a 9×9- pixel window (Welch et al., 1988; Trovinkere et al., 1993; Christopher et al., 1996), to visually separate the smoke aerosols from the other scene types. However, these color-based approaches can provide only basic information about smoke and fail to provide automatic identification.

Multi-threshold approach is one of effective tools to detect smoke based on the physical property difference between smoke and other scene types, such as cloud, vegetation, water, snow, ice, and soil. Generally, the algorithm employs a set of threshold tests to check all image pixels simultaneously to separate smoke from other scene types step by step. In each test, the particular thresholds, either static or dynamic, are calculated generally by the statistical analysis of training data. Baum and Trepte (1999) proposed a grouped threshold method for scene identification with AVHRR measurements. In their method, the smoke was classified by smoke module consisted with several thresholds test

11

cooperatively: the reflectance at 0.63 μm and 3.7 μm channel, the Bright Temperature (BT) difference between 3.7 μm and 11 μm channel, and the BT difference between anticipated clear-sky value and measured value at 11 μm channel. Li et al. (2001) presented a multi-threshold method for automated smoke plume detection using AVHRR measurements based on the neural networks. The shortcoming of using AVHRR is that AVHRR has only five channels, which is inefficient for smoke detection.

Chrysoulakis et al. (2007) proposed a multi-temporal change detection approach using two images at the same target area on the different time. By comparing two images (one is acquired during the fire event and the other is acquired before fire event), the important anomalies in NDVI and infrared radiances were detected hence to detect the core of plume. Then the plume core was enlarged to include the complete smoke area through identifying a pixel as plume pixel if it located spatially and spectrally at the neighborhood of the initial plume core. The new developed one offers a novel ways for smoke monitoring. However, this approach need find a clear day before the occurrence of smoke. The Bidirectional Reflectance Distribution Function (BRDF) issue is also need to be taken into account.

The current MODIS aerosol retrieval algorithm uses the dark target approach (Kaufman et al. 1997, Kaufman et al. 1997) with two assumptions: 1) the aerosol is transparent to most aerosol types (except dust) at 2.1 μm so that this channel can be used to detect dark surface targets; 2) the surface reflectance at 0.47 μm and 0.64 μm channel could be retrieved by that at 2.1 μm with the ratio 0.25 and 0.5. With the assumptions, the Aerosol Optical Thickness (AOT) and particle size parameters were retrieved at 0.47 μm

and 0.66 μm wavelengths and then interpolated to derive AOT at 0.55 μm. Therefore, smoke aerosols can be identified based on their size differences and absorption if smoke optical thickness is up to 3 (Kaufman et al. 2003). Although the assumptions are valid for most vegetated land surfaces (Chu et al. 2003), land surface reflectance may significantly deviates from this assumption over some bright surface regions. Hsu et al. (2004) proposed a Deep Blue algorithm suitable for aerosol identification over brightly reflecting surfaces because the surface reflectance at the deep blue channel is low enough to make such retrievals possible. In the algorithm, a maximum likelihood method is used to find the best match between the measured reflectance and the one stored in look-up-table at three blue channels to determine aerosol mode and the mixing ratio, hence to calculate aerosol optical thickness and Ångström exponent. However, several key parameters are based on surface albedo database and model simulation, further investigations and improvements are still needed.

2.2 Approaches for Dust Aerosol Monitoring

Similar to smoke detection, color imagery technique is the primary tool for dust storm monitoring in the past. Earlier researchers used visible spectrum to monitor dust outbreaks as well as to estimate dust optical depth over oceanic regions (Carlson, 1978; Norton et al., 1980). Dust was detected and its evolution followed by its yellow color on SeaWiFS satellite images. Some researchers also apply color enhancement techniques (Miller, 2003) to differentiate dust, ocean surface, and cloud.

Spectral indices based on dust characteristics over VIS/NIR/IR regions may provide

more information about dust characteristics. Qu et al. (2006) used Normalized Difference Dust Index (NDDI), a normalized ratio of 2.1μm band and blue band, to detect dust storms and monitor the moisture change of dust. NDDI has advantages because of the high sensitivity of MODIS 2.1μm band to moisture content. Recently, several studies show that it is feasible to detect Saharan dust over land using BT in thermal infrared spectra (Cavtenet et al., 1992; Legrand et al., 1987; Legrand et al., 1989; Legrand et al., 1992; Legrand et al.,2001) Hao et al, (2007) proposed a thermal infrared index to detect Saharan dust storms by combining fours MODIS TEBs. A correlation of the BT between 11 μm and 3.7 μm bands for dust outbreaks was proposed by Ackerman (1989). He developed a tri-spectral (8, 11 and 12 μm) technique later for detecting dust over water and for distinguishing dust plumes from water/ice clouds (Ackerman, 1997). An automatic multi-spectral approach for detection of dust storm in the northwest of China is developed by Han et al. (2005). In his approach, a set of indices were used to separate dust from cloud, snow, and land with several RSB measurements. However, most of approaches for dust (also for smoke) detection chooses either RSB measurements or TEB measurements.

For retrieval of dust parameters such as aerosol optical thickness, current algorithm works only over dark surface. The reason is that the algorithm is based on the empirical relationship between MODIS VIS bands and Small Wavelength Infrared (SWIR) bands (Kaufman 1997).

14

2.3 Chapter Summary

This chapter reviewed the approaches for detecting smoke and dust aerosols in past and present. Although visual identification of aerosol can provide quick identification, this technique only gives very limit information about smoke and dust aerosols. And this approach cannot offer automated detection of smoke and dust aerosols, which is not suitable for processing large amount of remote sensing measurements timely. Although current MODIS operational product provides aerosol classification based on dark target approach and deep blue approach, it misclassified most smoke/dust events near or mixed with cloud since it adopted cloud mask product directly which has strict standard to filter out all suspicious pixels. Moreover, the 10 km^2 spatial resolution is also relatively coarse. The physical principle of multi-spectral method is to find the spectral feature difference between several major kinds of scene types in VIS/NIR/IR even in microwave spectra. As discussed above, most multi-spectral approaches use the combination of the bands either in the solar spectrum or thermal spectrum. Similarly, most approaches can detect smoke or dust only at those areas away from cloud.

Based on the review of the physical bases, advantages, and limitations of above approaches, the multi-spectral approach is selected for smoke and dust aerosol detection in this dissertation by combining measurements of both MODIS RSBs and TEBs. The major goal of this algorithm is to detect smoke and dust aerosols over both dark and bright surfaces. Moreover, the algorithm is aim to avoid the misclassification over the areas close to or mixed with cloud.

CHAPTER 3

SMOKE AEROSOL DETECTION WITH MODIS MEASUREMENTS

Smoke aerosol from wildfires is a mixture of gases, organic compounds and particles, including carbon dioxide (CO2), carbon monoxide (CO), nitrogen oxides (NOx), sulfur dioxide (SO2), and so on (Austin and Goyer, 2007). The mixing level of these components varies with the types of burning wood and vegetation so that smoke aerosol has no stable spectral characteristic. Therefore, a multi-spectral method combining both MODIS RSBs and TEBs is developed in this chapter (Xie et al., 2007). The smoke is identified by filtering out other scene types step by step, according to their reflectance differences in solar spectrum and their BTD in thermal spectrum. The bands are selected and thresholds are decided on the basis of spectral and statistical analyses, as well as basic radiative transfer model. The algorithm works well on detection of smoke plumes occurred in the United States. The validation of results with MODIS true color images is also presented in this chapter.

3.1 MODIS Instrument

MODIS, one of key sensors of the National Aeronautics and Space Administration (NASA) Earth Observing System (EOS), was launched onboard the Terra spacecraft on December 18, 1999 and the Aqua spacecraft on May 4, 2002 (Barnes et al., 2002; Salomonson et al., 2002). Both Terra and Aqua MODIS are operated in a sun-synchronous orbit at the altitude of 705 km. Terra descends southwards with the local equatorial crossing time 10:30 a.m. and Aqua ascends northwards with the local equatorial crossing time 1:30 p.m. respectively. The MODIS has been widely used for the study of land, ocean, atmosphere, and solid earth etc. (Justice et al., 1998; Esaias et al., 1998; King et al., 2003; Parkinson, 2003).

3.1.1 MODIS spectral band

The MODIS makes the Earth observations with 36 bands, covering the wavelength range from 0.4 to 14.2 μm. The 20 RSBs and 16 TEBs are arranged in four FPAs: VIS, NIR, Short- and Middle- Wavelength Infrared (SMIR), and Long- Wavelength Infrared (LWIR), shown in Fig. 3.1 (Che et al., 2005). Three different spatial resolutions are designed according to the band specifications and science applications: 250 m (band 1-2), 500 m (band 3-7), and 1 km (band 8-36). The number of detectors of each band is 40, 20, and 10 respectively corresponding to its spatial resolution (Barnes et al., 2002; Salomonson et al., 2002). The specifications of all spectral bands are listed in Table 3.1. Among these bands, band 1 (red), band 4 (green), and band 3 (blue) are usually used for constructing RGB true color image. The MODIS is a cross-track scanning radiometer

with a two-side scan mirror which rotates over a scan angle range of ±55°, producing a

swath of 2330 km in scan direction and 10 km in track direction each scan (Xiong et al.,

2007).
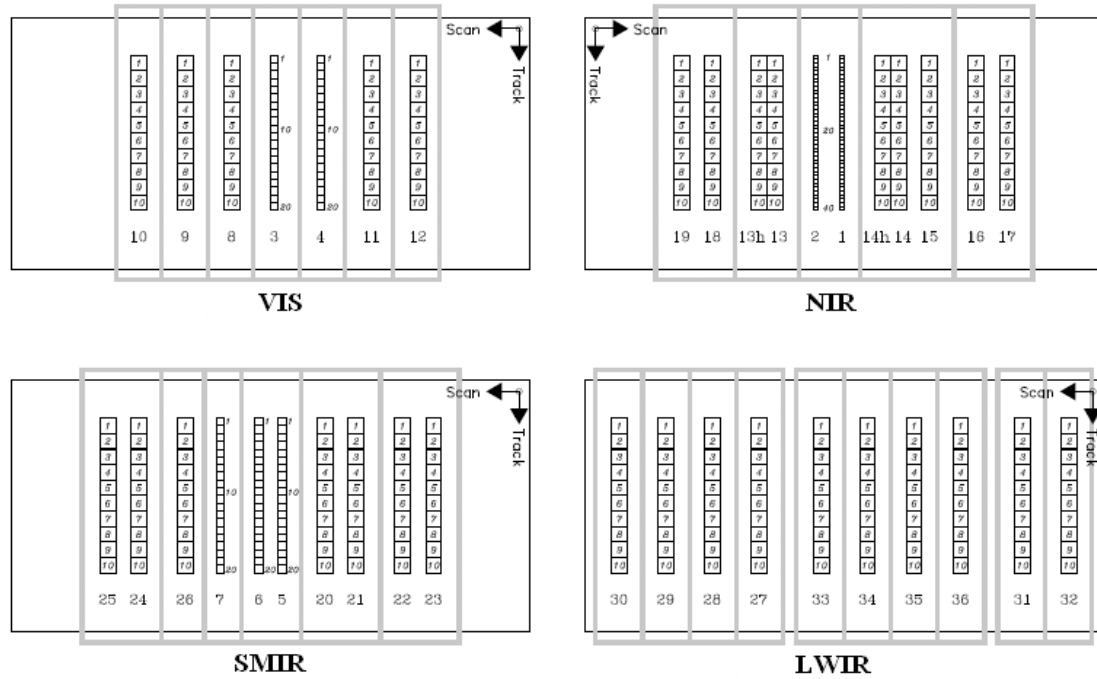
Figure 3.1: The layout of the MODIS FPAs. All 36 MODIS bands are separated into four FPAs: VIS, NIR, SMIR, and LWIR. The number of detectors of each band varies with the spatial resolution: 40 detectors for 250 m bands, 20 detectors for 500 m bands, and 10 detectors for 1 km bands (Source: Che et al., 2005).

Table 3.1: Specifications of MODIS spectral bands.

FPA	Band	CW	Bandwidth[1]	Ltyp[2]	Primary Use
R S B	1	645 nm	620-670	21.8	Land/Cloud/Aerosols Boundaries
	2	858 nm	841-876	24.7	Land/Cloud/Aerosols Boundaries
	3	469 nm	459-479	35.3	Land/Cloud/Aerosols Properties
	4	555 nm	545-565	29.0	Land/Cloud/Aerosols Properties
	5	1240 nm	1230-1250	5.4	Land/Cloud/Aerosols Properties
	6	1640 nm	1628-1652	7.3	Land/Cloud/Aerosols Properties
	7	2130 nm	2105-2155	1.0	Land/Cloud/Aerosols Properties
	8	412 nm	405-420	44.9	Ocean Color/ Phytoplankton/Biogeochemistry
	9	443 nm	438-448	41.9	Ocean Color/ Phytoplankton/Biogeochemistry
	10	488 nm	483-493	32.1	Ocean Color/ Phytoplankton/Biogeochemistry
	11	531 nm	526-536	27.9	Ocean Color/ Phytoplankton/Biogeochemistry
	12	551 nm	546-556	21.0	Ocean Color/ Phytoplankton/Biogeochemistry
	13	667 nm	662-672	9.5	Ocean Color/ Phytoplankton/Biogeochemistry
	14	678 nm	673-683	8.7	Ocean Color/ Phytoplankton/Biogeochemistry
	15	748 nm	743-753	10.2	Ocean Color/ Phytoplankton/Biogeochemistry
	16	869 nm	862-877	6.2	Ocean Color/ Phytoplankton/Biogeochemistry
	17	905 nm	890-920	10.0	Atmospheric Water Vapor
	18	936 nm	931-941	3.6	Atmospheric Water Vapor
	19	940 nm	915-965	15.0	Atmospheric Water Vapor
	26	1375 nm	1360-1390	6.0	Cirrus Clouds Water Vapor
T E B	20	3.75 μm	3.660-3.840	300	Surface/Cloud Temperature
	21	3.96 μm	3.929-3.989	335	Surface/Cloud Temperature
	22	3.96 μm	3.929-3.989	300	Surface/Cloud Temperature
	23	4.05 μm	4.020-4.080	300	Surface/Cloud Temperature
	24	4.47 μm	4.433-4.498	250	Atmospheric Temperature
	25	4.52 μm	4.482-4.549	275	Atmospheric Temperature
	27	6.72 μm	6.535-6.895	240	Water Vapor
	28	7.33 μm	7.175-7.475	250	Water Vapor
	29	8.55 μm	8.400-8.700	300	Water Vapor
	30	9.73 μm	9.580-9.880	250	Ozone
	31	11.03 μm	10.78-11.28	300	Surface/Cloud Temperature
	32	12.02 μm	11.77-12.27	300	Surface/Cloud Temperature
	33	13.34 μm	13.18-13.48	260	Cloud Top Altitude
	34	13.64 μm	13.48-13.78	250	Cloud Top Altitude
	35	13.94 μm	13.78-14.08	240	Cloud Top Altitude
	36	14.24 μm	14.08-14.38	220	Cloud Top Altitude

[1] The unit of bandwidth in this table for RSB is nm and for TEB is μm

[2] Ltyp is the typical value for RSB in the unit of $W/m^2/sr/\mu$ and for TEB in the unit of K

Source: http://modis.gsfc.nasa.gov/about/specifications.php

3.1.2 MODIS data

The 55^0 scan angle of MODIS enables it to achieve almost daily global coverage except for some small gaps in equatorial areas. Each MODIS sensor passes the same site twice a day: one in the daytime orbit for all thirty-six bands and the other in the nighttime orbit only for the TEBs (bands 20-25 and 27-36). Totally, four measurements can be collected every day with two MODIS sensors. The data used in this dissertation is the version 5 L1B measurements issued by NASA. Each MODIS file (referred to as a "granule") collects consecutive measurements within five minutes, typically 203 scans, covering an area with 2030 km (along-track) by 2330 km (cross-track) (Nishihama et al., 2000; Isaacman et al., 2003). In each scan, 1,354 data frames are recorded for each detector. For 500 m resolution band, 2 sub-frames or samples per frame (1 km) are recorded for its 20 detectors, and 4 sub-frames for each 250 m band and its 40 detectors (Xiong et al., 2003). Thus, each granule typically contains 2030 rows (along-track) $\times$ 1354 columns (along-scan) for 1 km resolution bands, 8120 rows $\times$ 5416 columns for 250 m resolution bands, and 4060 rows $\times$ 2708 columns for 500 m resolution bands. The geolocation data (latitude and longitude) in L1A are used to find the selected site automatically. The land/sea mask dataset assists users to quickly separate land from ocean (water). In L1B, the stored data format is digital number, which is generally converted into the reflectance or the radiance for RSBs and the radiance for TEBs with carefully calibrated scale and offset. Moreover, 250 m (band 1-2) and 500 m (band 3-7) resolution measurements can be aggregated to match 1 km resolution band for further spectral arithmetic (Nishihama et al., 1997).

3.2 Physical Principle of Smoke Aerosol Detection

The primary physical principle of multi-spectral algorithm for smoke/dust detection is to find the spectral difference between smoke/dust and other scene types. Generally, each scene type has its unique spectral characteristics. In some spectra (or bands), its spectral characteristics is significantly different from that of other scene types. Those bands, usually sensitive or insensitive to certain scene types, are picked up for the classification. The precision of classification depends mainly on the proper band selection and threshold definition of each test. The spectral analysis based on radiative transfer model and large amount of training data is performed in the following chapter.

3.2.1 Radiative transfer model

In solar spectrum, the signal received by MODIS sensor is reflected by the surface in a clear sky. It becomes relatively complicate, however, if there is an aerosol layer floated between sensor and ground surface, due to multiple scattering. In the radiative transfer model shown in Fig 3.2, part of sunlight is reflected by smoke (or dust) layer and then reaches to the sensor. Other lights are reflected by the surface after penetrating through smoke layer and then received by the MODIS sensor.
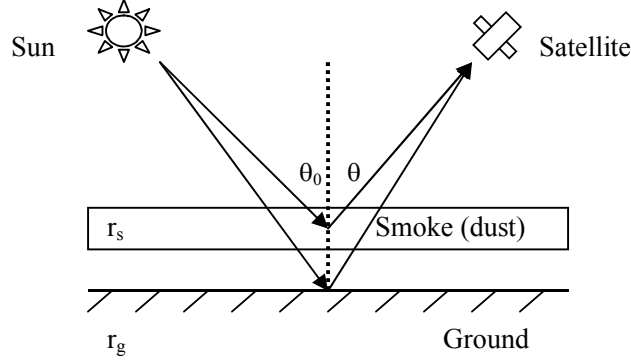
Figure 3.2: Basic radiative transfer model

Based on the fundamental radiative transfer model (Liou, 2002; Li et al., 2001), the reflectance at TOA viewed from a satellite can be expressed as in Eq. 3.1.

$$r(\lambda; \mu_0, \phi_0; \mu, \phi) = t(\lambda; \mu_0) r_s(\lambda; \mu_0, \phi_0; \mu, \phi) t(\lambda; \mu)$$

$$+ t(\lambda; \mu_0) \exp\left(\frac{-\tau}{\mu_0}\right) \frac{r_g(\lambda; \mu_0, \phi_0)}{1 - \overline{r}_s^*(\lambda)\overline{r}_g(\lambda)} \cdot \left[\exp\left(\frac{-\tau}{\mu}\right) + t_s^*(\lambda; \mu, \phi)\right] t(\lambda; \mu)$$

$$+ t(\lambda; \mu_0) t_s(\lambda; \mu_0, \phi_0) \frac{\overline{r}_g(\lambda)}{1 - \overline{r}_s^*(\lambda)\overline{r}_g(\lambda)} \cdot \left[\exp\left(\frac{-\tau}{\mu}\right) + t_s^*(\lambda; \mu, \phi)\right] t(\lambda; \mu)$$

(3.1)

where λ is the wavelength and τ is optical depth of smoke layer. Two parameters, μ_o and μ are the cosine of the solar zenith angle and view angle. $t\,(\lambda,\,\mu_o)$ is the transmittance from the top of atmosphere to smoke and $t\,(\lambda,\,\mu)$ is the transmittance in inverse direction in the view direction of satellite. Two azimuth angles, ϕ_o and ϕ, are viewed from sun and satellite, respectively. In Eq. 3.1, the notation asterisks indicate that these quantities are

for upwelling radiation. The plane albedo of ground surface r (λ, μ_o, ϕ_o) is given by the corresponding bidirectional reflectance r $(\lambda; \mu_o, \phi_o; \mu, \phi)$ via the following relationship in Eq. 3.2, and the spherical albedo of the ground surface is given by Eq. 3.3.

$$r_g(\lambda; \mu_0, \phi_0) = \frac{1}{\pi} \int_0^{2\pi} \int_0^1 r_g(\lambda; \mu_0, \phi_0; \mu, \phi) \mu d\mu d\phi$$

(3.2)

$$\overline{r}_g(\lambda) = \frac{1}{\pi} \int_0^{2\pi} \int_0^1 r_g(\lambda; \mu_0, \phi_0) \mu_0 d\mu_0 d\phi_0$$

(3.3)

Similarly, r_s $(\lambda; \mu_o, \phi_o; \mu, \phi)$ is the bidirectional reflectance of smoke layer for the incidence radiation. $\overline{r}_s^*(\lambda)$ is the spherical albedo of the smoke for upwelling radiation. In Eq. (3.1), t $(\lambda; \mu_o, \phi_o)$ and t^* $(\lambda; \mu, \phi)$ are diffused transmittances of the smoke for downward and upwelling radiation, respectively.

Set the spectral bandwidth as $\Delta\lambda$ for a given band with the Center Wavelength (CW) at λ_o and let the instrument Relative Spectral Response (RSR) function be $RSR(\lambda)$. Integrate the product of each quantity in Eq. 3.1 and RSR with respect to λ. The average reflectance is given by Eq. 3.4a

$$r_{\lambda_0}(\mu_0, \phi_0; \mu, \phi) = T_{\lambda_0}(\mu; \mu_0) r_{s,\lambda_0}(\mu_0, \phi_0; \mu, \phi)$$
$$+ b_{\lambda_0}(\mu_0, \phi_0; \mu, \phi) r_{g,\lambda_0}(\mu_0, \phi_0; \mu, \phi)$$

(3.4a)

where

$$T_{\lambda_0}(\mu; \mu_0) = \frac{1}{\Delta\lambda} \int_{\lambda_0 - \lambda/2}^{\lambda_0 + \lambda/2} t(\lambda, \mu_0) t(\lambda, \mu) RSR(\lambda) d\lambda$$

(3.4b)

23

$$b_{\lambda_0}(\mu_0,\phi_0;\mu,\phi)=\frac{1}{\Delta\lambda}\int_{\lambda_0-\lambda/2}^{\lambda_0+\lambda/2}\left\{k_1\left[\exp\left(\frac{-\tau}{\mu_0}\right)+t_s(\lambda;\mu_0,\phi_0)\right]\right.$$

$$+k_2\left[\exp\left(\frac{-\tau}{\mu}\right)+t_s^*(\lambda;\mu,\phi)\right]\right\}$$

$$\cdot\frac{t(\lambda;\mu_0)\cdot t(\lambda;\mu)}{1-\bar{r}_s^*(\lambda)\bar{r}_g(\lambda)}RSR(\lambda)d\lambda$$

(3.4c)

(3.4d)

(3.4e)

In Eq. 3.4a, it is reasonable to say that the signal received by the sensor come from two parts: one is reflected by the aerosol layer directly and the other is contributed from the ground surface.

3.2.2 Smoke spectral feature

The continuous measurements of Hyperion, a hyperspectral sensor, are collected for analyzing the spectral characteristics of the smoke. The Fig. 3.3 show the smoke plume originated from the Aspen fire in Arizona on July 7, 2003. The first subplot is the true color image and rest of eight subplots are derived from measurements of eight typical bands with CW 447, 549, 600, 651, 752, 854, 1044, and 1245 nm. Those eight bands are chosen because they have the similar CW to those corresponding bands in MODIS. In the figure, the smoke plume has the strong reflectivity in the short wavelength bands but

become more transparent in the long wavelength bands. This phenomenon illustrates that the short wavelength bands are more sensitive to smoke than the long wavelength bands.

According to the radiative transfer model, the signal received by sensor is comprised of two parts (Eq. 3.4a). In the short wavelength range, the smoke obscures the surface so that the signal is contributed largely from the smoke layer. The contribution to signal from the ground surface increases in the long wavelength range because of the transparency of smoke layer. Therefore, the short wavelength bands such as blue band are very critical for the detection of smoke plume. Consequently, in solar spectrum choosing at least a short wavelength band in each test is the prerequisite to increase the quality of algorithm. It is worth noting that some bands located in the spectral window of water vapor or ozone can be used solely, such as band 26, a water band for measuring high cirrus cloud Gao et al., 1993; Gao et al., 2002).

| 447 nm | 549 nm | 600 nm | 651nm | 752 nm | 854 nm | 1044 nm | 1245 nm |
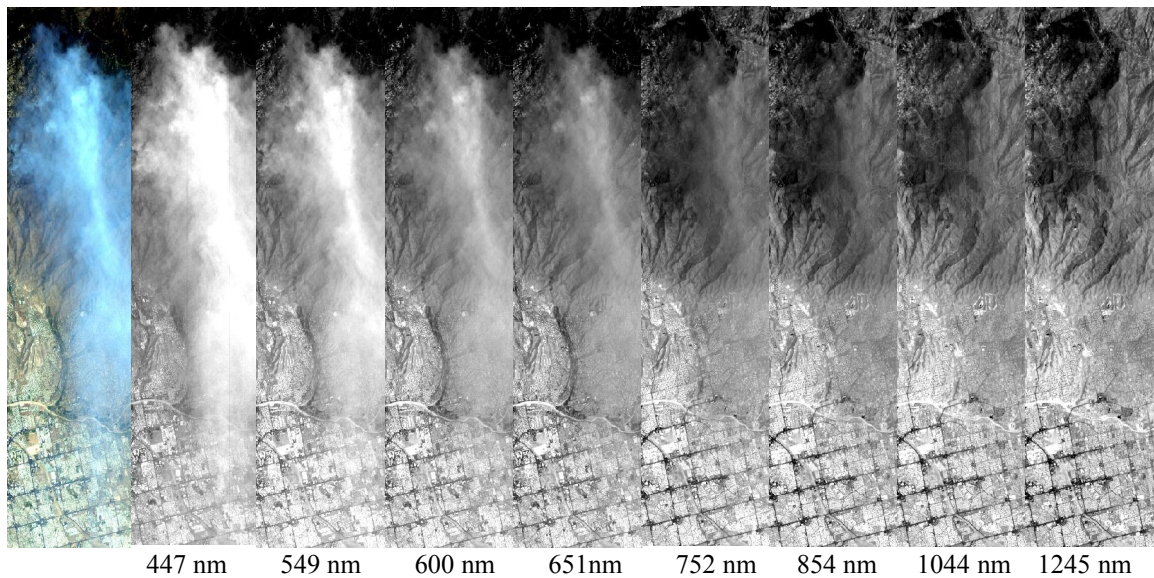
Figure 3.3: Images with smoke plume generated from eight Hyperion bands to show the transparency feature from short wavelength to long wavelength.

3.2.3 Training data collection

Surface geology and wood species, two key parameters affecting the spectral response of smoke received by sensor, vary with site by site. The geology decides the reflectivity of the surface and the wood species determines the component of smoke plume. The amount of training data in given area determines the applicability of the algorithm. In this manner, eighteen smoke plumes with various intensities occurred in USA during last five years (2000-2005) are selected as training data to perform the statistical analysis. Around 200,000 smoke pixels are collected with visual identification, and separated into two classes using MODIS land/sea mask product: smoke pixels over land and ocean respectively. Moreover, bright land pixels, dark land pixels, and cloud pixels are also colleted for deciding the bands and thresholds of each index.

3.2.4 Spectral curves

The spectral responses of several major scene types are calculated statistically from training data, given in Figs. 3.4 and 3.5. The spectral responses at ten bands are plotted in these two figures since those bands are usually used for aerosol detection. The spectral response at each band is the mean value of all training data for each scene type with the standard deviation. Since part of smoke events occurred in eastern or western USA may spread over the oceans, the spectral curves of smoke are separated into two classes: smoke over land and smoke over ocean. For easily comparison, spectral curves of smoke (both over land and ocean) and cloud are plotted in Fig. 3.4. The curves of smoke (over land only) and land (both dark and bright surfaces) are plotted in Fig. 3.5. The abscissa of

both figures stands for the MODIS band number. The vertical axes is the responses of different scene types in each band; the reflectance for RSBs in the left side and the BT for TEBs in the right side.

3.2.5 Band selection

Generally, the Normalized Difference Vegetation Index (NDDI) (Rouse et al., 1973; Huete et al., 1994) is an ideal index for vegetation classification. However, the conclusion in chapter 3.2.2 illustrates that the short wavelength band is sensitive to smoke and at least one short wavelength band is selected in each test. Consequently, a pseudo-NDVI, the normalized ratio of band 2 and band 3 (469 nm), is introduced to discriminate vegetation and smoke pixels. The reason is that smoke has high reflectivity in band 3 than that in band 1 due to Rayleigh scattering while the vegetation appears dark either in band 3.

The NDDI, the normalized ratio of band 7 (2130 nm) and band 3, is an index developed for dust detection (Qu et al., 2006). It is also suitable for soil classification (namely brightly reflecting surface). Normally, the NDDI value is positive for soil or dust but negative for smoke. The inverse value of NDDI is applied for the differentiation smoke from soil surface according to the spectral signature difference.
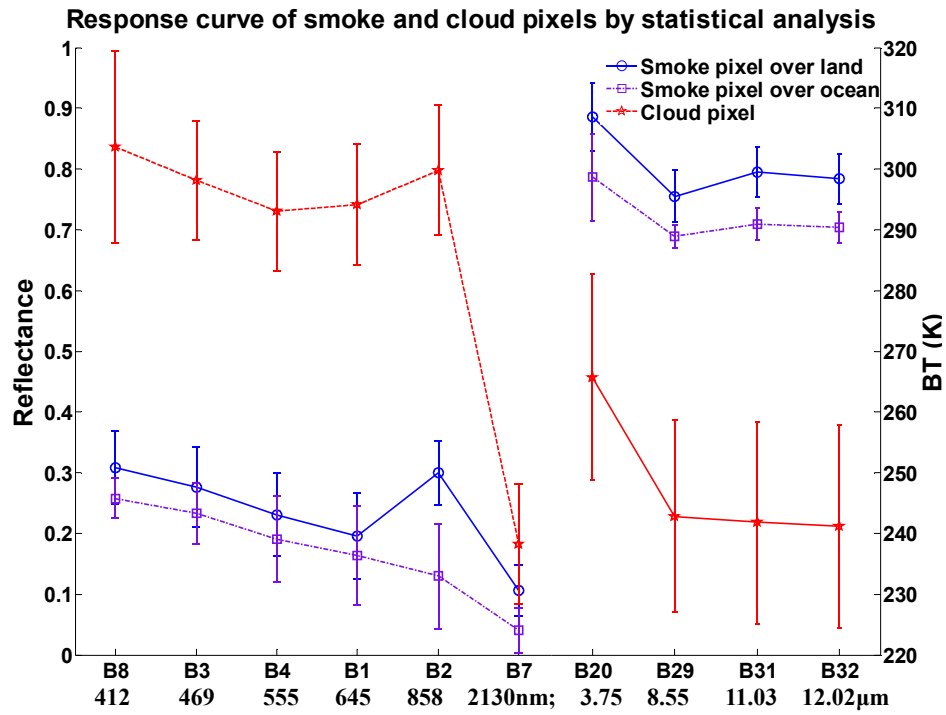
Figure 3.4: Response curves of smoke and cloud pixels.
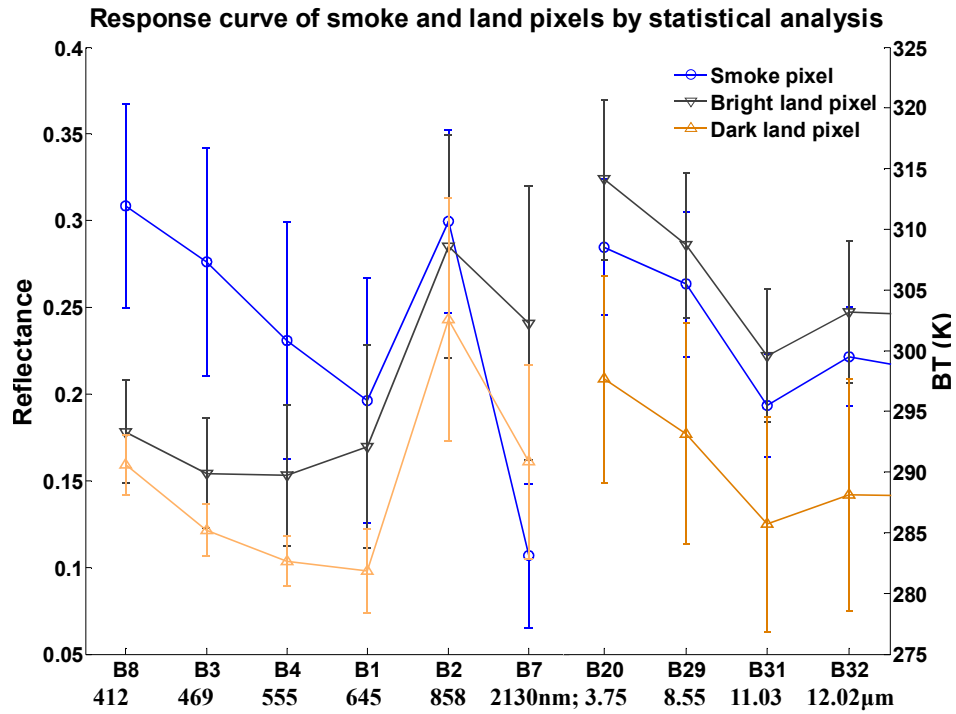
Figure 3.5: Response curves of smoke and land pixels.

28

The BT of the 11 μm band (band 31) and the BTD between the 11 μm band and the 3.7 μm band (band 20) (Ackerman et al., 2002) are used to separate smoke aerosol from cloud, as well as the reflectance at the 1.38 μm channel, a spectrum window of water vapor useful for detecting high cirrus cloud (Gao et al., 1993; Gao et al., 2002).

The normalized ratio of two blue bands, (R3 - R8) / (R3 + R8), and the single reflectance of band 8 (412 nm) are proposed to filter out the noise pixel (mainly water pixels and coastline pixels). Band 8, the shortest wavelength band within MODIS, is strongly sensitive to the smoke aerosol because of Rayleigh scattering. The average geometrical radii of smoke particle are in the range of 0.01 - 0.05 μm, largely satisfying the Rayleigh scattering limit (Wong and Li, 2002; Remer et al., 2002). Rayleigh scattering is wavelength dependence. Its intensity is inversely proportional to the fourth power of the wavelength. As a result, this ratio of two blue bands is very sensitive to aerosol. Two examples with smoke plumes are shown in Fig. 3.6. The normalized ratio of two blue bands for smoke plumes in both images is relative higher than vegetated and water areas, and the ratio values increases with the plume intensity.

For the convenient expression in this dissertation, the single reflectance of certain band is expressed with R (reflectance) plus band number. The BT of certain band is denoted with BT plus CW. The normalized ratio of two bands has the formula like Ratio (Ra, Rb) = (Ra - Rb) / (Ra + Rb), where a and b are band number. The BTD between two bands is given in BTD (CWa, CWb) = BTCWa – BTCWb, where CWa and CWb are CW of band a and band b.
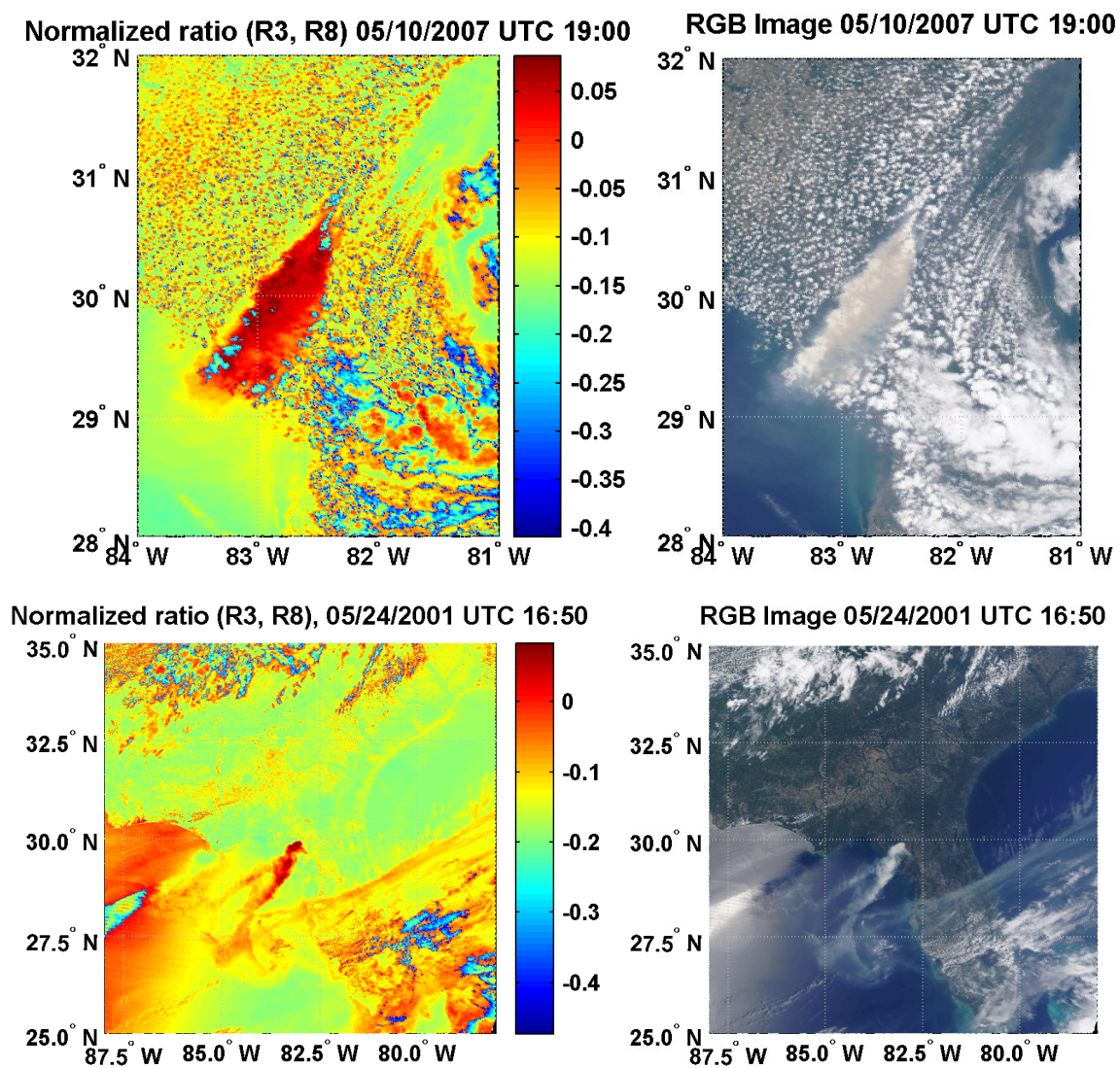
Figure 3.6: The normalized ratio of band 3 and band 8 used for identifying smoke plume and corresponding RGB images. The upper row is the case on May 10, 2007, and the bottom row is the case on May 24, 2001.

3.3 Methodology

3.3.1 Threshold and accuracy analysis

To decide threshold of each test, the scatter plots of several major scene types is given in Figs. 3.7(a-h). Each data point is the average value of all smoke pixels in one smoke events, along with standard deviation.

In each subplot, a pair of scene types is displayed for clear comparison. Figs. 3.7(a) and 3.7(b) give the pseudo-NDVI values and single reflectance of band 8 for smoke and dark pixels. Vegetation pixel has high pseudo-NDVI value but low reflectance in deep blue spectrum. The comparisons between smoke and cloud over land and ocean are plotted in Figs. 3.7(c) - 3.7(f). The cloud usually has a very low BT in the LWIR. Since the long wavelength is insensitive to smoke, the temperature changes very lightly at the smoke area. Therefore, the BT11 and BTD (3.7, 12) have large difference between cloud and smoke. In Fig. 3.7(g), NDDI values of smoke are mostly larger than 0.1 while that of bright pixels are less than 0.1. The Ratio (B3, B8) in Fig. 3.7(f) is effective to separate smoke from dark land, as well as water which has very low reflectance.

The threshold of each index is decided with the statistical calculation to ensure the minimum error of each test. The error is a statistical parameter to reflect how many smoke pixels are not identified with corresponding defined threshold. The threshold which produces minimum error is picked up by adjusting the threshold itself.

The detail thresholds of each index are summarized in Table 3.2. The NDDI and pseudo-NDVI applied only to pixels in the land branch. The rest of indices are applied to

all pixels over both land and ocean. The threshold values of BTD (3.7, 12) are 15 K over land and 9 K over ocean. The total errors for land and ocean branches are estimated. It is worth noting that the total error is not equal to the summation of errors from each test because the overlap exists among some index tests. The accuracy of algorithm over land is much higher than that over ocean. The large errors over ocean are mainly attributed to the undetected thin smoke pixels. In fact, it is very difficult to detect those smoke pixels whose magnitude is relatively low. The smoke plume usually originates from fires in land areas and the plume magnitude becomes weaker and weaker during the motion from land to ocean. Therefore, the probable reason is that there are much more thin smoke pixels over ocean than over land to reduce the algorithm precision.
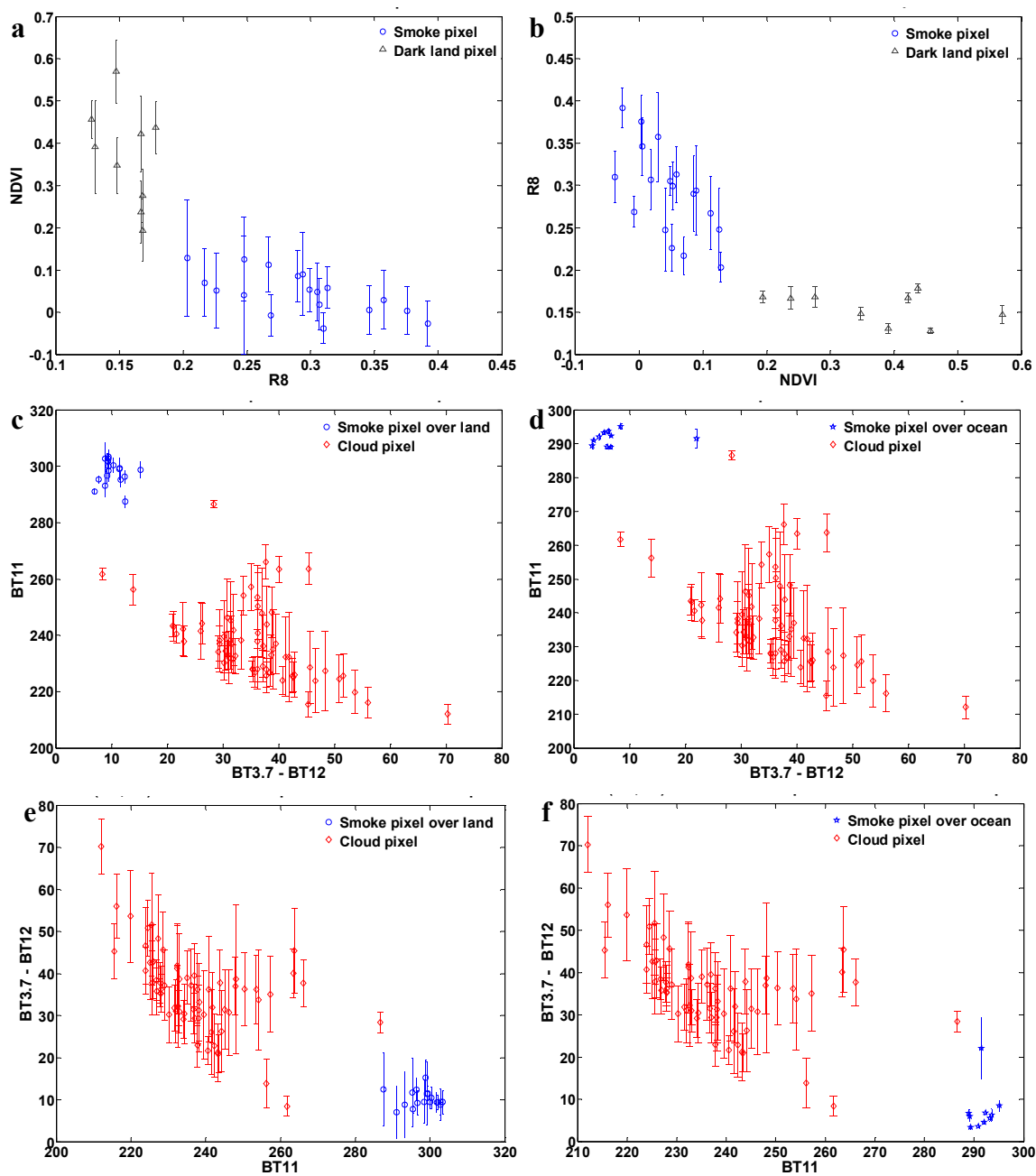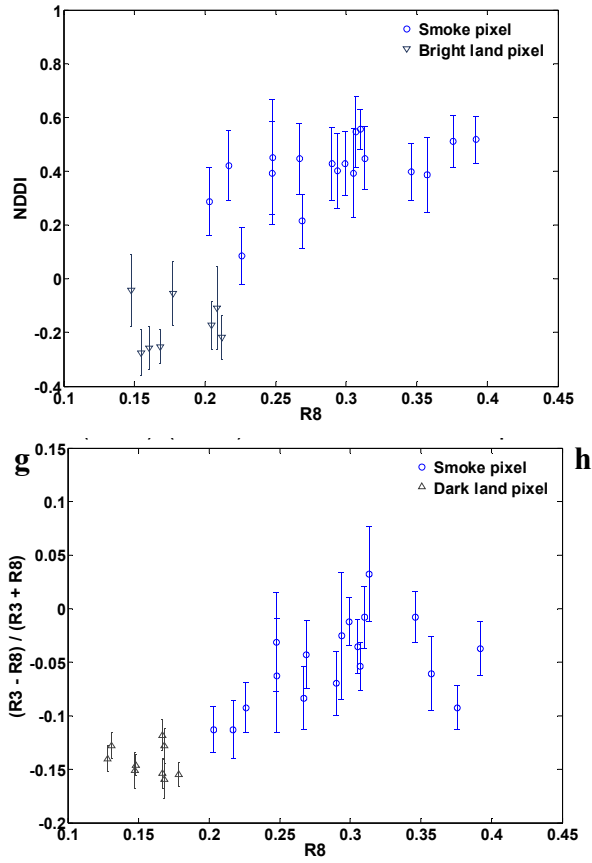
Figure 3.7: Statistical analyses of training data for deciding the threshold.

Table 3.2: The threshold tests and thresholds used for classification of four surface types and sensitivity analysis based on the selected cases in Georgia area during last five years.

Class type	Threshold test	Value	Error (Land)	Error (Ocean)
Vegetation	(B2-B3) / (B2+B3)	0.30	0.045%	N.A.[3]
Soil	(B3-B7) / (B3+B7)	0.10	3.047%	N.A.[3]
	B26 &	0.03	0.007%	0.084%
Cloud	BTD (3.7, 12) &	15(9)K[1]	1.745%	17.937%
	BT11	285K	0.212%	0.683%
Water &	(B3-B8) / (B8+B3)	0.15	0.007%	18.665%
Noise	& B8	0.17	0.000%	1.453%

Total	4.656%^{2}	34.577%^{2}

[1] The threshold of BTD (3.7, 12) is 15 K for pixels over land and 9 K for pixels over ocean.
[2] The total errors of both over land and over ocean are not equal to the summation of errors from each test because the overlap exists among tests.
[3] The pseudo-NDVI and NDDI is only applied over land.

3.3.2 Flowchart

Fig. 3.8 is the flowchart of smoke detection algorithm. The whole swath of L1B measurements is input and divided into two branches with land/sea mask product stored in L1A file: smoke over land and smoke over ocean. In land branch, the process is comprised with four tests, orderly for classifying vegetation, soil, cloud, and noise (including water). The first test employs a pseudo-NDVI to examine vegetated pixel. The NDDI is applied in the second test for differentiating smoke from bright surface. In the third test, the BT11 and BTD (3.7, 11) are used to discriminate smoke from cloud, as well as the reflectance at the 1.38μm band. The goal of last module is to filter out the noise pixels (mainly water pixels) with the normalized Ratio (R3, R8) and single of reflectance of band 8. In ocean branch, the process is relatively easy, which is comprised of two steps only. At the end of process, an additional test named "noise-elimination test" is executed to further filter noise pixels. In view of the smoke continuity, although a pixel is identified as smoke pixel but it is not close to other smoke pixels, this pixel will be considered as noise pixels and deleted from smoke images.
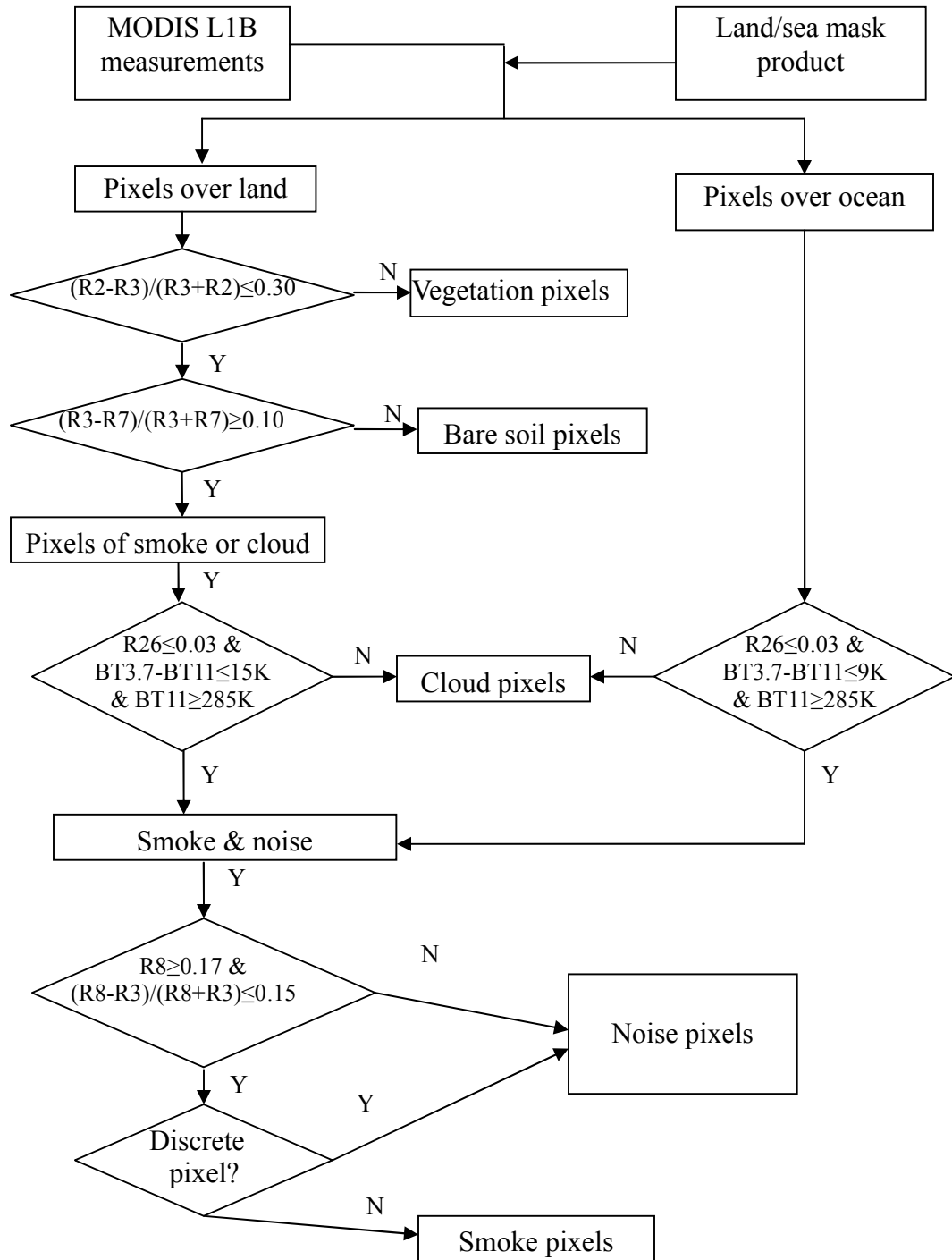
Figure 3.8: Flowchart of the multi-threshold method for smoke detection.

3.4 Results

3.4.1 Georgia 2007 fire

Smoke plumes caused by major wildfires in Georgia started on April 16, 2007 greatly impacted the local air quality, the public health, and even the climate to some extent. The Sweat Farm Road Fire, located ten miles southwest of the city of Waycross, Georgia, was caused by a tree limb suddenly fell down on a power line and, fanned by strong winds, quickly became a major fire. Prolonged drought conditions and record low water levels in the Okefenokee Swamp expedited this big wildfire burning with diversity of woods and vegetations. The Big Turnaround Fire was an extension of the Sweat Farm Road Fire, located 8 miles west of Folkston, Georgia and 10 miles south of Waycross, Georgia. The total burned areas of two major wildfires reach to 389,722 acres including 330,114 acres in the wildlife refuge (http://inciweb.org/incident/675/). Due to the danger from the rapidly growing blaze, thousands of residents in and around the town of Waycross were evacuated during the early days of this Georgia fire.

The consecutive smoke images of Georgia wildfires during April 19 to May 21 are generated at 1 km spatial resolution (http://eastfirelab.gmu.edu/gafire/). Several examples at different time and under different condition are displayed in Figs. 3.9 and 3.10. The smoke pixels are marked in blue color.

The MODIS has the capability of generating RGB true color image which could be used for validation. The true color images of 04/29/07 and 05/20/07 are also plotted in Fig. 3.9 and Fig. 3.10, respectively. Comparing smoke images with true color images, it

is clear that most of smoke plumes have been detected. In these smoke images, most smoke pixels are identified except some missing pixels located at the fire spots in which the temperature is abnormal. Some pixels located at the edge of plume with very weak magnitude are also missed.

The MODIS AOD product in MOD04 file is also shown in Figs 3.9 and 3.10 for the comparison. The spatial resolution of AOD product is 10 km. In the AOD images, the AOD values were accurately retrieved with current algorithm over thin smoky area. However, the AOD results are not suitable for those areas under heavy smoke layer, with invalid values in selected cases. Since AOD retrieval algorithm is performed after cloud mask, some smoke areas close to cloud or mixed with cloud may masked out so that smoke areas in these areas are missed.

Based on the resulting smoke images, the spread direction and growth of smoke plumes could be monitored by combining consecutive measurements from both Terra and Aqua MODIS; one is in the morning time and the other is in the afternoon time. An example with six smoke images (from Fig. 3.11a to Fig. 3.11f) at the same resolution and cover area, display the dispersion and magnitude of smoke plumes during three consecutive days, from day April 21 to April 23. In the first day (April 21), the smoke is fairly strong and spread directly towards southwest in the morning, and became weaker at the same spread direction in the afternoon. The dispersion direction changed from southwest to northwest and the magnitude of smoke plume became weaker and weaker with small fluctuation during the following two days.
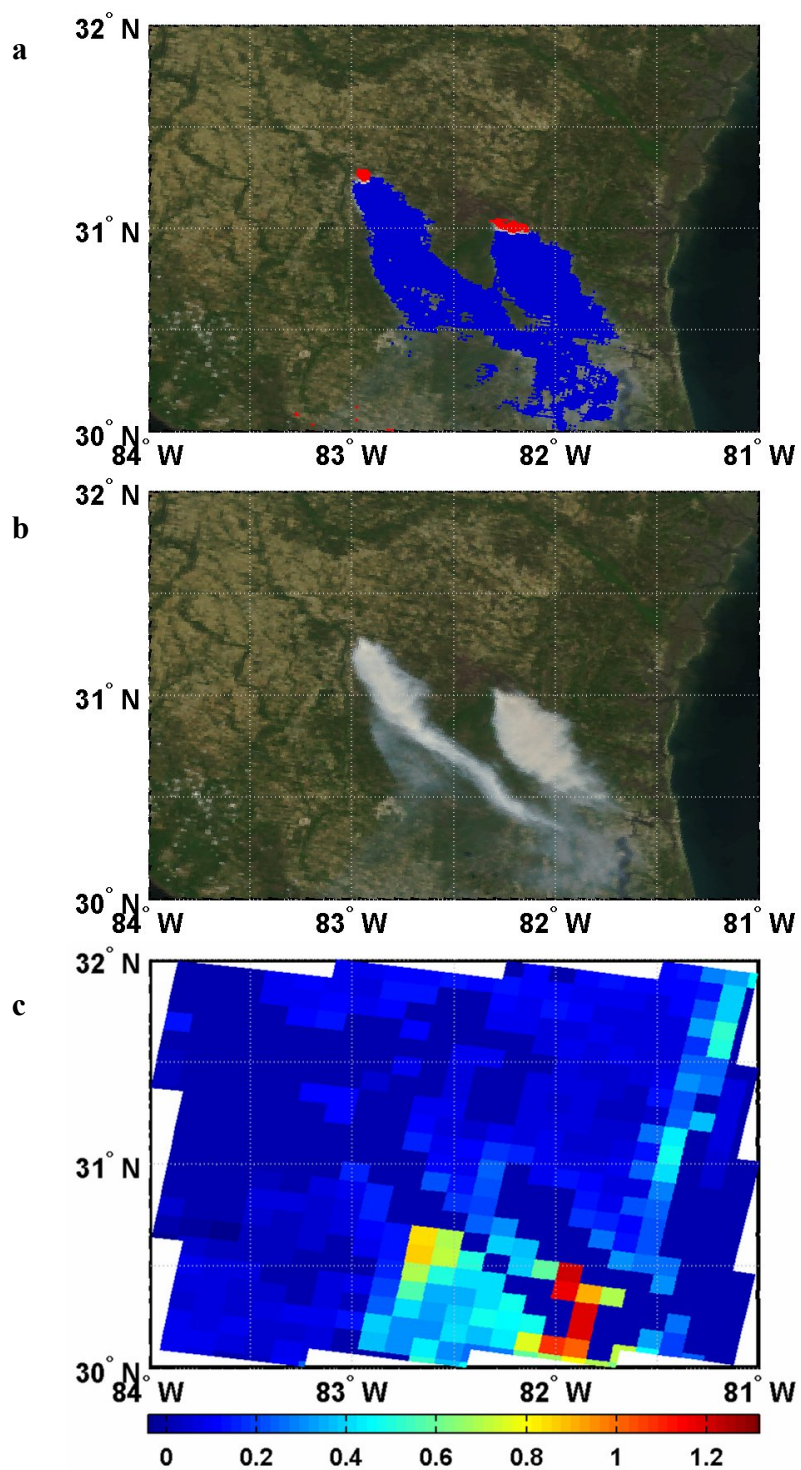
Figure 3.9: Smoke images on 04/29/07 (a) Smoke image at 1 km resolution; (b) MODIS true color image at 1 km resolution; (c) MODIS AOD image at 10 km resolution.
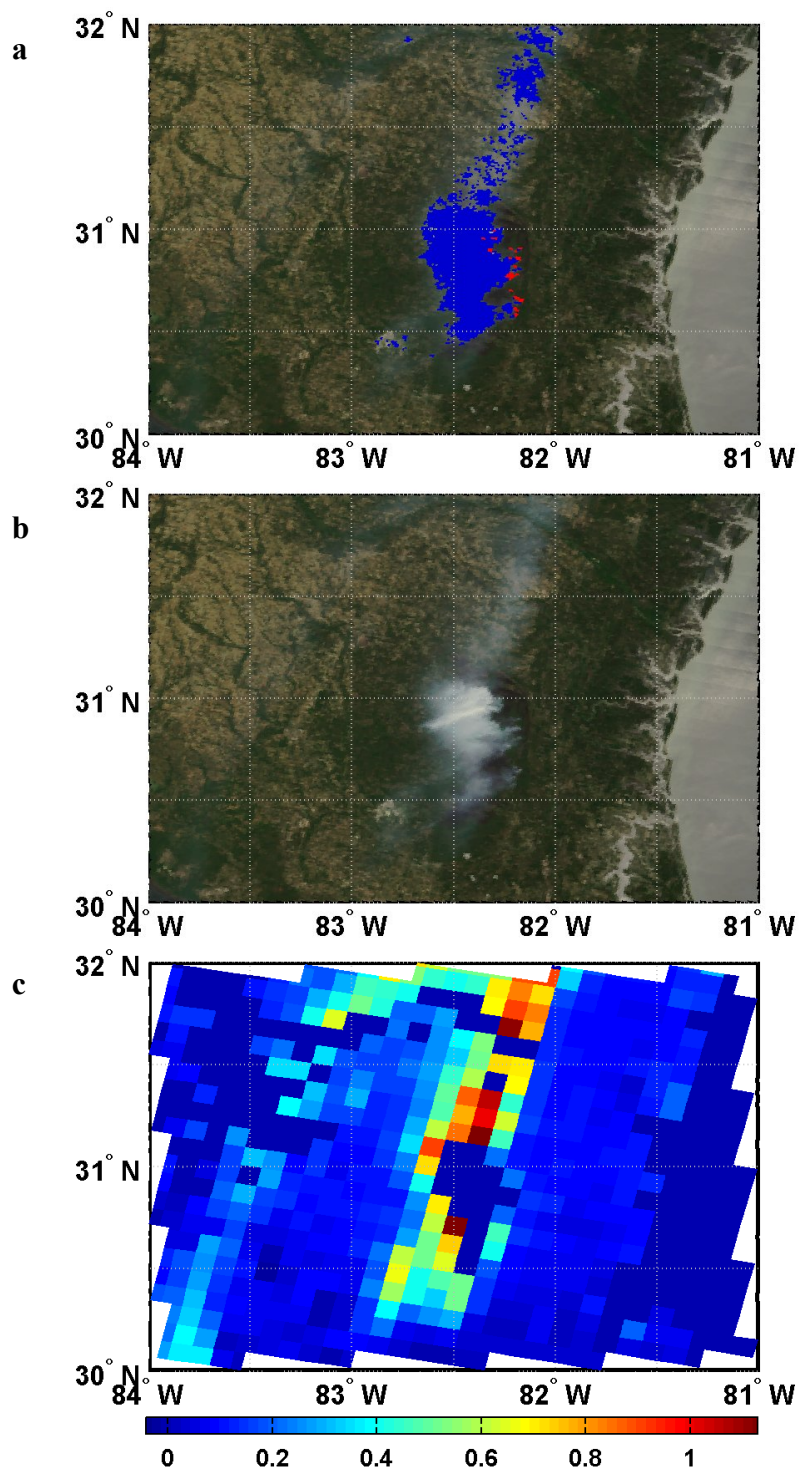
Figure 3.10: Smoke images on day 05/20/07 (a) Smoke image at 1km resolution (b) MODIS true color image at 1 km resolution; (c) AOD image at 10 km resolution.
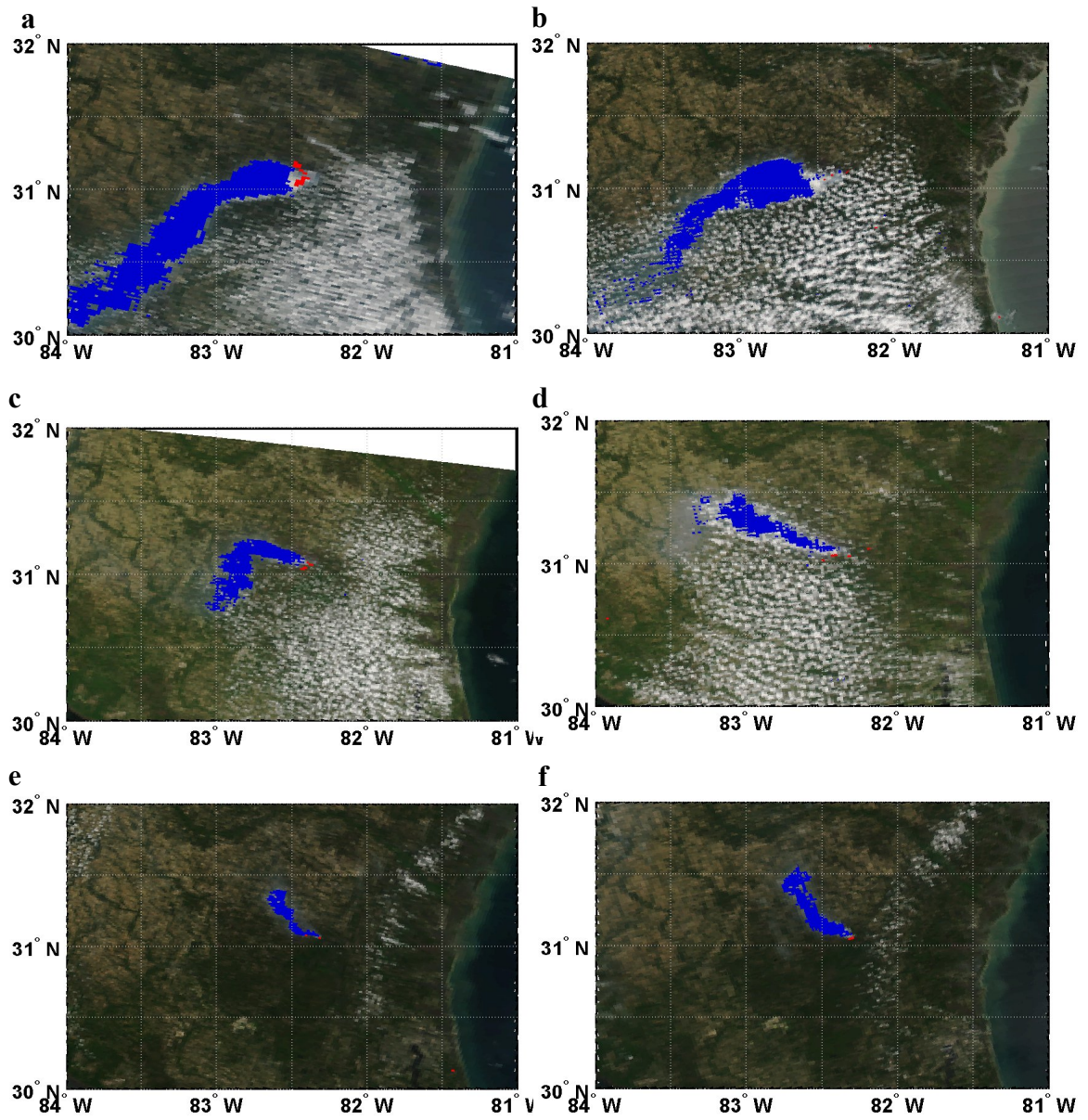
Figure 3.11: The example with six smoke images is used to investigate the dispersion of smoke plume in consecutive three days, from day April 21 to April 23. (a) Smoke on April 21 (Terra); (b) Smoke on April 21 (Aqua); (c) Smoke on April 22 (Terra); (d) Smoke on April 22 (Aqua); (e) Smoke on April 23 (Terra); (f) Smoke on April 23 (Aqua).

3.4.2 California 2007 fire

The 2007 California wildfires, stated on October 20, was a major wildfire that burned across Southern California. The fires brought significant economic and vital loss to the society. At least 1,500 homes were destroyed (Flaccus, 2007) and over 500,000 acres of land were burned. Nine people died and 85 others were injured, including at least 61 firefighters (CNN, 2007). The Witch fire and the Harris fire are the two biggest located in San Diego County of all the fires. The Witch Creek Fire, the largest of the October 2007 wildfires, started in Witch Creek Canyon and quickly spread to other areas with strong wind. Strong Santa Ana winds, over 100 mph (160 km/h), pushed the fires west towards the coast (martinez et al., 2007). Many major roads were also closed as a result of fires and smoke (http://en.wikipedia.org/wiki/California_wildfires_of_October_2007).

The detected smoke plumes of California fire on October 22 at UTC time 19:20 (Terra) and on October 23 at UTC time 21:40 (Aqua) are plotted in the Fig. 3.12, as well as the true color images. The detection results clearly show the huge smoke plume is floated over Pacific Ocean. Although the accuracy of detection results over ocean (dark surface) is not as good as that over land according to the Table 3.2, the algorithm observes most areas covered with dense smoke plume.
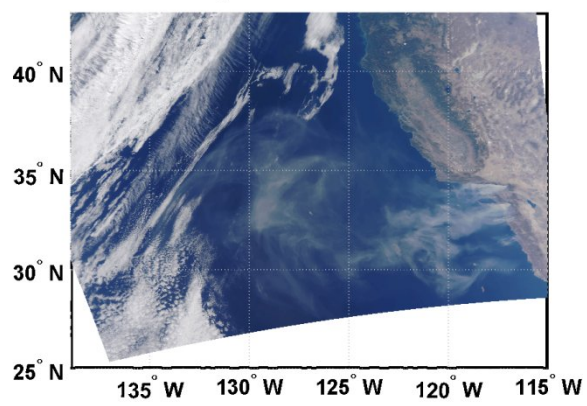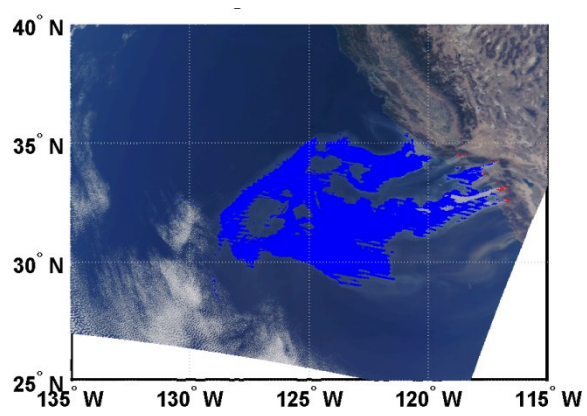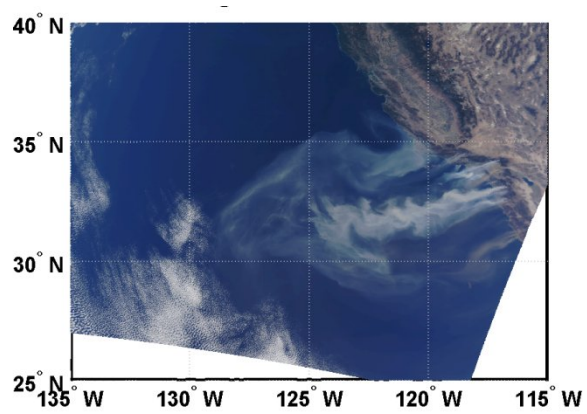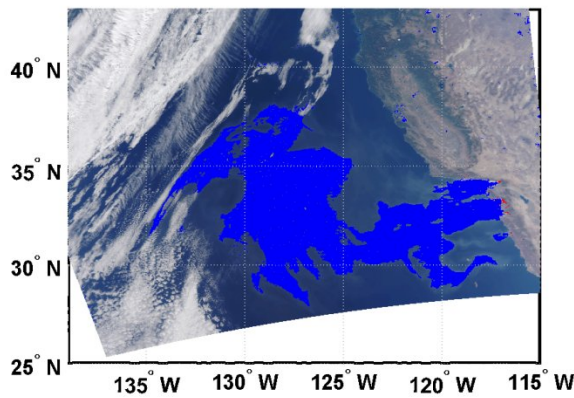
Figure 3.12: Smoke images of 2007 California Fire on October 22 captured by Terra MODIS (upper row) and on October 23 captured by Aqua MODIS (bottom row). The left column is the MODIS true color images and the right column is the smoke images.

3.5 Chapter Summary

Large scale smoke plume from wildfires is a frequently occurred phenomenon in the nature, releasing large amount of harmful gases and matters into the air. Detecting smoke plume timely using satellite remote sensing measurements is explored. An algorithm based on multi-spectral technique is developed combining measurements of both MODIS RSBs and TEBs, aiming to detect smoke plumes over both land and ocean.

In the algorithm, the process is divided into two branches, smoke over land and smoke over ocean. The tests and thresholds of each branch are decided based on the spectral and statistical analyses of training data. In the algorithm, several blue bands are used jointly or separately since they are sensitive to smoke. On the other hand, cloud module is introduced to mask cloud to observe smoke located close to cloud or mixed with cloud.

The multi-spectral approach is tested and validated with plumes from major wildfires in Georgia and California. The resulting smoke images are compared with MODIS true color images. In these smoke images, most smoke pixels are identified correctly except some missing pixels. Since smoke plumes over ocean usually become weaker during their transportation from land, the accuracy over the ocean is lower than over land.

Pairs of smoke images generated from both Terra and Aqua measurements in consecutive days provide a good opportunity to monitor the characteristics change of the smoke. These continuous smoke images give the general information about smoke, such as spread direction and distance, shape, and intensity change. It is valuable to perform further dynamic analysis of smoke aerosol in the future by combining the real time wind information. Additionally, the results of smoke detection have been applied to other applications, such as detecting cooling fires in the southeastern United States (Wang et al, 2007).

CHAPTER 4

DUST AEROSOL MONITORING WITH MODIS MEASUREMENTS

Asian dust storm, originates in Mongolia and northern China and Kazakhstan, is a seasonal meteorological phenomenon. Every year, thousands of tons of dust are transported by the prevailing winds in springtime into eastern China, North and South Korea, and Japan, and Pacific Ocean. Sometime, these airborne dust particulates impacted the air quality as far as the North American. The severe dust storms transported by wind great impact the financial trade, industrial production, transportation, daily activity, and endanger human's life. Detection dust storm in a timely manner can give alarm to people to take measures to avoid economic even vital loss. The detecting results are also very useful for the atmospheric modeling and simulation. An algorithm based on multi-spectral technique is developed combining measurements of six MODIS RSBs and TEBs. Similar to the development of smoke detection algorithm, the bands are selected according to the spectral analysis and the thresholds of each test are decided with the statistical analysis. Several dust storm events are selected as example cases to test the algorithm. The results are validated with MODIS true color images in this chapter and validated quantitatively with multi-sensor measurements in chapter six.

4.1 Physical Principle of Dust Aerosol Detection

4.1.1 Data collection

In order to accurately decide the bands and thresholds in the algorithm of dust aerosol detection, more than fifty dust storm events occurred in China during 2001- 2007 (2001-2007 for Terra MODIS and 2002-2007 for Aqua MODIS) are collected as training data for spectral analysis. The detail information of each selected dust storm event is listed in Table 4.1, including the sensor, year, day, and UTC time. Cloud pixels and clear pixels are also collected, written in Tables 4.2 and 4.3, based on the MODIS cloud mask product.

Table 4.1: Dust storm events selected as training data for spectral and statistical analyses.

MODIS	Year	Julian/Calendar	UTC	MODIS	Year	Julian/Calendar	UTC
Aqua	2002	234-08/22	06:50	Terra	2001	096-04/06	03:40
Aqua	2002	239-08/27	07:10	Terra	2001	098-04/08	05:05
Aqua	2002	290-10/17	07:40	Terra	2001	100-04/10	06:30
Aqua	2002	299-10/26	07:50	Terra	2002	106-04/16	05:15
Aqua	2003	107-04/17	07:00	Terra	2002	113-04/23	05:20
Aqua	2003	108-04/18	07:45	Terra	2002	114-04/24	06:05
Aqua	2004	120-04/30	07:40	Terra	2003	107-04/17	05:25
Aqua	2005	030-01/30	07:15	Terra	2004	329-11/24	05:05
Aqua	2005	118-04/28	06:25	Terra	2004	330-11/25	05:45
Aqua	2005	173-06/22	06:30	Terra	2005	030-01/30	05:35
Aqua	2005	176-06/25	07:00	Terra	2005	155-06/04	05:05
Aqua	2006	100-04/10	06:05	Terra	2005	17606/25	05:25
Aqua	2006	101-04/11	06:50	Terra	2006	045-02/14	05:05
Aqua	2006	103-04/13	06:40	Terra	2006	100-04/10	04:30
Aqua	2006	113-04/23	07:15	Terra	2006	101-04/11	05:10
Aqua	2006	207-07/26	07:30	Terra	2006	102-04/12	04:15

Aqua	2007	089-03/30	06:00	Terra	2006	105-04/15	04:45
Aqua	2007	090-03/31	05:00	Terra	2006	120-04/30	05:40
Aqua	2007	106-04/16	08:20	Terra	2006	124-05/04	05:20
Aqua	2007	113-04/23	06:45	Terra	2007	090-03/31	03:20
Aqua	2007	113-04/23	08:25	Terra	2007	091-04/01	05:45
Aqua	2007	130-05/10	07:30	Terra	2007	092-04/02	04:50
Aqua	2007	131-05/11	08:10	Terra	2007	106-04/16	05:00
Terra	2001	061-03/02	06:25	Terra	2007	113-04/23	05:05
Terra	2001	064-03/05	03:40	Terra	2007	120-04/30	03:30
Terra	2001	094-04/04	05:30	Terra	2007	130-05/10	05:50
Terra	2001	096-04/06	03:35	Terra	2007	131-05/11	04:55

Table 4.2: Cloud events selected as training data for spectral and statistical analyses.

MODIS	Year	Julian/Calendar	Time	MODIS	Year	Julian/Calendar	Time
Aqua	2002	239-08/27	07:10	Terra	2001	064-03/05	03:40
Aqua	2003	107-04/17	07:00	Terra	2001	094-04/04	05:30
Aqua	2003	108-04/18	07:45	Terra	2001	096-04/06	03:35
Aqua	2004	070-03/10	04:35	Terra	2001	096-04/06	03:40
Aqua	2004	087-03/27	05:15	Terra	2001	09704/07	02:40
Aqua	2004	087-03/27	05:20	Terra	2001	098-04/-8	03:25
Aqua	2004	119-04/28	05:20	Terra	2001	238-08/26	05:25
Aqua	2004	120-04/29	07:40	Terra	2002	006-01/06	05:40
Aqua	2005	118-04/28	04:45	Terra	2002	097-04/07	02:00
Aqua	2005	118-04/28	06:25	Terra	2002	097-04/07	03:40
Aqua	2005	119-04/29	03:50	Terra	2002	113-04/23	05:20
Aqua	2005	119-04/29	05:20	Terra	2002	120-04/30	05:25
Aqua	2005	120-04/30	02:55	Terra	2004	330-11/25	04:10
Aqua	2005	121-05/01	03:35	Terra	2004	330-11/25	05:45
Aqua	2005	173-06/22	04:55	Terra	2005	118-04/28	04:45
Aqua	2006	043-02/12	06:10	Terra	2005	119-04/29	02:10
Aqua	2006	096-04/06	04:45	Terra	2005	119-04/29	03:50
Aqua	2006	100-04/10	06:05	Terra	2005	120-04/30	01:15

Aqua	2006	102-04/12	04:15	Terra	2005	120-04/30	02:25
Aqua	2006	107-04/17	04:35	Terra	2005	173-06/22	03:15
Aqua	2006	108-04/18	05:15	Terra	2005	177-06/26	06:05
Aqua	2006	109-04/19	04:20	Terra	2005	198-07/17	04:45
Aqua	2006	113-04/23	07:15	Terra	2005	310-11/06	03:05
Aqua	2006	149-05/29	05:10	Terra	2006	091-04/01	03:00
Aqua	2006	149-05/29	05:15	Terra	2006	097-04/07	02:15
Aqua	2007	083-03/24	04:55	Terra	2006	102-04/12	04:15
Aqua	2007	089-03/30	05:55	Terra	2006	107-04/17	02:55
Aqua	2007	089-03/30	06:00	Terra	2006	120-04/30	05:40
Aqua	2007	090-03/31	05:00	Terra	2006	124-05/04	05:20
Aqua	2007	106-03/16	08:20	Terra	2007	090-03/31	03:20
Aqua	2007	113-03/23	06:45	Terra	2007	091-04/01	05:45
Terra	2001	106-03/16	06:25	Terra	2007	120-04/30	01:55
Terra	2001	061-03/02	03:40	Terra	2007	120-04/30	03:30

Table 4.3: Clear scene selected as training data for spectral and statistical analyses.

Dark clear pixels				Bright clear pixels			
MODIS	Year	Julian/Calendar	Time	MODIS	Year	Julian/Calendar	Time
Aqua	2004	087-03/27	05:15	Aqua	2002	239-08/27	07:10
Aqua	2004	119-04/28	05:10	Terra	2001	238-08/26	05:25
Aqua	2006	097-04/07	05:35	Terra	2001	298-10/25	05:50
Aqua	2006	098-04/08	04:40	Terra	2001	300-10/27	05:35
Aqua	2006	149-05/29	05:10	Terra	2002	006-01/06	05:40
Terra	2001	079-03/20	02:55	Terra	2002	120-04/30	05:25
Terra	2001	107-04/17	03:20	Terra	2006	119-04/29	05:00
Terra	2002	091-04/01	02:40	Terra	2006	124-05/04	05:20
Terra	2005	118-04/18	03:10	Terra	2006	133-05/13	05:10
Terra	2005	119-04/19	02:10	Terra	2007	113-04/23	05:05
Terra	2005	173-06/22	03:15	Terra	2007	130-05/10	0550
Terra	2005	310-11/06	03:05	Terra	2007	131-05/11	04:55
Terra	2007	120-04/30	03:30				

4.1.2 Spectral curves

According to selected cases, most Asian dust storms originate and dissipate within the inland areas. In this manner, the dust events selected as training data are roughly divided into two categories using land surface types dataset: dust storm over bright surface and over dark surface. The spectral curves of these two categories of dust are shown in Fig. 4.1, as well as those of clouds and clear scenes. The spectral response at each band is the statistical mean value of all training data, and the standard deviation as well. In Fig. 4.1, cloud shows a high reflectivity in band 3 and low reflectivity in band 7, while dust displays a reverse trend. In thermal spectrum, cloud has much lower BT than dust. This difference assists their separation significantly. In Figs. 4.2 and 4.3, the relatively large response difference between dust and clear scene over both dark and bright surfaces is found at the band 1 (red channel). Additionally, the BTD (3.7, 11) value of dust is larger than that of clear scenes.

4.1.3 Band selection

The BT in LWIR between dust and cloud is obviously different. Ackerman (1997) proposed an "IR split windows" technique to discriminate the dust storm layer from cloud using the brightness temperature difference between the 11 and the 12μm regions of the spectrum. As illustrated in smoke detection section, the BTD (12, 11) value is negative for cloud. The BTD (12, 11) value is positive for dust based on the Ackerman's conclusion and also spectral curves in Fig. 4.1.

The dust has a high reflectivity at band 7 but a low reflectivity at band 3 (blue band). Contrarily, blue band is sensitive to cloud but band 7 is insensitive to cloud. This inverse spectral feature helps greatly for distinguishing dust and cloud. Qu et al. (2006) raised NDDI to detect dust, with the formula $NDDI = (R3 - R7) / (R3 + R7)$.

The BTD (3.7, 11) is selected to separate dust from surface scenes. Both dust and surface scenes have a similar BT at the band 20 (3.7μm) but dust has much lower BT at the LWIR than surface scenes. Among bands in LWIR, the BTD of band 31 (11μm) relative to band 20 has the largest statistical difference between dust and surface scenes.

Moreover, in reflective solar spectrum the relative large reflectance difference between dust and surface scenes (both bright and dark surfaces) is found at band 1. Therefore, the single reflectance of band 1 is picked up to differentiate dust from surface scenes.

Overall, the BTD (12, 11) and NDDI are chosen for discriminating dust and cloud, while BTD (3.7, 11) and the single reflectance of band 1 are chosen for identify dust over both dark and bright surfaces. In each branch, both RSBs and TEBs are used.
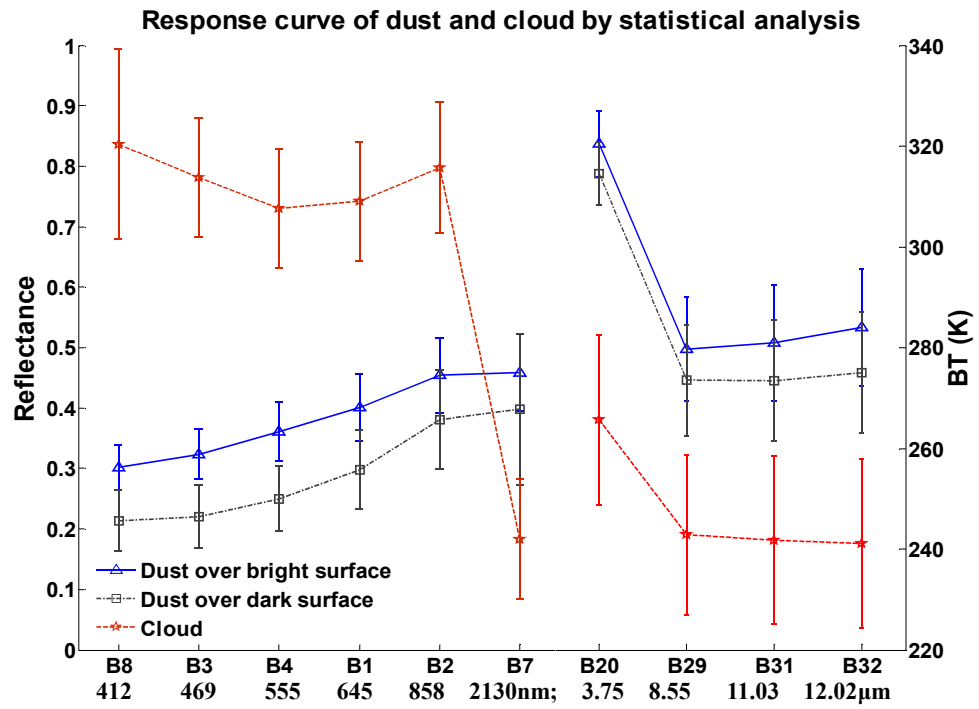
Figure 4.1: Response curves of dust and cloud.
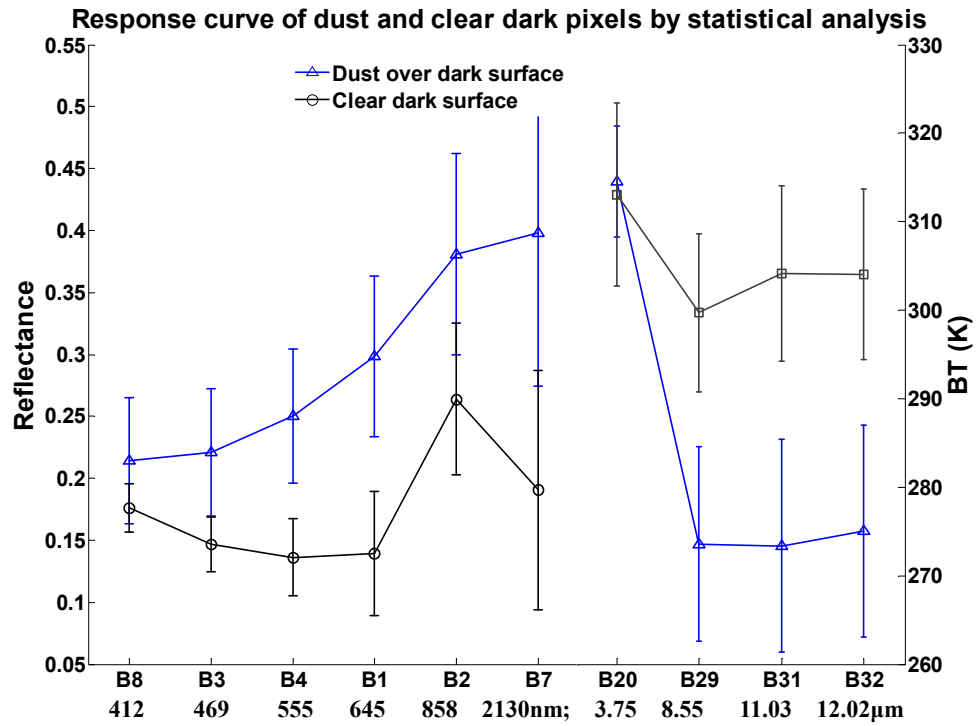
Figure 4.2: Response curves of dust and clear dark pixels.
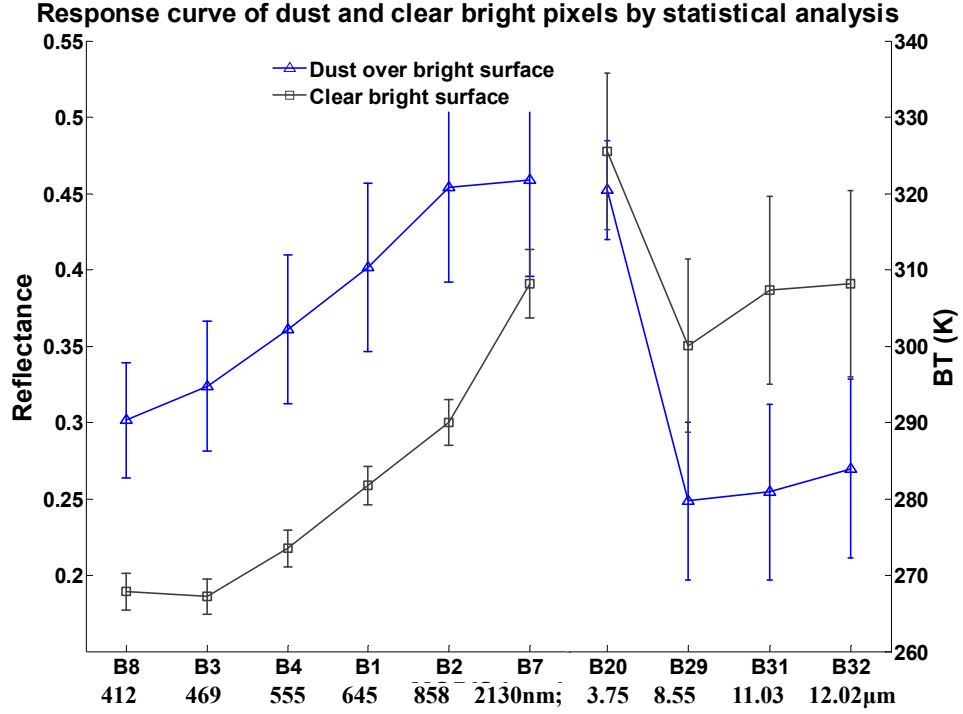
Figure 4.3: Response curves of dust and clear bright pixels.

4.2 Methodology

4.2.1 Threshold and accuracy analysis

The scatter plots of NDDI, BTD (12, 11), BTD (3.7, 11), and logarithm of single reflectance of band 1, are given in Fig. 4.4 to decide the thresholds of each test. Each data point is the average value of one dust events, along with standard deviation. Figs. 4.4a and 4.4b show a large difference of NDDI and BTD (12, 11) values between cloud and dust. Cloud has negative BTD (12, 11) and NDDI values while dust has positive values of these two indices contrarily. The dust has larger BTD (3.7, 11) values than clear bright surface (Fig. 4.4c) and clear dark surface (Fig. 4.4e). Among them, the BTD (3.7, 11)

53

values of dark surface is smallest, generally less than 20 K. In Figs. 4.4d and 4.4f, the logarithm of single reflectance of red band is introduced to separate dust from surface scenes. Using logarithm can enhances the resolving power of this index, especially in small reflectance range. Obviously, the Ln (R1) of most dust pixels is larger than -1.2 over bright surface, and -1.6 over dark surface.

The detail thresholds of each index are summarized in the Table 4.4. The thresholds are calculated statistically from all training data, namely selected dust events in China during 2001-2007. The errors caused by using the defined thresholds of each test are also listed in Table 4.4. The largest error is appeared at the separation of dust from cloud over dark surface in reflective solar spectrum, which is up to 12.484%. This big error caused possibly by light dust pixels suspended over water. Considering that some pixels can be counted repeatedly, the total errors of both over bright and dark surfaces are not equal to the summation of errors from each test.

4.2.2 Flowchart

The flowchart of dust detection algorithm is shown in Fig. 4.5. The L1B measurements are input into cloud module to filter out cloud first by employing BTD (12, 11) and NDDI. The remaining pixels are then divided into two branches based on pre-stored surface type information: dust over bright surface and over dark surface. The BTD (3.7, 11) and the logarithm of reflectance at band 1 are applied in both branches with respective thresholds. At the end, a same "noise-elimination" process is executed to filter out discrete pixels.
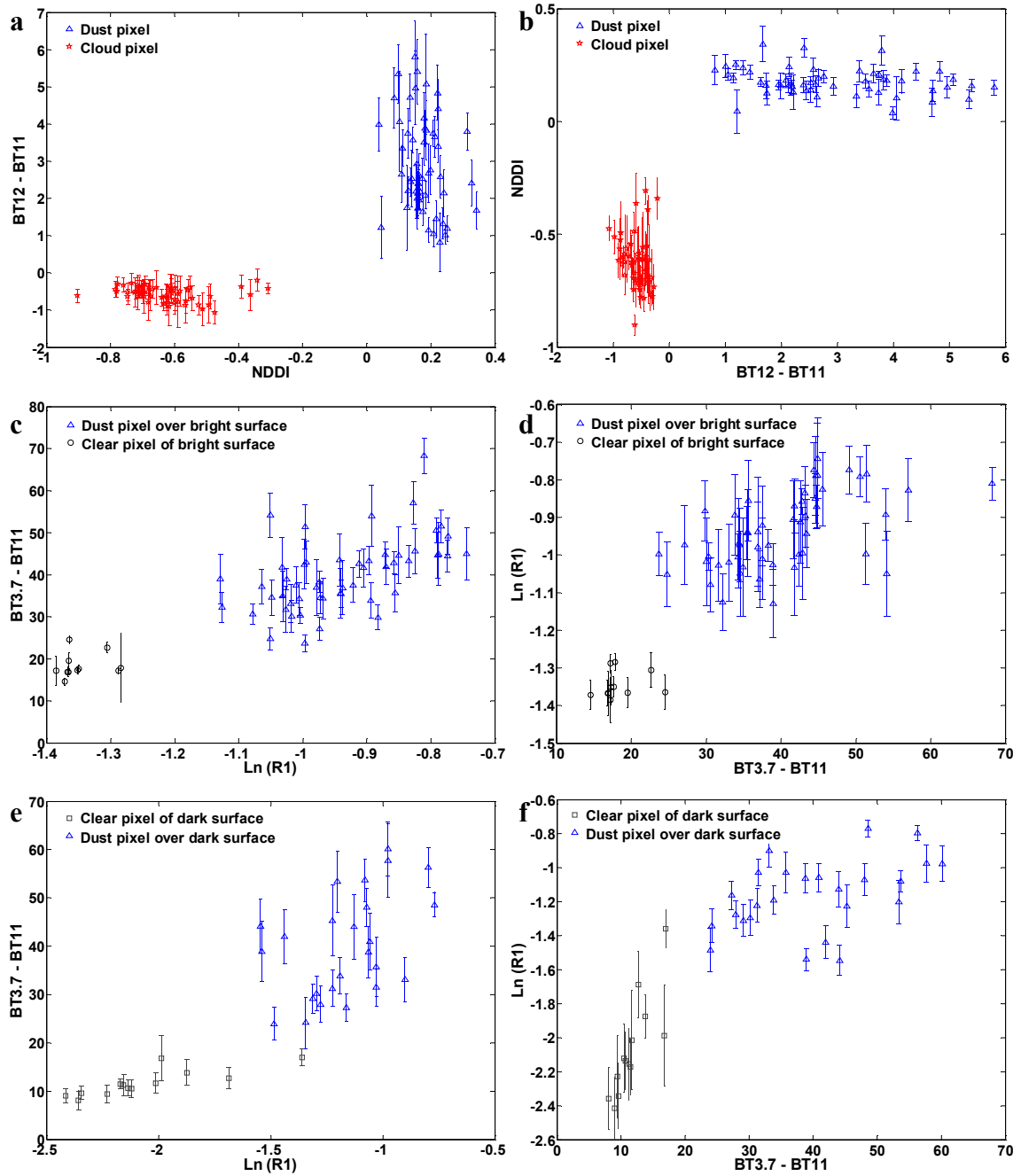
Figure 4.4 Statistical analyses of training data for deciding thresholds. (a)BTD (12, 11) values for dust and cloud; (b) NDDI values for dust and cloud; (c) BTD (3.7, 11) values for dust and clear pixels over bright surface; (d) Ln (R1) values for dust and clear pixels over bright surface; (e) BTD (3.7, 11) values for dust and clear pixels over dark surface; (f) Ln (R1) values for dust and dark pixels over dark surface.
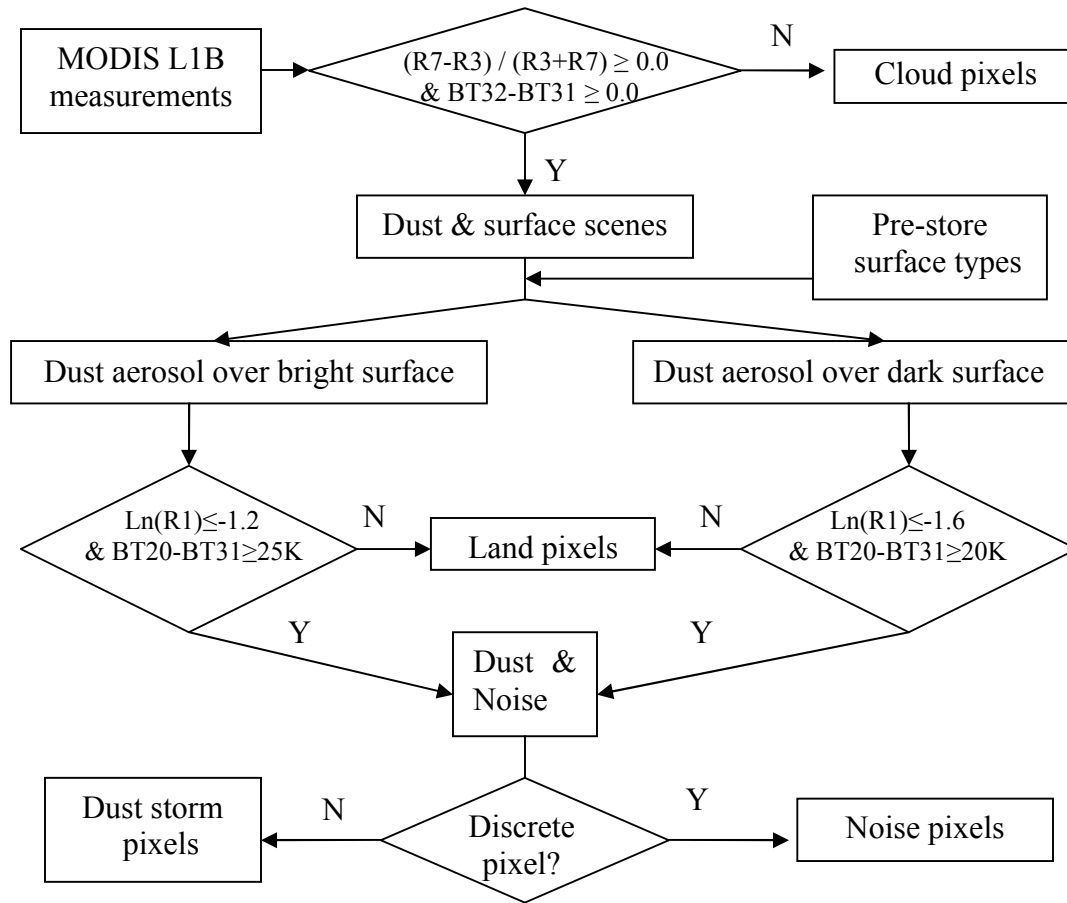
Figure 4.5: The flowchart of the dust storm detection

Table 4.4: The tests and thresholds used for detecting dust storm; and sensitivity analysis based on the selected dust storm events in China during years 2001-2007.

Class Type	Threshold test	Bright surface		Dark surface	
		Value	Error (%)	Value	Error (%)
Dust over land	BT 3.7 – BT 11	25 K	2.843	20 K	2.623
	& Ln (R1)	-1.2	2.294	-1.6	4.416
Cloud	(B7-B3) / (B3+B7)	0.0	1.886	0.0	12.484
	& BT 12 – BT 11	0 K	0.334	0 K	0.845
Total			[1]5.976		[1]17.717

[1] The total errors of both over bright and dark surface are not equal to the summation of errors from each test because the overlap exists among tests.

4.3 Results

Three dust events occurred in different locations are shown in Figs. 4.6, 4.7, and 4.8, separately. In Fig. 4.6, the dust storm is floated above the Takalimakan Desert, captured by Terra MODIS on June 25, 2005. The dust storm is blown in a long-narrow shape. The detected dust marked with black color in Fig. 4.6b has a good agreement with MODIS true color image (Fig. 4.6a). The dust in Fig. 4.7 is a large dust storm covered most part of northeastern China, captured by Terra MODIS on April 7, 2001. The dust storm mixed with cloud. With the NDDI and BTD (12, 11), the dust pixels (Fig. 4.7b) are separated obviously from cloud by comparing with MODIS true color image (Fig. 4.7a). Only small part of dust aerosol pixels over ocean (left bottom corner) is missed in that the algorithm is mainly focused on the land area. The dust storm in Fig. 4.8 spreads cross two countries, Pakistan and Afghanistan, on August 10, 2008. Two strings of dust plumes in the middle of image are identified successfully. Another small dust storm in the right upper corner is also detected.

The MODIS AOD images at the same region are displayed for the comparison, shown in Figs. 4.6c, 4.7c, and 4.8c. The spatial resolution of AOD product is 10 km. In the AOD images, the AOD is not accurately retrieved for the areas with heavy dust loading. Therefore, in this condition, the detecting results of this algorithm can provide more accurate information about the dust aerosol than the MODIS AOD product.

57

a

a

b

b

c
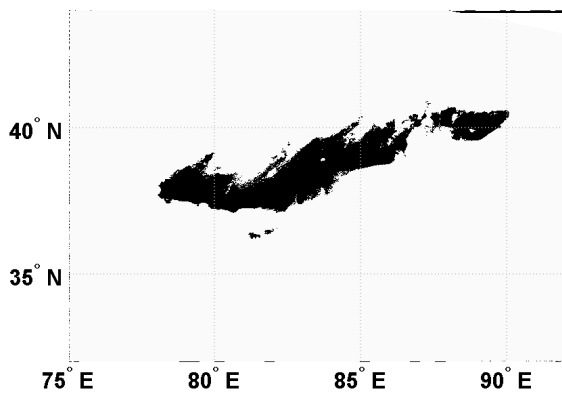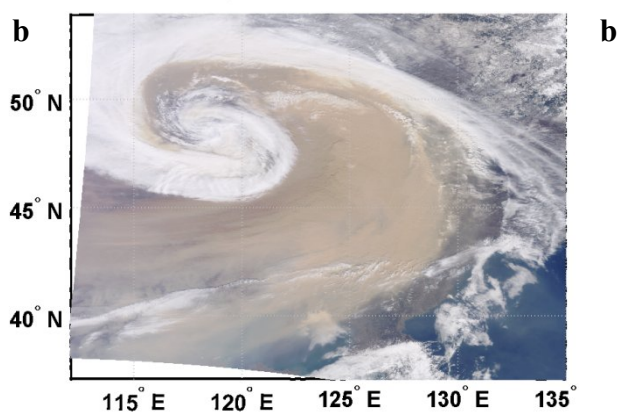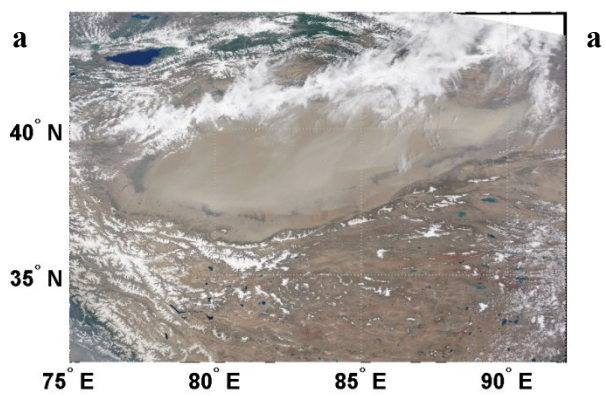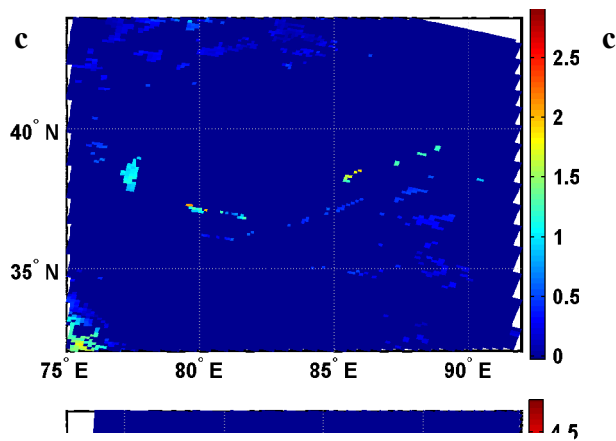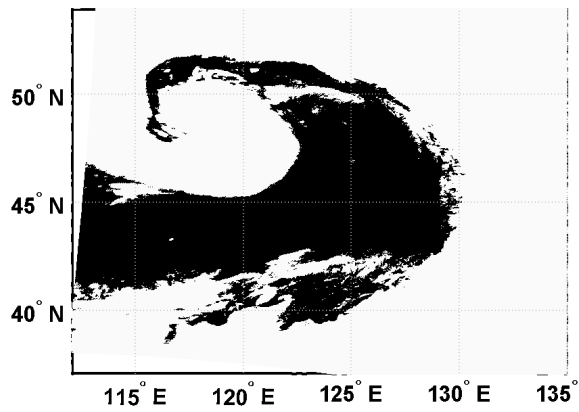
Figure 4.6: Dust storm over TAKLIMAKAN Desert on June 25, 2005. (a) MODIS true color image; (b) dust image; (c) AOT image.
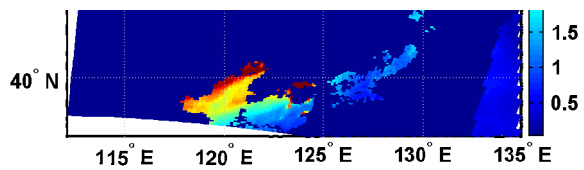
c

Figure 4.7: Dust storm in the northeastern China on April 7, 2001. (a) MODIS true color image; (b) dust image; (c) AOT image.
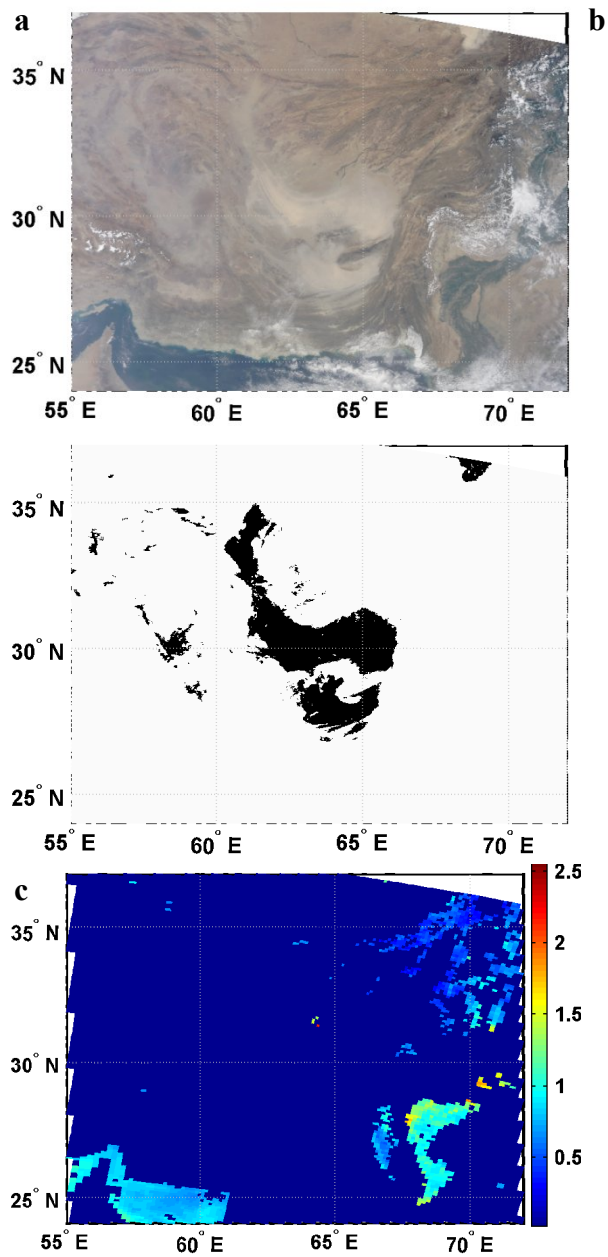
Figure 4.8: Dust storm cross Pakistan and Afghanistan on August 10, 2008. (a) MODIS true color image; (b) dust image; (c) AOT image.

4.4 Chapter Summary

In this chapter, the algorithm based on multi-spectral technique for detecting Asian dust aerosol is developed; combining measurements of six MODIS spectral bands in both solar and thermal spectrum. The algorithm is only focusing on dust storms over land areas so that it is roughly divided into two branches: dust over dark and bright surfaces. The identification of dust aerosol is performed by a series of threshold-test to filter out non-dust pixel step by step.

The spectral curves of several major scene types are obtained statistically with the large amount of training data collected from Asian dust storm events occurred during last several years. According to spectral curves, the dust displays unique features different from those of cloud and surface scenes. The NDDI and BTD (12, 11), two well-developed indices, are adopted directly for separating dust and cloud, because the values of these two indices are opposite for dust and cloud. To distinguish dust from surface scenes, the BTD (3.7, 11) and logarithm of reflectance of band 1 is introduced according to spectral analysis. The thresholds of these tests are defined with statistical analysis to seek the minimum error.

The algorithm is applied to several Asian dust events occurred in different areas. The resulting dust images are compared with MODIS true color images, showing a good agreement over both dark and bright surfaces. In these dust images, most dust pixels are identified correctly except some dust pixels which have relatively low magnitude. Moreover, the algorithm works well in the areas close to cloud even mixed with cloud.

CHAPTER 5

AEROSOL DETECTION BY COMBINING CALIPSO AND MODIS

MEASUREMENTS

Multi-sensor remote sensing, by its global and repetitive measurement capability, provides a large amount of valuable information for solving problems in various Earth observation applications. This massive amount of data allows the same features on the Earth to be observed by the several different sensors, yielding complementary information for more accurate measurements.

CALIPSO mission studies the role of aerosols and cloud in the Earth's climate system (Winker et al., 2003). It provides the vertical information about aerosols and cloud. The CALIPSO level 2 Vertical Feature Mask (VFM) (Vaughan et al., 2004) product provides detail vertical information about aerosol and cloud layer. It is easily used to separate dust from ground surface. However, limited by its spectral coverage, the misclassification may appear by labeling heavy dust aerosols as cloud in VFM product and reported by recent data quality statement (CALIPOS Lidar Level 2 Vertical Feature Mask products Version 2.01, January 25, 2008). The possible reason is that the intrinsic scattering properties of dust layers are similar to those of cloud in certain conditions. The Aqua MODIS has good spatial resolution and spectral coverage for detection large scale aerosol. It can provide the planar information about the dust storm. Both sensors are

operated in the A-train orbit with similar local equatorial crossing time. To fully take advantages of multi-sensor system, these two sensors, MODIS and CALIPSO, are combined together for Asian dust detection.

5.1 CALIPSO Instrument and Measurements

CALIOP is a lidar (LIght Detection And Ranging) sensor, namely a laser radar, providing information on the vertical distribution of aerosols and cloud as well as their optical and physical properties (Winker et al., 2003). Current remote sensing capabilities can be enhanced by the CALIPSO by providing global, vertically-resolved measurements of aerosol distribution. Cloud and aerosol layers can be discriminated easily using the magnitude and spectral variation of the lidar backscatter (Liu et al., 2004).

5.1.1 CALIPSO instrument

The CALIPSO mission was launched on April 28, 2006. It is flying at the same orbit as Aqua spacecraft with 1 minute and 15 seconds behind. The CALIPSO payload consists of three instruments: a two-wavelength, polarization-sensitive lidar (CALIOP), the Image Infrared Radiometer (IIR) and the Wide Field Camera (WFC) (Winker et al., 2003). The CALIPO is a two-wavelength polarization-sensitive lidar. It is designed to acquire the vertical profiles of aerosols with backscatter signal at 532 nm and 1064 nm in both daytime and nighttime, as well as profiles of linear depolarization at 532 nm. The IIR with three channels in the infrared window region is optimized for retrievals of cirrus particle size. The WFC has one visible channel that provides meteorological context and a means to accurately register CALIPSO observations to those from MODIS on the Aqua

satellite (Winker et al., 2004). The instrument performance parameters are given in Table 5.1, and the vertical and horizontal resolutions of the data products are shown in Table 5.2.

Table 5.1: Payload parameters

Payload	Characteristic	Value
CALIPSO	wavelengths	53 2nm & 1064 nm
	polarization	532 nm
	pulse energy	110 mJ
	footprint	70 m
WFC	wavelength	645 nm
	spectral bandwidth	50 nm
	IFOV / swath	125 / 61 km
IIR	wavelength	8.65 μm, 10.6 μm , 12.0 μm
	spectral bandwidth	0.6μm ~ 1.0μm
	IFOV / swath	1 km / 64 km

Table 5.2: Spatial resolution of CALIPSO data

Altitude Range (km)	Horizontal Resolution (km)	Vertical Resolution (km)
30.1 ~ 40.0	5.00	0.30
20.2 ~ 30.1	1.67	0.18
8.2 ~ 20.2	1.00	0.06
-0.5 ~ 8.2	0.33	0.03
-2.0 ~ -0.5	0.33	0.30

5.1.2 CALIPSO measurements and VFM product

The measurements of CALIPSO are free to public, from June 2006 to present. The size of each file (version 2.01) of daytime is around 500 Mb. The data provide such parameter as total attenuated backscatter at 532nm and 1064nm, perpendicular attenuated backscatter, height, elevation, latitude, longitude, and so on. Table 5.2 gives the measurable height relative to sea level. The vertical and horizontal spatial resolution varies with the height.

In CALIPSO measurements, total attenuated backscatter at 532nm and 1064nm and perpendicular attenuated backscatter at 532nm directly provide vertical information about aerosols. Fig.5.1 is an example to show CALIPSO attenuated backscatter signal at 1064nm on March 30, 2007. The horizontal axis stands for the geolocation of sample point and vertical axis represents the height relative to sea level. Usually, the value of attenuated backscatter is from $0.0001 \sim 0.1$.

Fig. 5.1 displays the CALIPSO attenuated backscattering signal at 1064 nm in the northwest China on July 26, 2006 at the UTC time 07:30. In the figure, the red solid line in horizontal direction is the elevation of the ground surface. A heavy aerosol (or cloud) over Taklimakan Desert is captured by CALIPSO, floating at the height of 2 -3 km from 38.27^0 N to 40.3^0 N. Heavy clouds are floating at the height of $7 \sim 8$ km in the south side of desert and at the height of 5 km in the north side of desert.

The VFM, level-2 product of CALIPSO, reports the scene classification based on the physical feature differences of aerosols and clouds. With the SCA (Scene Classification Algorithm), the atmospheric features are classified as either clouds or

aerosols and then the clouds and aerosols are separated into different subclasses (Omar et al., 2003). The VFM product can be shown in a two dimensional color-coded image, displaying the vertical and horizontal distribution of cloud and aerosol layers. The VFM product for the same region is given in Fig. 5.2. The colors stand for different scene features, listed as follow; 1: invalid (bad or missing data); 2: "clear air"; 3: cloud; 4: aerosol; 5: stratospheric feature; polar stratospheric cloud or stratospheric aerosol; 6: surface; 7: no signal (Currey et al., 2007).
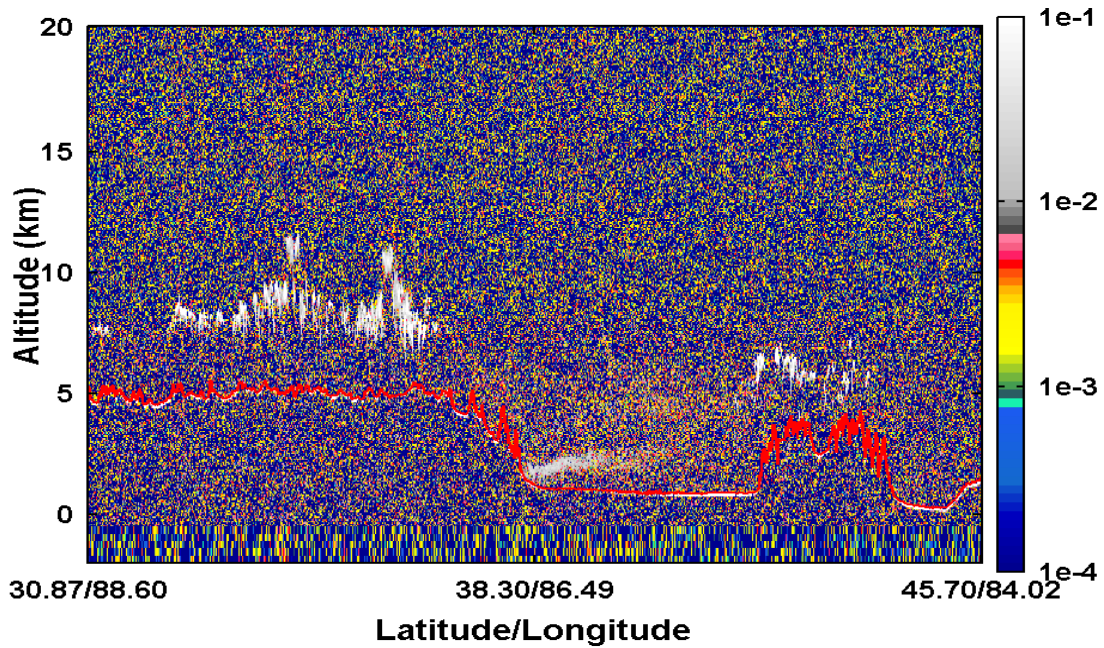
Figure 5.1: CALIPSO attenuated backscatter signal at 1064 nm on July 26, 2006.
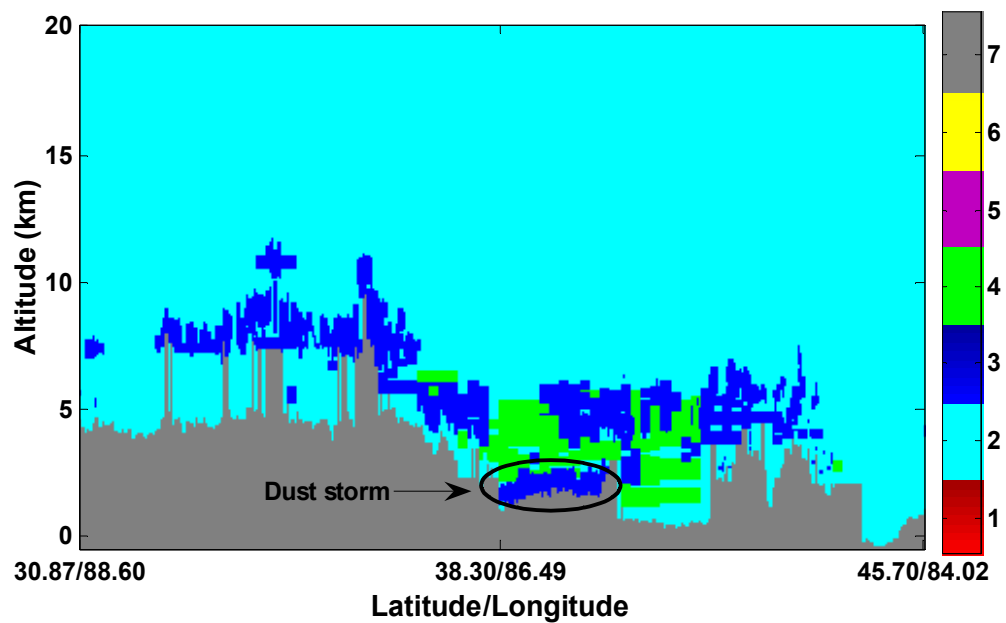
Figure 5.2: CALIPSO VFM data product on July 26, 2006.
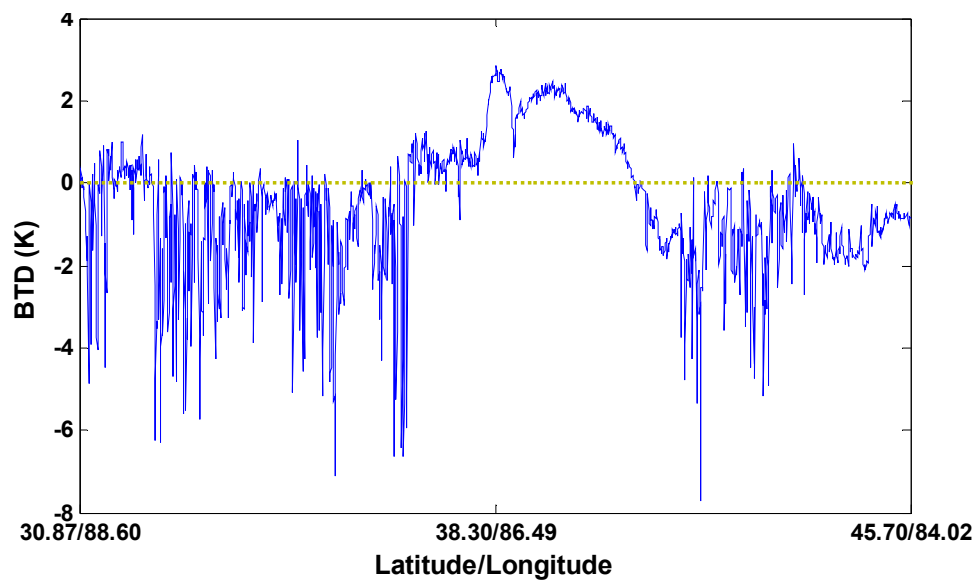
Figure 5.3: MODIS BTD (12, 11µm) values over the CALIPSO footprint on July 26,

2006.

5.2 Detecting Dust Storm with CALIPSO and MODIS Measurements

CALIPSO measures the vertical distribution of aerosols and clouds as well as their optical and physical properties, such as altitude, location, and aerosol optical depth. It is capable of separating airborne dust from ground dust. MODIS has been demonstrated as an effective sensor suitable for detecting dust aerosol. Since both Aqua MODIS and CALIPSO are operating in the A-train orbit with similar local equatorial crossing times, the temporal mis-registration between measurements of two sensors is quite small. The temporal registration is ignored in this dissertation. After spatial registration, three-dimensional information of dust can be obtained by combining MODIS and CALIPSO measurements.

5.2.1 Methodology

The MODIS BTD (12, 11) can be used to differentiate dust aerosol and cloud in both day and night time based on their physical feature difference in thermal spectrum. Generally, the values of BTD (12, 11) are positive for dust aerosol and are negative for cloud (Ackerman, 1997).

Due to the different field of view, the Aqua MODIS has much larger swath than CALIPSO. The footprint of CALIPSO is generally located in the near nadir of the MODIS swath. The spatial resolution is 1 km for Aqua MODIS, and 333 m for CALIPSO. Because of the spatial resolution is different between two sensors, the spatial mapping is performed firstly.

After spatial registration, the overlapped areas (namely over CALIPSO path) can be divided into two categories according to MODIS BTD (12, 11) values: BTD (12, 11) > 0 and BTD (12, 11) < 0. The comparison between measurements of two sensors is performed. If a layer is labeled as cloud in CALIPSO VFM product but it located in the area having positive BTD (12, 11μm) values, it is identified as dust aerosol.

5.2.2 Results

The same region is also observed by Aqua MODIS and shown with MODIS true color image in Fig. 5.4(a). The image is generated with measurements extracted from two swaths at UTC time 7:25 and 7:30. The dust aerosol is located at the eastern desert. The blue dash line is the footprint of CALIPSO in this area. It is clear that CALIPSO passes cross the dust aerosol. The BTD (12, 11μm) values of the same region is given in Fig. 5.4(b). And the BTD (12, 11μm) values over the CALIPSO footprint is given in Fig. 5.3. Obviously, the BTD (12, 11μm) values is larger than zero in the area having the latitude from 36.75^0 N - 40.80^0 N, which means dust aerosol is dominated in this area. Therefore, the dust aerosol in that area is identified and marked with dark circle in Fig. 5.2.

Fig. 5.5 gives the MODIS true color image of another case in which the dust aerosol aroused in the northeast China on March 30, 2007. The footprint of CALIPSO is plotted in blue dash line from equator to North Pole. The corresponding measurements of images are extracted partly from two MODIS swaths at the UTC time 05:55 and 06:00. The MODIS BTD (12, 11μm) image is plotted in Fig. 5.5(b) and corresponding BTD (12, 11μm) over CALIPSO footprint is given in Fig. 5.6. The CALIPSO is just passing through this dust storm. From MODIS true color image, the dust aerosol is overlapped

with cloud in some areas along the CALIPSO path. In the Fig. 5.6, the BTD (12, 11µm) is positive at three peaks with latitude 36.59^0 N - 39.79^0 N, 41.04^0 N - 44.02^0 N, and 44.640 N - 45.750 N, which is corresponding to dust aerosol areas. Between three peaks, the BTD (12, 11µm) is negative which corresponding to cloud. Therefore, four dust aerosol layers are found and marked with black circle in Fig. 5.7.

After the successful detection, the detail information about dust aerosol could be further retrieved. Fig. 5.8 shows the total attenuated backscatter signal profile at 532 nm in two locations: $(40^0$N, 109.16^0E) and $(42^0$N, 108.51^0E). The vertical profile for specific location gives more detail and accurate values about dust aerosols. At the first location, cloud (in dashed line rectangular) floated about 10.5 km above the sea level. At the latitude 42^0N, a large backscatter value at the altitude 2.5 km is corresponding to the dust storm. By integrating the measurements of both sensors, the vertical and horizontal information about dust aerosol can be retrieved. Table 5.3 summarized the vertical and horizontal information about dust aerosols occurred in 2008 spring season in northwest China, including height, averaged depth, width, and coverage.
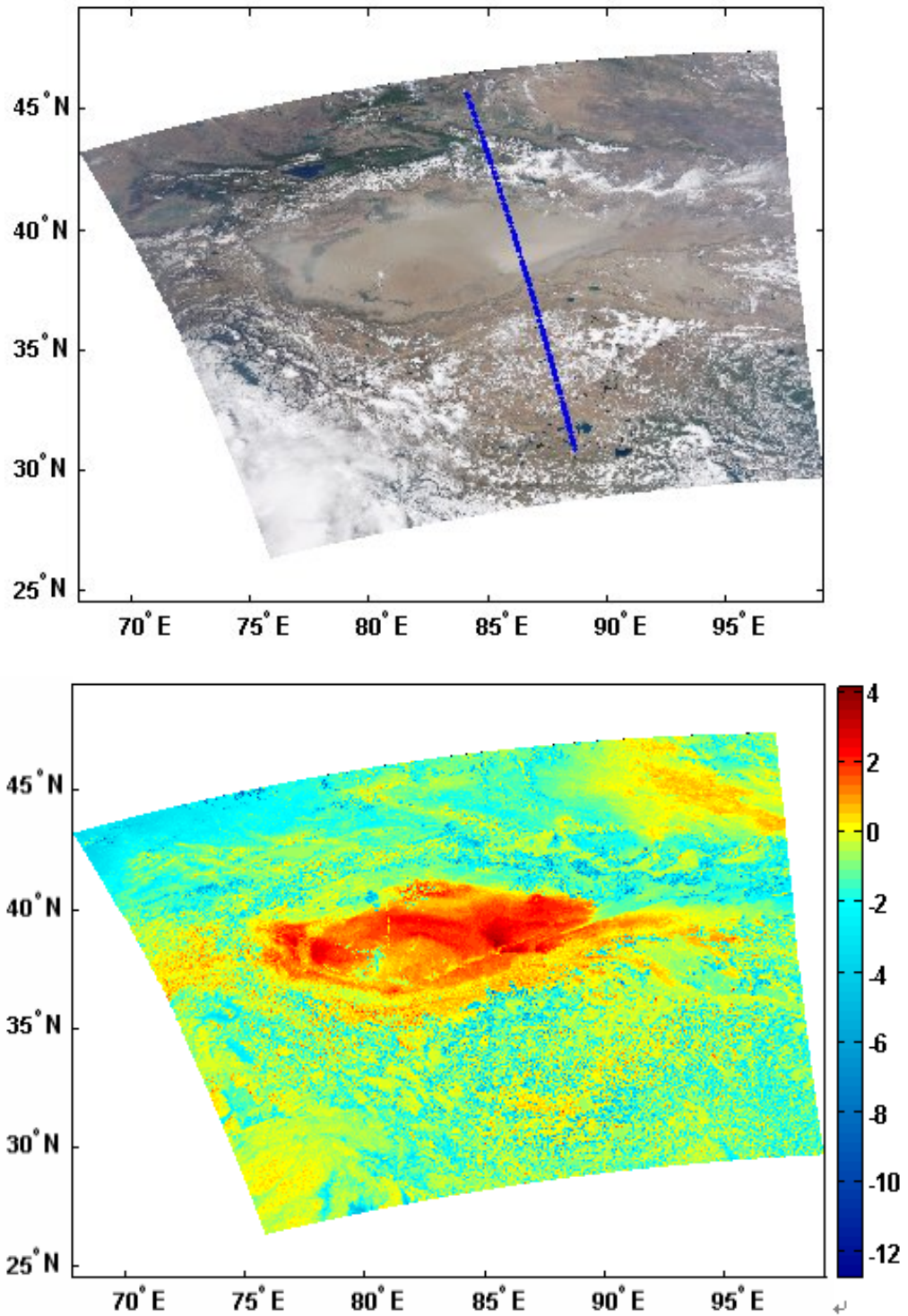
Figure 5.4(a) The MODIS true color image of dust storm in Taklimakan Desert on July 26, 2006. The blue solid line is the footprint of CALIPSO; (b) The corresponding BTD (12, 11μm) image of dust on July 26, 2006.
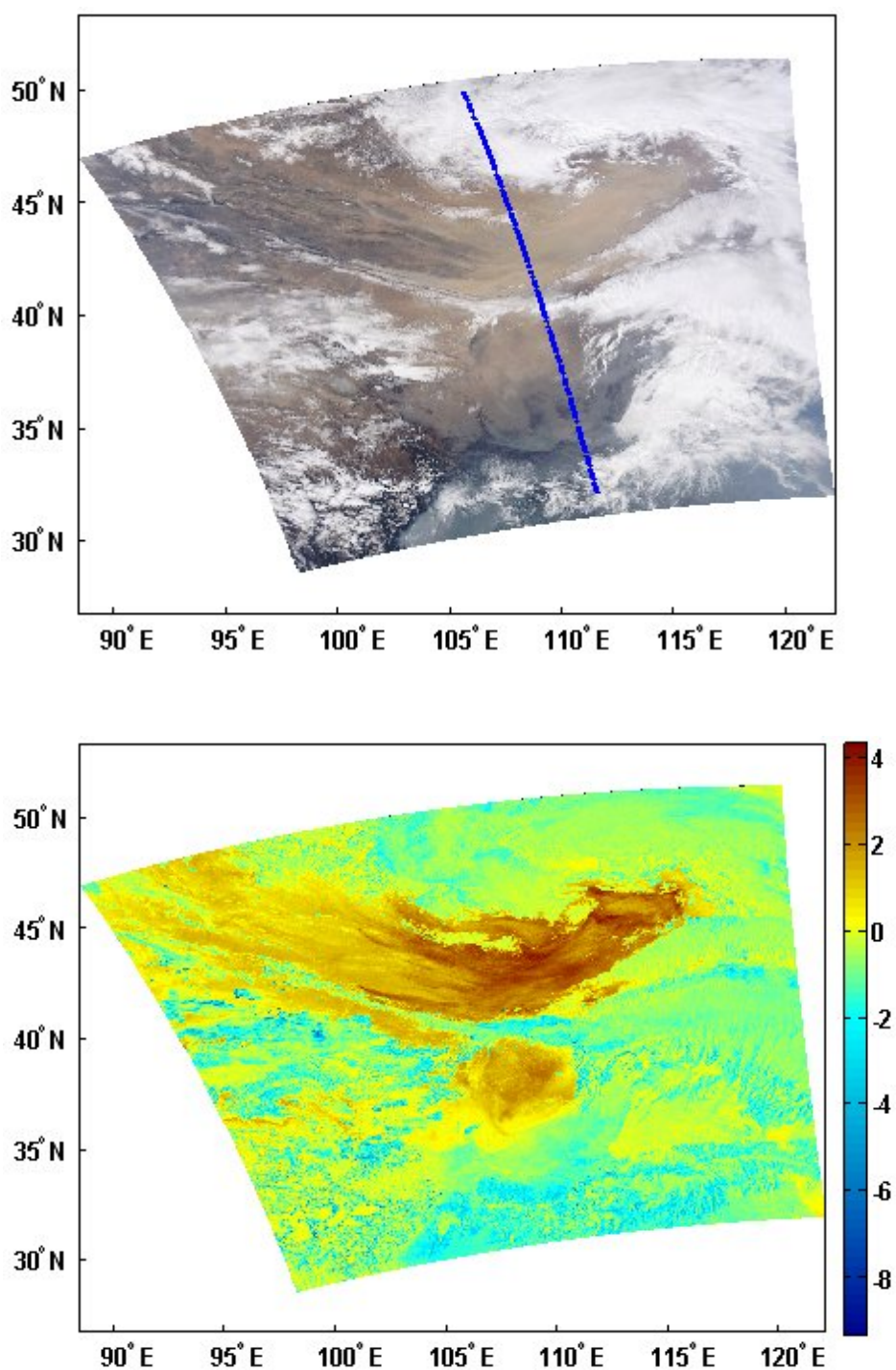
Figure 5.5(a) The MODIS true color image of dust storm in northeast China on March 30, 2007. The blue solid line is the footprint of CALIPSO; (b) The corresponding BTD (12, 11μm) image of dust on March 30, 2007.
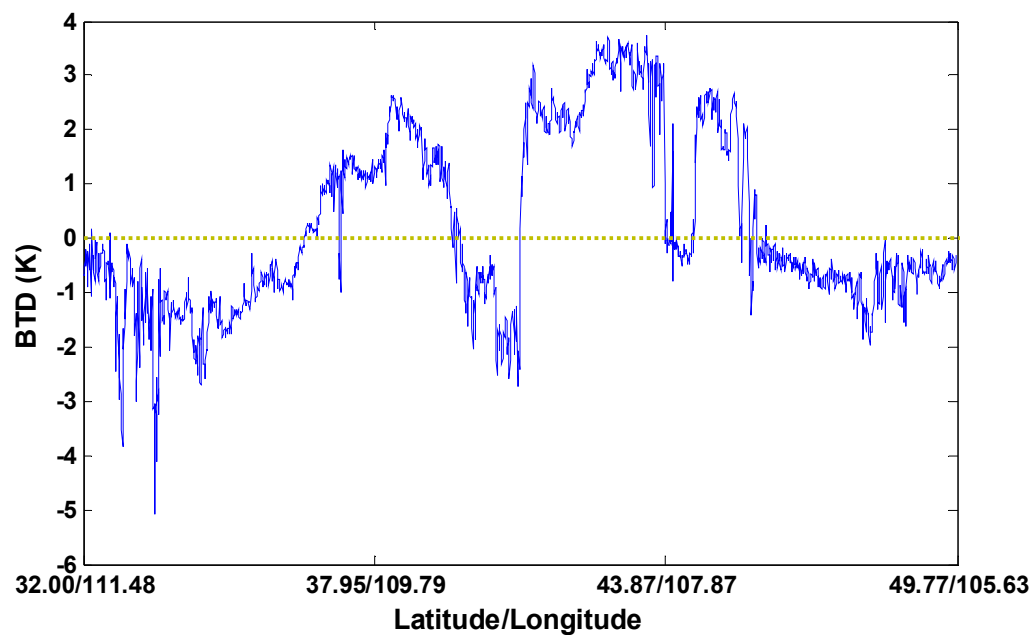
Figure 5.6: MODIS BTD (12, 11μm) values over the CALIPSO footprint on March

30, 2007.
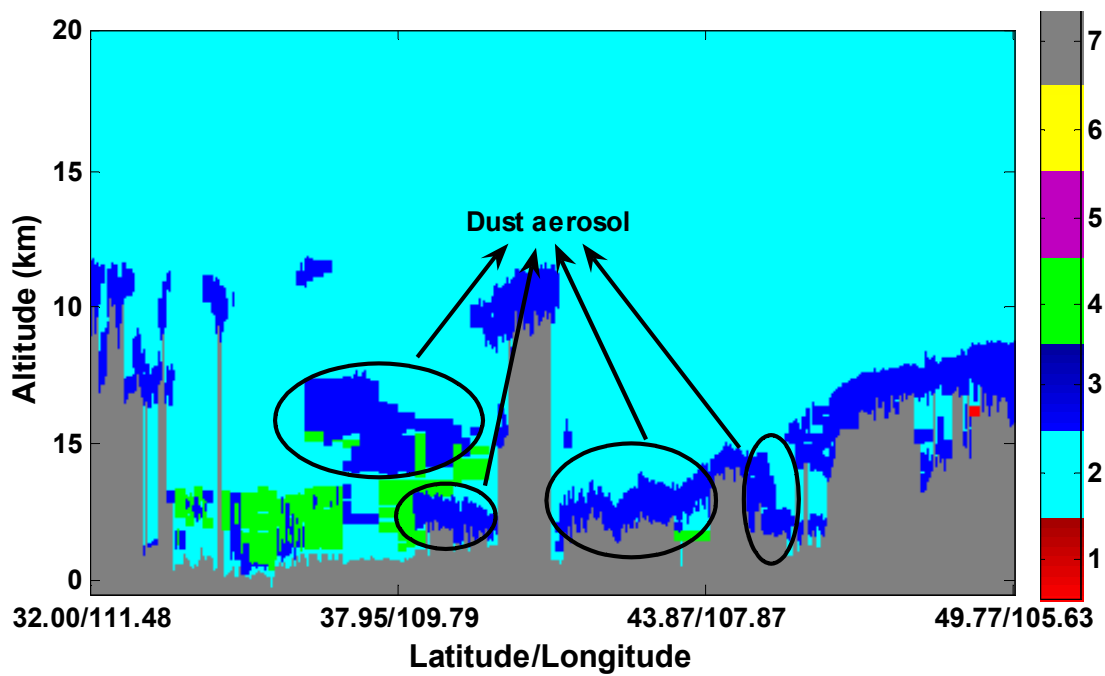
Figure 5.7: CALIPSO VFM data product on March 30, 2007.
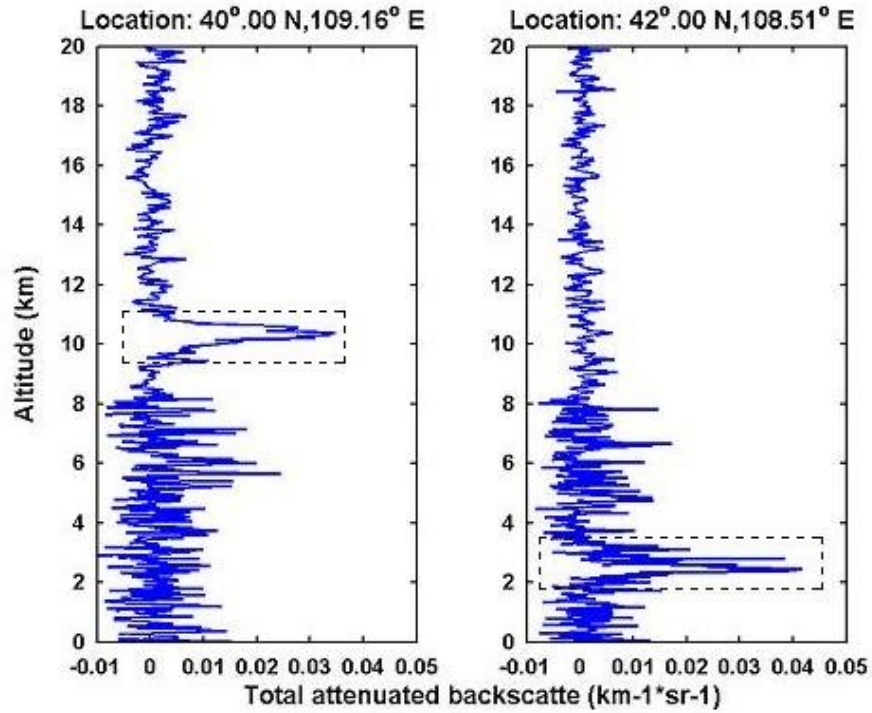
Figure 5.8: The total attenuated backscatter signal profile at 532 nm in two locations.

Table 5.3: Vertical and horizontal information about dust aerosols occurred in 2008 spring season.

Case	Date (UTC time)	Height (km)	Width (km)	Average depth (km)	Coverage (km^2)
1	Mar 29, 2008, 7:05	1.6 ~ 4.7	200	1.2	239113
2	Mar 30, 2008, 7:45	1.4 ~ 3.2	330	1.2	184081
3	Apr 19, 2008, 7:20	3.2 ~ 5.0	161	1.8	240236
4	Apr 20, 2008, 8:05	1.7 ~ 4.7	400	0.9	301729
5	Apr 28, 2008, 7:15	1.4 ~ 5.0	313	1.4	206002
6	May 5, 2008, 7:25	2.9 ~ 6.1	280	1.3	117019

5.3 Chapter Summary

The dust aerosol detection with multi-sensor measurements, such as MODIS and CALIPSO, is performed in this chapter. Since both CALIPSO and Aqua MODIS operated

in the same A-train orbit with similar local passing time, the mis-registration of temporal is quite small and ignored in the algorithm. A simple approach is developed combining the CALIPSO VFM product and MODIS BTD (12, 11) measurements. With the CALIPSO VFM product, the aerosol and cloud layer are easily separated from ground scene types. Then dust aerosol is further separated from cloud with MODIS BTD (12, 11) values, since dust aerosol and cloud have opposite values. After spatial registration, those layers labeled as cloud in CALIPSO VFM but having positive BTD (12, 11) values are identified as heavy dust aerosol. Several cases are selected to test the algorithm; the accuracy is quite good by compare with true color images. Based on this approach, several dust storms occurred during spring season in northwest China is summarized. A few important parameters of dust aerosol are retrieved, including the altitude, thickness, location, and spatial coverage and distribution.

CHAPTER 6

VALIDATION OF SMOKE AND DUST AEROSOLS DETECTION

WITH MULTI-SENSOR

In Chapters three and four, the detection of smoke and dust aerosols is performed by combining MODIS RSB and TEB measurements based on the multi-spectra technique. The detection results are validated roughly with MODIS true color images. Visual validation provides, however, only basic verification. Validating results with the same sensor offers relatively low confidence. The further quantitative validation with other sensors, such as OMI and CALIPSO, is executed in this chapter.

6.1 Validation of Aerosol Detection with OMI

OMI onboard EOS AURA is one of key instruments designed for monitoring the ozone and other atmospheric species including aerosols. It is a hyperspectral sensor, observing the solar backscatter radiation in the ultraviolet (UV) and visible spectrum (Ahmad et al., 2003; Levelt et al., 2000). The wavelengths and algorithms used for retrieving OMI aerosol parameters are significantly different from those of MODIS. These differences produce some advantages, such as the high sensitivity of the OMI UV retrieval algorithm to aerosol absorption and the ability to retrieve aerosol information over bright surfaces and clouds (Livingston et al., 2007). Moreover, both AURA and

Aqua spacecrafts are operated in the A-train orbit. Therefore, OMI is selected for validating smoke and dust detection derived with MODIS measurements.

6.1.1 OMI sensor

OMI was launched successfully on July 15, 2004 onboard Aura. The Aura spacecraft is rotating in a 705 km sun-synchronous polar orbit (98.2^0 inclination angle) with a period of approximate 100 minutes. The local equatorial crossing time is 1:45 p.m. in the ascending mode. The OMI views the Earth with a wide view angle, $\pm57^0$ relative to nadir. The large swath, up to 2600 km in scan direction, enables OMI to achieve almost daily global coverage in 14 orbits. OMI instrument employs hyperspectral imaging in a push-broom, nadir-viewing mode to measure the solar backscatter radiation in the wavelength range from 270 to 500 nm, at a spectral resolution about 0.5 nm (Levelt et al., 2006). OMI instrument characteristics (Ahmad et al., 2003) are given in Table 6.1.

Table 6.1: OMI instrument characteristics

Item		Parameter
Wavelength range	Visible	365 - 500 nm
	UV-1	270 to 310 nm
	UV-2	310 to 365 nm
View angle		114^0 ($\pm57^0$)
Swath		2600 km
IFOV		3 km, binned to 13 x 24 km

6.1.2 OMI UVAI

The OMI instrument can distinguish between aerosol types, such as smoke, dust, and sulfates. The UVAI is an index to measure how much the wavelength depend on the backscattered UV radiation from an atmosphere containing aerosols (Mie scattering, Rayleigh scattering, and absorption) differs from that of a pure molecular atmosphere (pure Rayleigh scattering). It is a qualitative indicator of the presence of the absorbing aerosols, defined to be (Herman et al., 1997; Torres et al., 2007)

$$UVAI = -100 \log_{10} (I360_{Meas} / I360_{Calc})$$

where $I360_{Meas}$ is the measured 360 nm OMI radiance and $I360_{Calc}$ is the calculated 360 nm OMI radiance for a Rayleigh atmosphere.

Since the UVAI is sensitive only to absorbing aerosols, it is able to identify absorbing aerosols (dust, smoke) from weakly or non-absorbing particles. Usually, the aerosols that absorb in the UV yield the positive UVAI values. The near-zero UVAI values appear when the sky is clear or there are large non-absorbing aerosols and clouds which have nearly zero Angstrom coefficient. The non-absorbing small particle aerosols are the main source of negative UVAI values due to their non-zero Angstrom coefficients (Torres et al., 2007).

6.1.3 Validation of smoke detection with OMI UVAI

The OMI UVAI product is a valuable tool for the validation of smoke detection because the short wavelength band is sensitive to smoke. The OMI UVAI image of smoke plume from 2007 California Fire on October 23 at UTC time 21:40 is displayed in

the Fig. 6.1a. For easy comparison, the MODIS true color and smoke images of same region are plotted in Figs. 6.1b and 6.1c. The smoke originated from west coast of California and spread over the Pacific Ocean covering a large area, which satisfies the OMI relatively coarse spatial resolution.
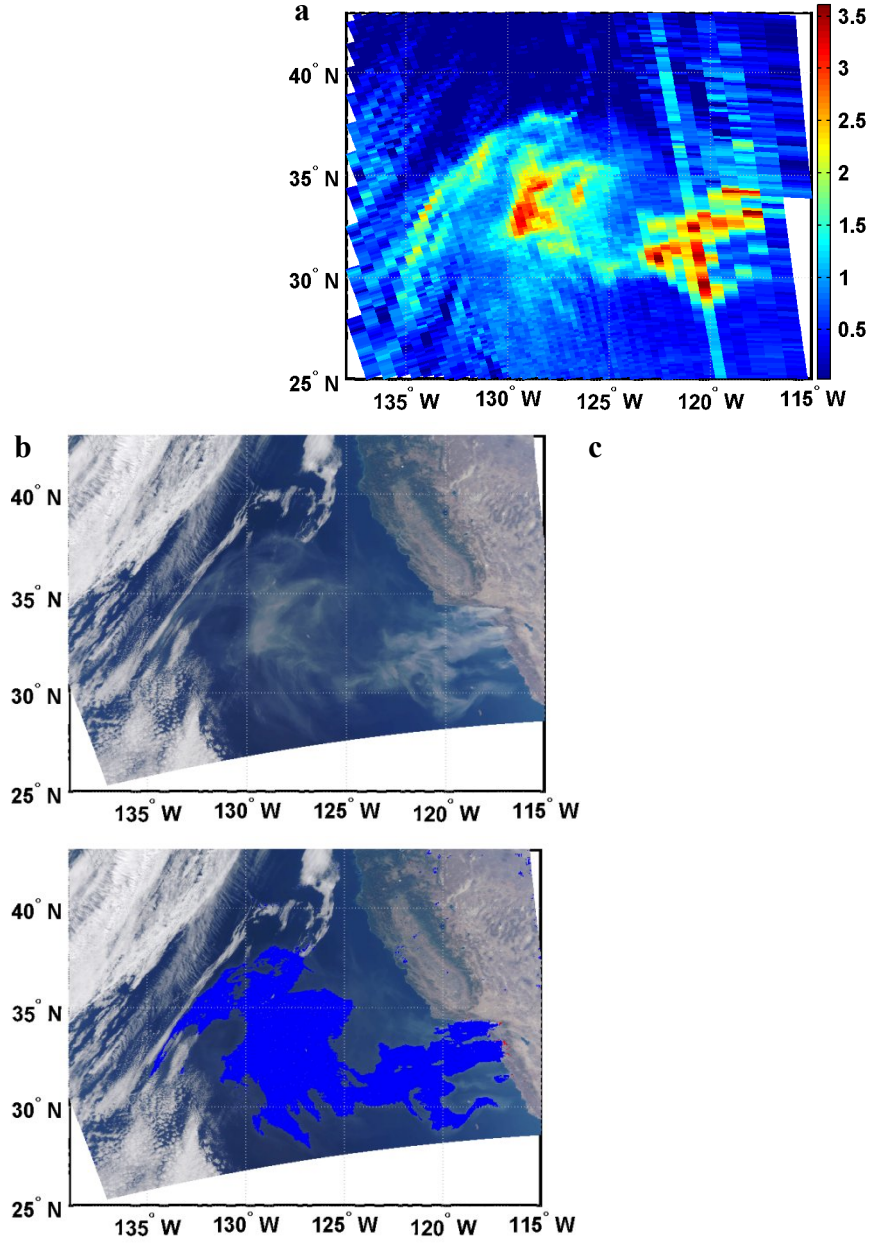
Figure 6.1: Validation of smoke image on October 23, 2007 with OMI UVAI. (a) OMI

UVAI image; (b) MODIS true color image; (c) Smoke image.

According to the procedure of aerosol selection presented in OMAERUN README file (http://daac.gsfc.nasa.gov/documents/OMAERUV_README_File_v3.doc), the aerosol associated with biomass burning usually has the UVAI values larger than 0.7. Therefore, the OMI UVAI images with the UVAI values larger than 0.7, 1.0, and 1.2 are displayed respectively in Fig. 6.2, for multiple comparisons with smoke image derived with multi-spectral algorithm using MODIS measurements. Some obviously misclassifications (bad or low quality data) in OMI UVAI product, are filtered out to improve the accuracy of comparisons.

The distributions of identified, unidentified, and misidentified pixels in three comparisons are given in Fig. 6.2. In the first comparison (UVAI > 0.7; Figs. 6.2a and 6.2b), there are 513,582 pixels are identified correctly (labeled as smoke in both images), listed in Table 6.2. About 365,853 pixels are unidentified (detected by OMI only) and 1,563 pixels are misidentified (detected by MODIS only) in MODIS smoke image. The percentage of identified smoke pixels increases to 73.78% with acceptable 4.34% misidentification in second comparison (UVAI > 1.0; Figs. 6.2c and 6.2d). In the third comparison (UVAI > 1.2; Figs. 6.2e and 6.2f), the unidentified smoke pixels decreases further to 11.18% but around 19.05% pixels are labeled as smoke in the smoke image which is labeled as nonsmoker pixel in OMI UVAI image.

Overall, the core part of smoke is explicitly detected by MODIS smoke image in all three comparisons. The major difference exists at the edge of plume, which may attribute to the different spatial resolutions between two sensors. Because of different spatial

81

resolutions, the number of smoke pixels in MODIS smoke image (1 km) is not enough to aggregate a corresponding pixel in OMI UVAI image (10 km). In another word, some smoke pixels in OMI UVAI image are not filled with smoke pixels in MODIS smoke image.
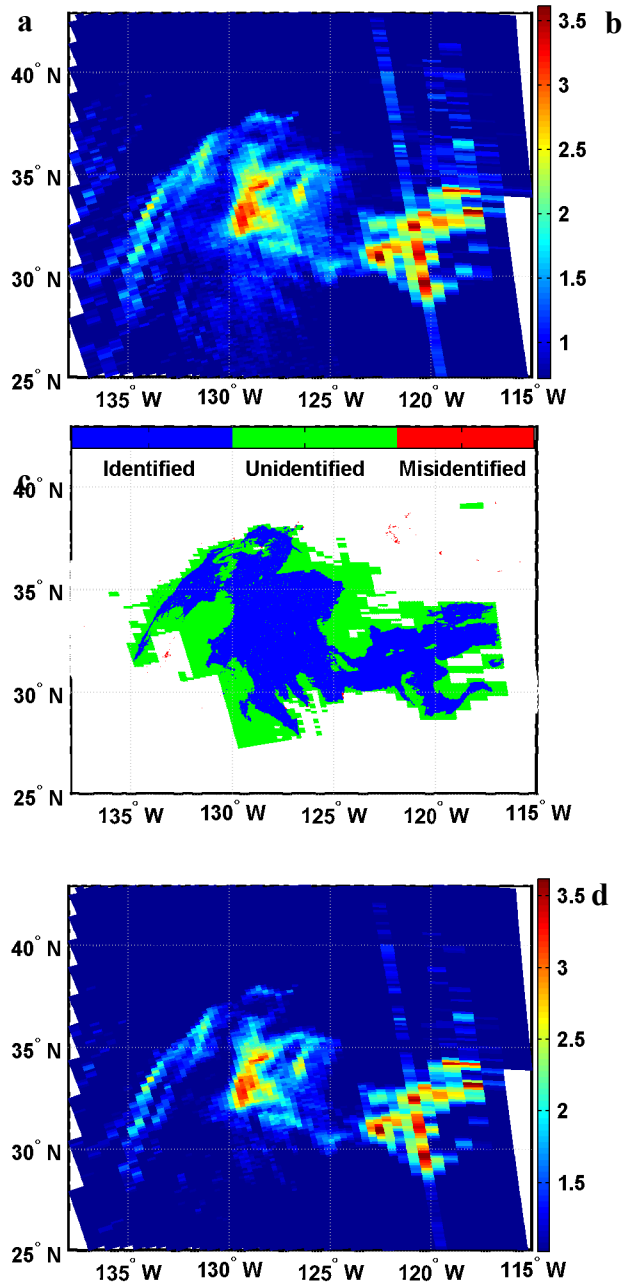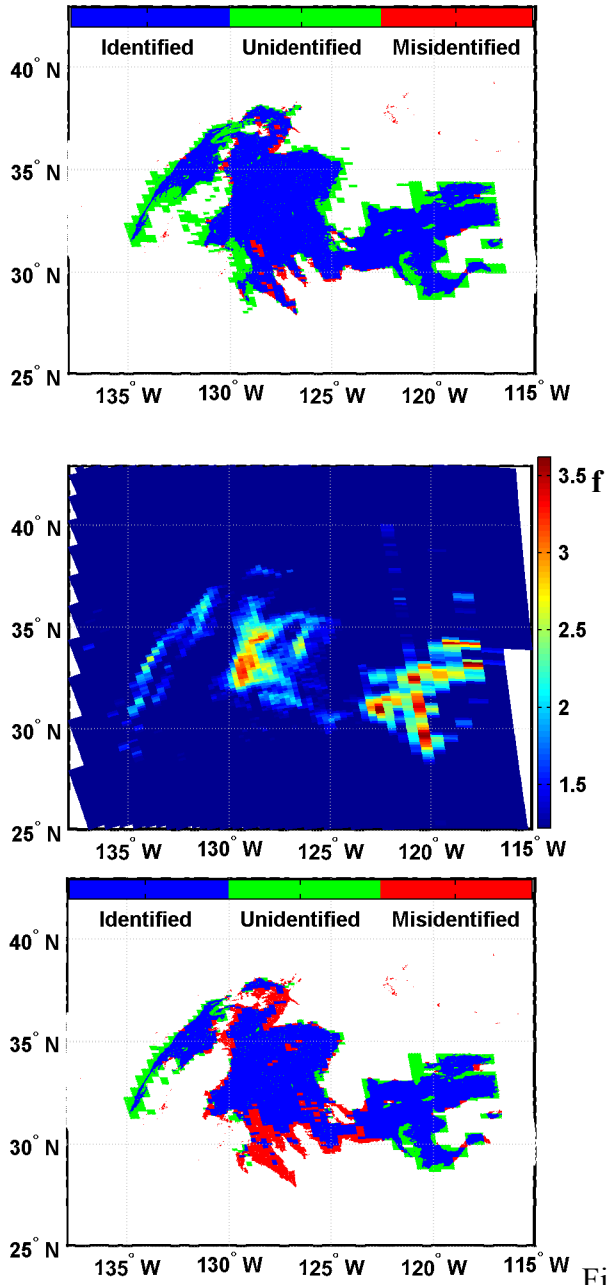
Figure 6.2: The UVAI images and the difference between UVAI and smoke images. (a) UVAI image (UVAI > 0.7); (b) The difference of first comparison; (c) UVAI image (UVAI > 1.0); (d) The difference of second comparison; (e) UVAI image (UVAI > 1.2); (f) The difference of third comparison.

6.1.4 Validation of dust monitoring with OMI UVAI

The dust storm in center China was captured by Aqua MODIS on October 23, 2007 at UTC time 04:55. The MODIS true color image is shown in Fig. 6.3a and corresponding dust image generated with algorithm illustrated in Chapter 4 is shown in Fig. 6.3b. The UVAI values associated with dust aerosol are usually larger than 1.2 according to the procedure of aerosol selection in OMAERUN README file. Therefore, only the areas with UVAI values larger than 1.2 in OMI UVAI image are shown in the Fig. 6.3c. With comparison, totally about 187,472 pixels are labeled as dust with OMI UVAI product. Among these pixels, 137,554 pixels are labeled as the dust either in MODIS dust image, but 49,918 pixels are undetected. About 3.67% (6,871 pixels) are identified as dust in MODIS dust image but labeled as non-dust pixel in OMI UVAI image. Fig. 6.3d gives the spatial distribution of all identified, unidentified, and misidentified pixels. The center part of the dust storm is detected by both images. The major difference is appeared at the front of dust storm (southeast part) where many pixels are labeled as dust aerosol in OMI UVAI image. Statistically, at the margin area, more than 5% difference can be attributed to the spatial resolution differences between two sensors. Moreover, the small clouds floated above the dust storm contribute another around 3% errors, which is too small to be detected by OMI sensor.
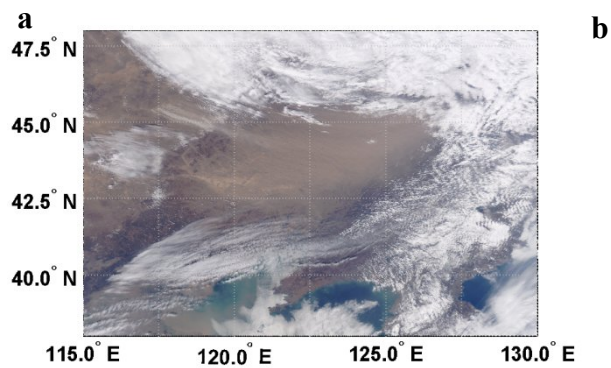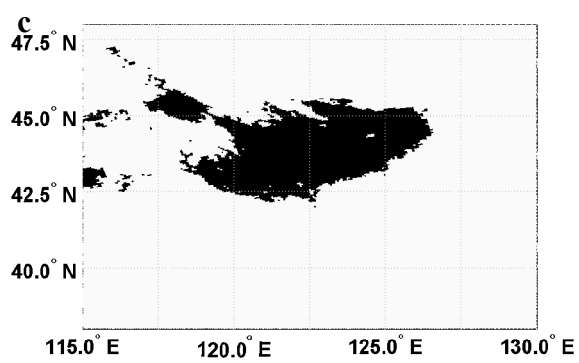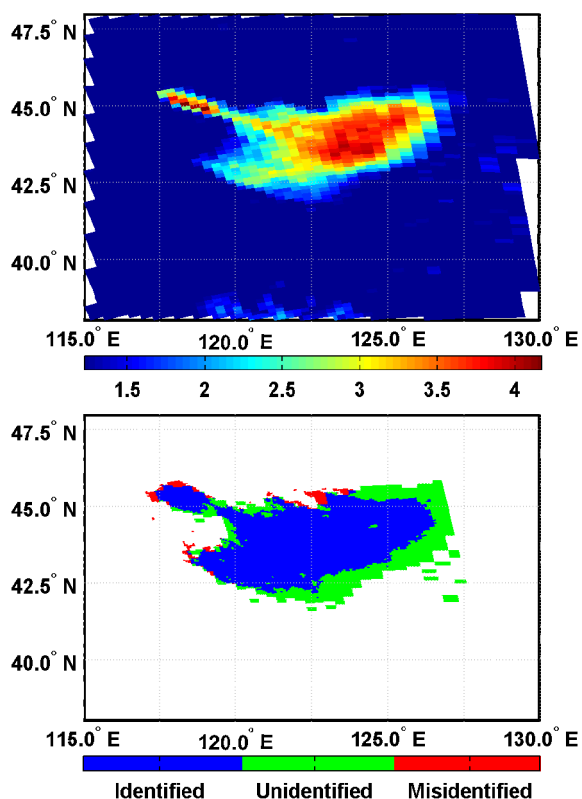
Figure 6.3 Validation of dust image with OMI UVAI on October 23, 2007 at UTC time 04:55. (a) RGB image; (b)Dust image; (c) OMI UVAI image; (d) The difference between UVAI and dust image.

Table 6.2 The error analysis in the comparisons between MODIS smoke image and OMI UVAI images with different UVAI values.

			MODIS smoke image	
			Non-smoke pixels	Smoke pixels
		UVAI > 0.7		1,563
OMI	Non-smoke	UVAI > 1.0		28,634
UVAI	pixels	UVAI > 1.2		110,502
image	Smoke	UVAI > 0.7	365,853	513,582
	pixels	UVAI > 1.0	144,287	486,511
		UVAI > 1.2	64,862	404,643

6.2 Validating Dust Detection with CALIPSO

The CALIPSO is an effective tool for validating the dust detection. It is capable of separating airborne dust from ground dust with the vertical information of aerosol and cloud layers. As illustrated in Chapter five, the CALIPSO VFM classifies various scene features into several types. Therefore, the VFM product is used for the quantitative validation of dust detection results.

Fig. 6.4 shows a dust storm event over Taklimakan Desert captured by Aqua MODIS on July 26, 2006. The image is generated with measurements extracted from two swaths at UTC time 7:25 and 7:30. The dust aerosol is located at the eastern desert. The blue dash line is the footprint of CALIPSO in this area. The dust image generated from multi-spectral approach is displayed in Fig. 6.5. The VFM product of the region marked by blue dash line in Fig. 6.4 is shown in Fig. 6.6. The validation is executed by matching pixels from two sensors with their geolocation measurements in the overlapping region. It is worth noting that the misclassification of labeling dust aerosol over desert area as cloud is observed which is mentioned in Chapter five. The dust aerosol layer marked in the black circle is misclassified as cloud in Fig. 6.6.

The error analysis is performed to count the number of pixels identified (pixel is labeled as dust aerosol with both sensors), unidentified (pixel is labeled as dust aerosol with only CALIPSO but undetected with MODIS), and misidentified (pixel is labeled as non-dust aerosol pixel with CALIPSO but detected with MODIS). According to spectral curves of dust aerosol in Figs. 4.2 and 4.3, red band is a key spectral band able to reflect the intensity of dust aerosol loading. Usually, the stronger the dust storm is the higher

reflectance in red band. Therefore, the dust aerosol pixels are sorted into several categories according to their reflectance at the red band, given in Fig. 6.7. There are 204 pixels identified and only 18 pixels unidentified. About 91.89% dust aerosol pixels obtained from proposed multi-spectral detection algorithm are correctly identified by comparing with CALIPSO VFM data product. Additionally, there are 21 pixels misidentified. Actually, the statistical analysis shows that most heavy dust aerosol pixels are identified. Unidentified and misidentified dust aerosol pixels are mostly concentrated in the low reflectance range at the red band, namely low dust aerosol loading. Fig. 6.8 displays the profile of dust storm in the sensor motion direction using the reflectance at the red band. In the image, the errors (unidentified or misidentified) are located only at the margin of the dust storm with light aerosol loading. Consequently, the multi-spectral algorithm for dust aerosol detection by MODIS works fairly well over bright surface, based on the validation with the CALIPSO VFM data product.
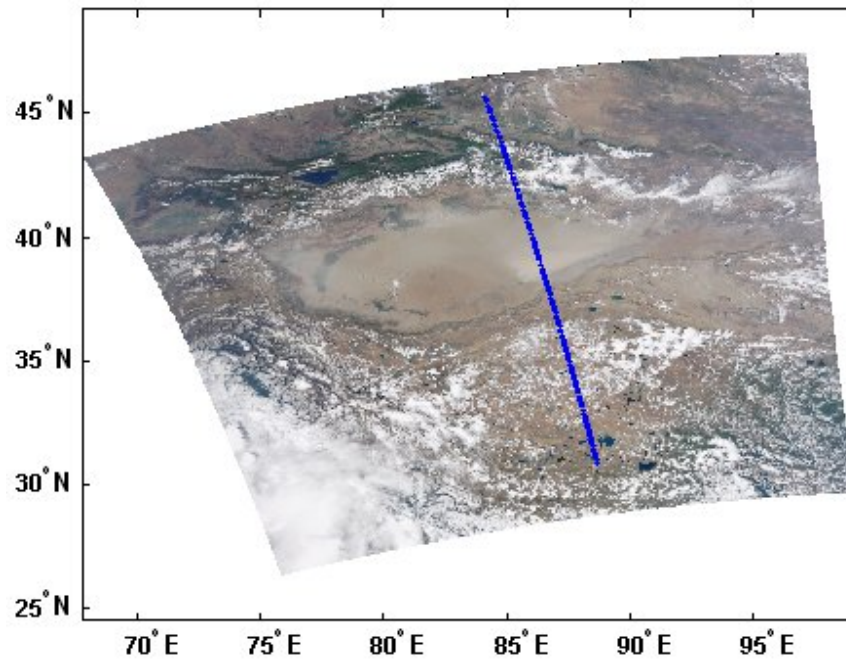
Figure 6.4: The MODIS true color image of dust storm over Taklimakan Desert on July 26, 2006. The blue solid line is the footprint of CALIPSO.
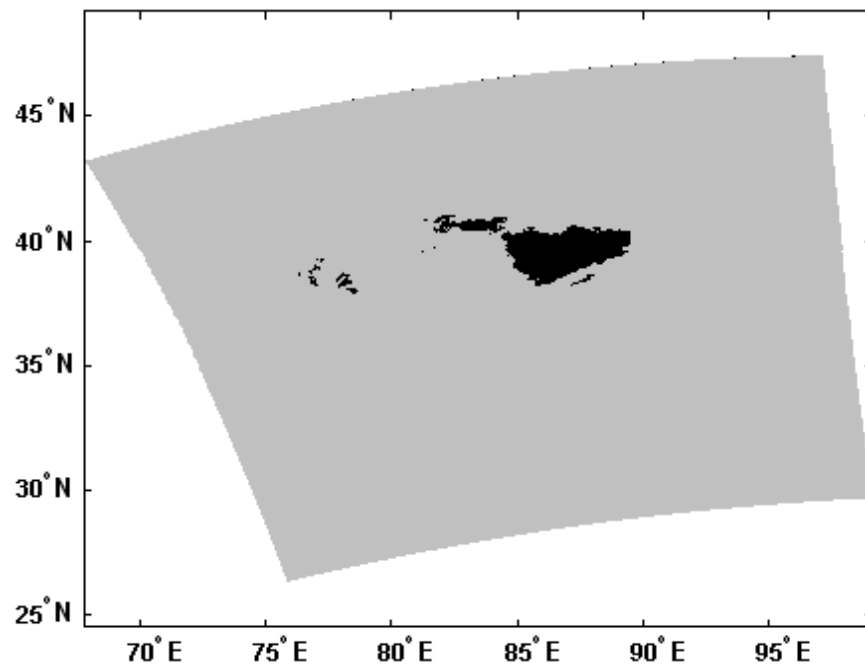
Figure 6.5: The Dust image of dust storm in Taklimakan Desert on July 26, 2006
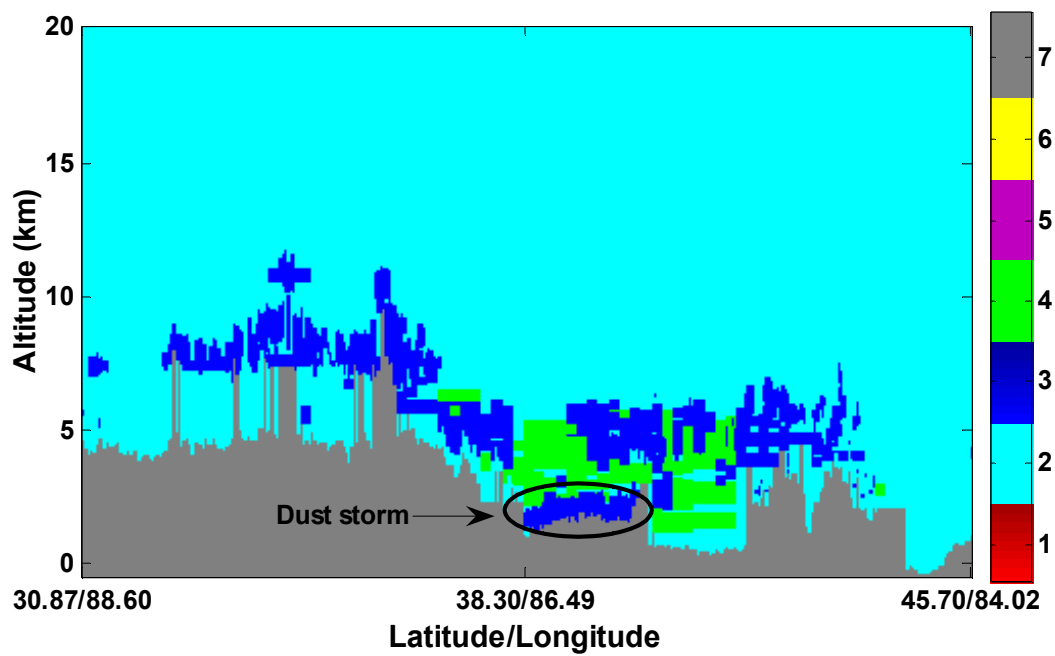
Figure 6.6: CALIPSO VFM data product on July 26, 2006 at UTC time 07:30.
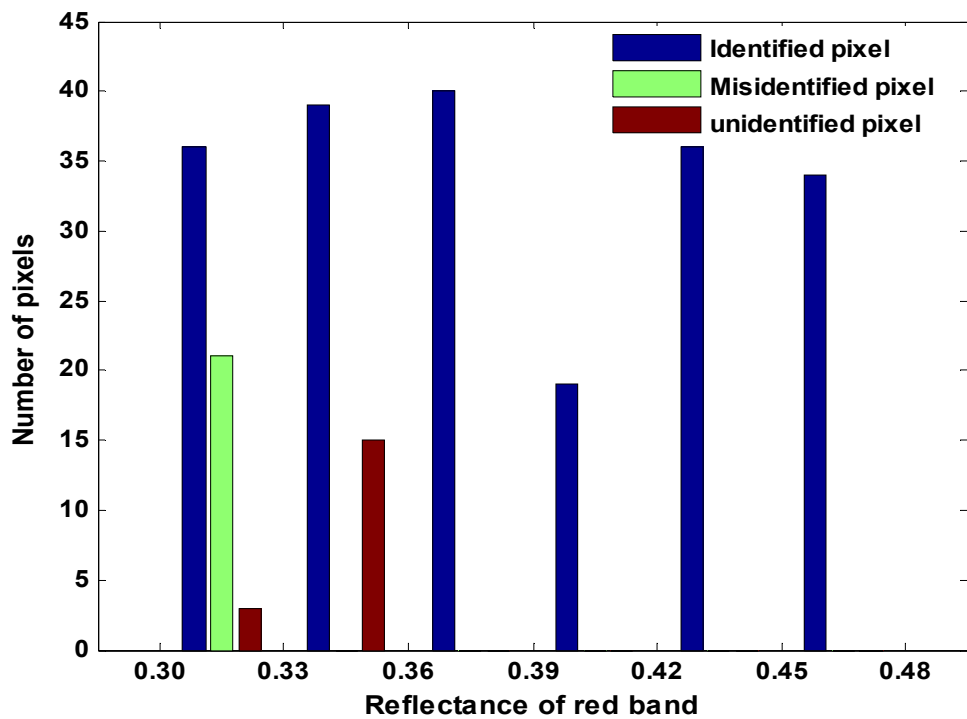
Figure 6.7: The error statistics of validating MODIS dust aerosol detection results with CALIPSO VFM data product

Reflectivity profile of dust storm at red band
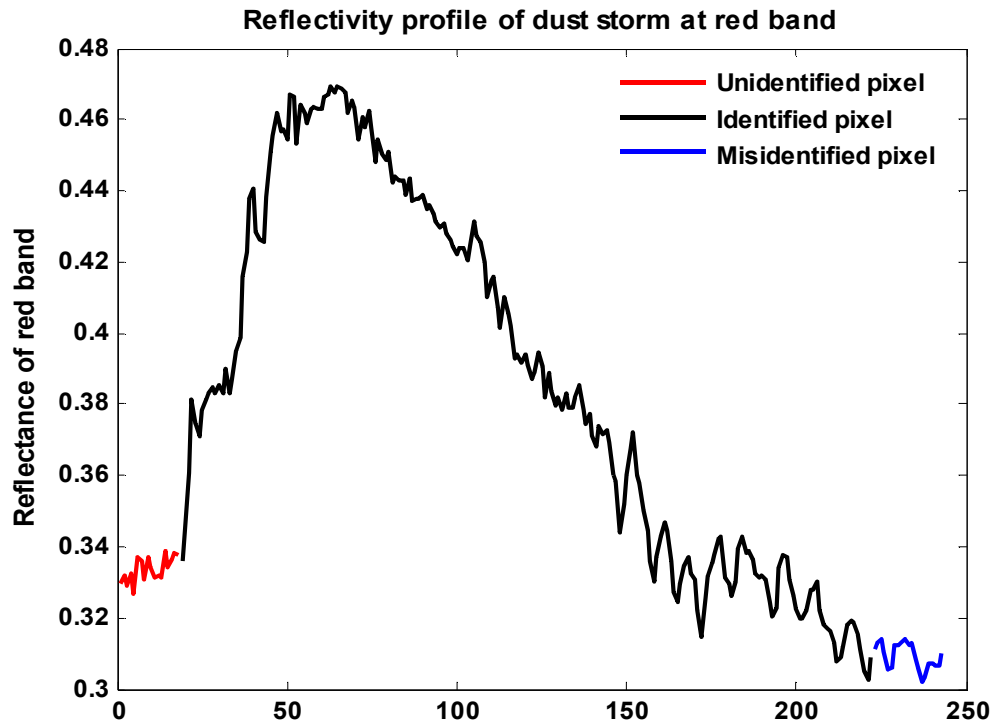
Figure 6.8: The profile of dust storm in the sensor motion direction

6.3 Undetected Smoke Plume

Although MODIS is a good sensor for detection of large scale smoke and dust aerosols, it is limited to detect small scale aerosol layer due to its moderate spatial resolution. The Aspen fire, located immediately northeast of Tucson, Arizona (32.4^0N, 110.7^0W), started on June 17, 2003. The fire burned over 84,000 acres and destroyed 333 structures. The fire was contained on July 12, 2003. The smoke plume was captured by both Hyperion and ASTER sensors on July 7, 2003, shown in Figs. 6.9a and 6.9b respectively. The Hyperion swath width is 7.6 km. The ASTER image covers an area of 41.2 x 47.3 km. However, it is difficult to find the smoke plume in MODIS true color

image at the same location. The reason of this undetected smoke plume may attribute probably to the moderate spatial resolution of MODIS instrument rather than algorithm itself.
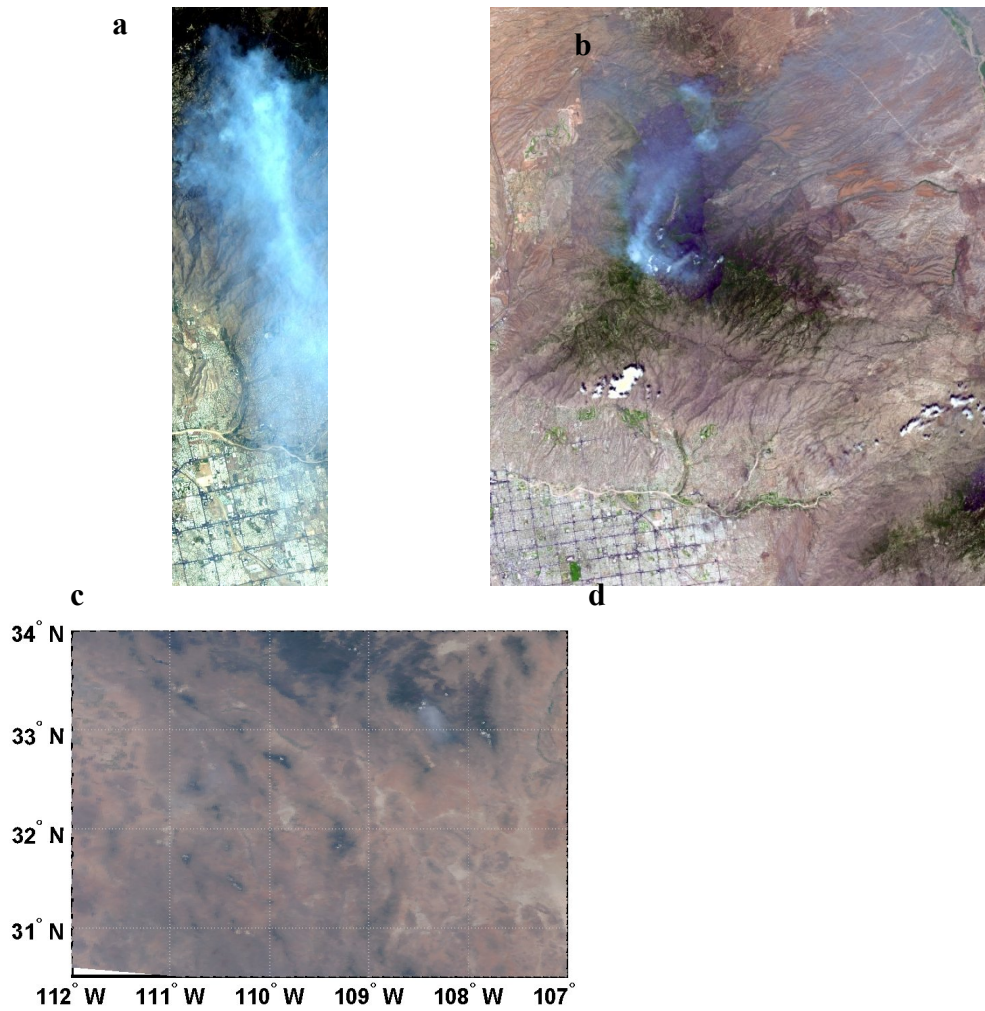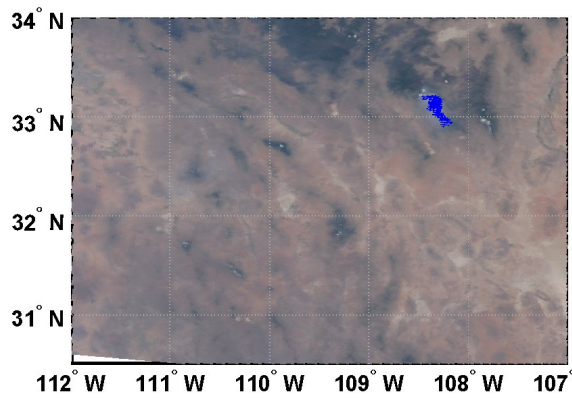
Figure 6.9: Smoke plume from Aspen fire observed by both ASTER and Hyperion on July 7, 2003. (a) Aspen fire captured by Hyperion sensor; (b) Aspen fire captured by ASTER sensor; (c) MODIS true color image at the same region; (d) Smoke image at the same region.

6.4 Chapter Summary

In this Chapter, the quantitative validation of smoke and dust detection using MODIS measurements is performed with OMI UVAI and CALIPSO VFM products. By comparing the smoke/dust images with OMI UVAI and CALIPSO VFM products, the number or the percentage of identified, unidentified, and misidentified smoke/dust pixels are counted.

The OMI UVAI, a qualitative indicator of the presence of the absorbing aerosols, is very sensitive to smoke/dust aerosols. According to statistical comparison results, more than 70% smoke/dust aerosol pixels are identified correctly. The spatial distribution difference images explicitly show that the core part of smoke/dust is detected. The

accuracy could be increased further if the uncertainties caused by the spatial resolution difference are subtracted.

Currently, the identification and validation of aerosols over bright surface is still a challenge issue. However, CALIPSO is a good sensor for detecting aerosols over bright surface, even for separating airborne dust from ground dust, with its vertical measuring capability. By comparing with the CALIPSO VFM data product, the dust aerosol detection works well over bright surface. More than 90% dust aerosol pixels are identified correctly in the select case. Although there are some pixels misclassified, most of them concentrate at the edge of dust storm with light dust aerosol loading. Those pixels with heavy dust aerosol loading are generally well detected.

Furthermore, the MODIS sensor is not very suitable for detecting small scale smoke according to the comparison with ASTER and Hyperion observations.

CHAPTER 7

IMPACT ASSESSMENT OF MODIS SPATIAL CHARACTERIZATION ON DETECTION RESULTS

The mis-registration, or the Band-to-Band Registration (BBR) shift, has been observed between the MODIS bands and FPAs by the Spectro-Radiometric Calibration Assembly (SRCA) and by the ground target approach. On-orbit results show that the

mis-registration for Terra MODIS is generally less than tenth of a pixel. But for Aqua MODIS, it is relatively large especially between the bands located on the warm FPAs and the cold FPAs. Because of the mis-registration, measurements over slightly mismatched areas from different spectral bands may produce undesired effects when used together, and consequently lead to less accurate data products (Xie et al., 2008). In this chapter, the impacts of the BBR shift on the L1B measurements and dust detection are assessed.

7.1 MODIS Sensor Spatial Calibration and Characterization

Before its launch, system level spatial characterization was performed with a ground calibration device called integration alignment calibrator by the instrument vendor (Barnes et al., 1998). Although MODIS Band-to-Band Registration (BBR) was carefully characterized pre-launch, mis-registration between the spectral bands and FPAs still exist or occur during its on-orbit operation. On-orbit, the MODIS has a unique device, the SRCA, operated bi-monthly or tri-monthly for monitoring and tracking the BBR change of all 35 bands relative to band 1. The quality of measurements is quite good. On the other hand, the ground target approach serves as an alternative means for observing the on-orbit BBR change with specific ground scenes located in Libyan Desert (Xie et al., 2006). The ground target approach provides frequent measurements for more than half of MODIS bands.

7.1.1 Mis-registration

Consistent with the pre-launch spatial characterization, relatively large spatial mis-registrations are observed for Aqua MODIS between its spectral bands on the warm

FPAs and cold FPAs (because of different temperature, VIS and NIR FPAsare called warm FPAs and SMIR and LWIR FPAs are named cold FPAs) (Xie et al., 2006). An example on Jan 4, 2003 at the UTC time 11:50 with 500 m spatial resolution measurements shows that the mis-registration exists between the warm and cold FPAs in both track and scan directions. Theoretically, the measurements of different spectral bands over the same target should match perfectly if there is no mis-registration. In the example (Fig. 7.1), a dark target located at the center of the selected area produces a lower signal than that of its neighboring pixels. In the along-track direction bands 1 and 4 on the warm FPAs scan the dark target at pixel number 11 while band 7 on the cold SMIR FPA crosses the same target at pixel number 10, about one pixel earlier (Fig. 7.1(a)). Likewise, in the scan direction, bands 1 and 4 scan the dark pixel at pixel number 10 while band 7 about one pixel later, at pixel number 11 (Fig. 7.1(b)). It indicates that the relative mis-registration is approximately one pixel, or 500 m, between cold and warm FPAs.
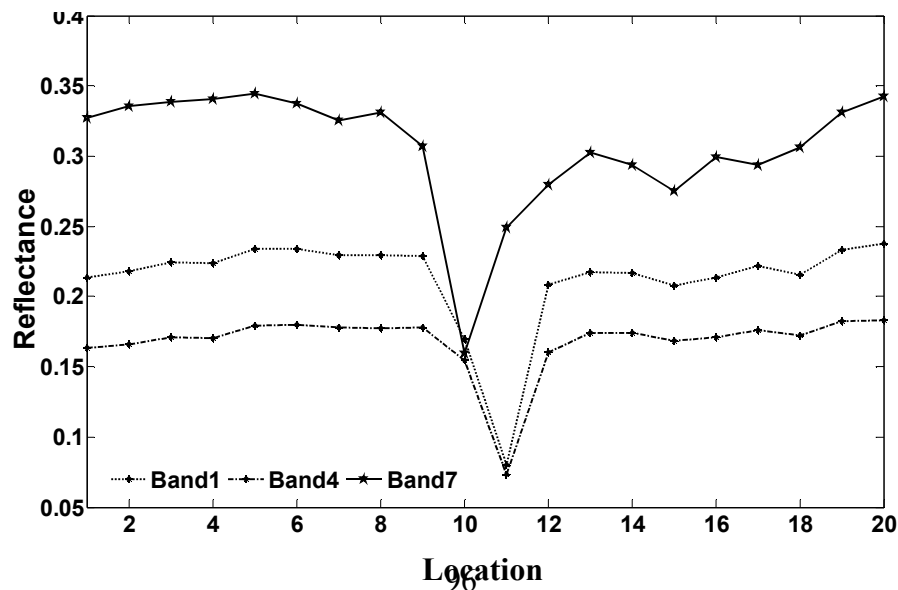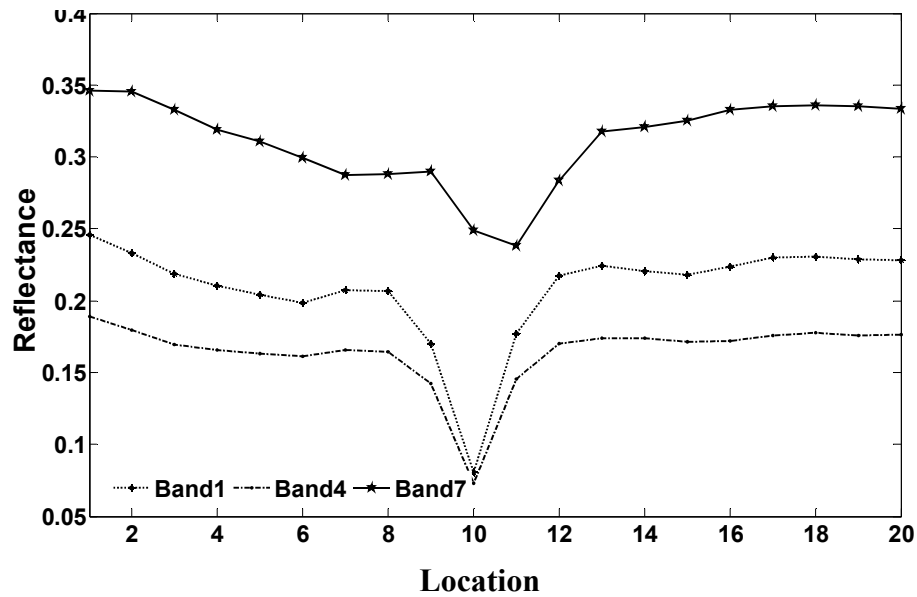
Figure 7.1: The example of mis-registration between MODIS VIS and SMIR FPAs. (a) Mis-registration between MODIS VIS and SMIR FPAs in track direction; (b) Mis-registration between MODIS VIS and SMIR FPAs in scan direction

7.1.2 Spatial characterization with SRCA

The Spectro-Radiometric Calibration Assembly (SRCA), a unique device within MODIS, is designed for sensor calibration and characterization in three modes: radiometric, spatial, and spectral. When it is configured in spatial mode, the SRCA is capable of tracking the BBR shifts periodically of all other 35 bands relative to band 1 from pre-launch to on-orbit and throughout the MODIS lifetime (Montgomery et al., 2000 and Xiong et al., 2005). To our best knowledge, tracking the spatial (also spectral) performance changes is unique because there was previously no device on remote sensing instruments to monitor these parameters over such a long period of time. This tracking provides valuable information to the remote sensing community and is beneficial for the

development of future remote sensing systems. Fig. 7.2 is a layout of the SRCA (Xiong et al., 2006). It consists of three subassemblies: a light source (VIS/NIR and infrared IR), a monochromator/optical relay, and a collimator. The VIS/NIR source is a spherical integration source (SIS) with four 10-W lamps and two 1-W lamps (one of the 10-W lamps and one of the 1-W lamps are backups) to provide multiple levels of illumination for the RSB characterization. A thermal source provides IR energy. The multi-lamp configurations allow each band to be operated at a good SNR level. When the SRCA is in spatial mode, a beam combiner on the filter wheel is used. The light coming out of the SIS passes through it while the IR beam is reflected from its surface. The combined beams provide illumination for all 36 bands. The light passes through the beam combiner and is focused onto the monochromator's entrance slit. After reflection by a collimating mirror, the beam passes onto a mirror or grating (the grating is used for the spectral characterizations). The beam is then refocused onto an exit slit (or various interchangeable reticles) by the focusing mirror. The follow-up Cassegrain telescope system expands and collimates the beam before it exits the SRCA and is viewed by the MODIS scan mirror. The SRCA spatial mode was originally performed bi-monthly. When the scan mirror is viewing the SRCA, the Earth scene illumination can pass through the MODIS system and interfere with the measurement. In order to minimize this effect, the SRCA is only operated in the night portion of the orbit.

When the SRCA is operated in spatial mode, an entrance slit equivalent to a 5 km (scan direction) 12 km (track direction) nadir Instantaneous Field Of View (IFOV) (Fig. 7.3a) is used (Xiong et al., 2005). The mirror is set up in position so that the

monochromator functions as a simple optical relay system. Located at the exit position are two reticles: one for along-scan, which is identical to the entrance slit (Fig. 7.3a), and the other for along-track (Fig. 7.3b) with stepped openings. The two reticles are positioned in turn to measure MODIS spatial response in both directions. The SRCA collimator and the MODIS optics image the reticles onto the FPAs. In the spatial mode, the IR source is on, and the lamps inside the SIS are turned on in sequence of three 10 W, two 10 W, one 10 W, and 1 W. Each band utilizes one light source configuration to assure an adequate SNR. Since the lamps need warm up time, both the along-scan and along-track measurements are performed at each lamp configuration before it is changed.
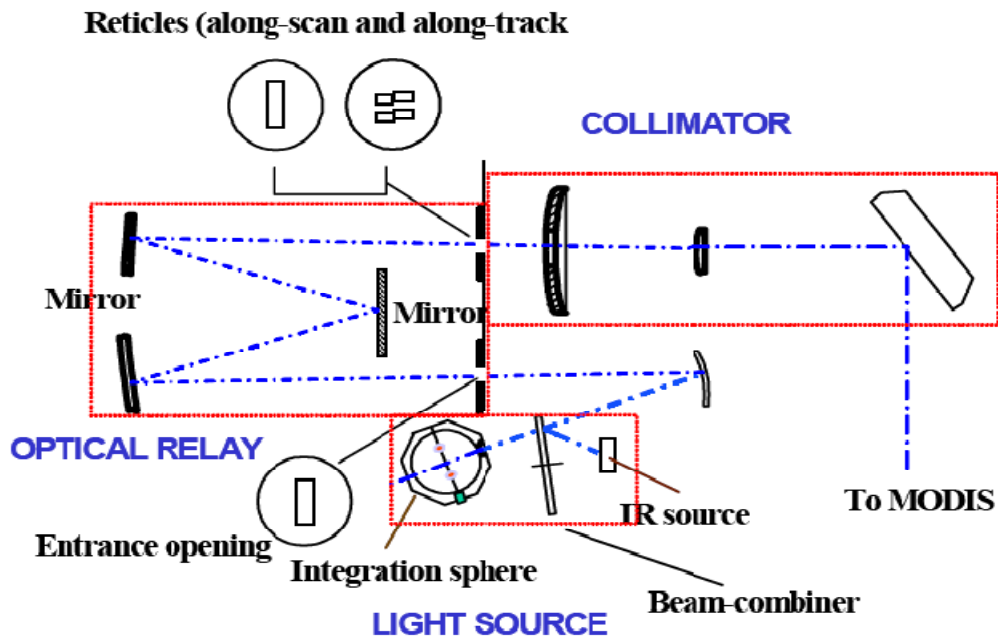
Figure 7.2: The layout of the SRCA (Source: Xiong et al., 2006).
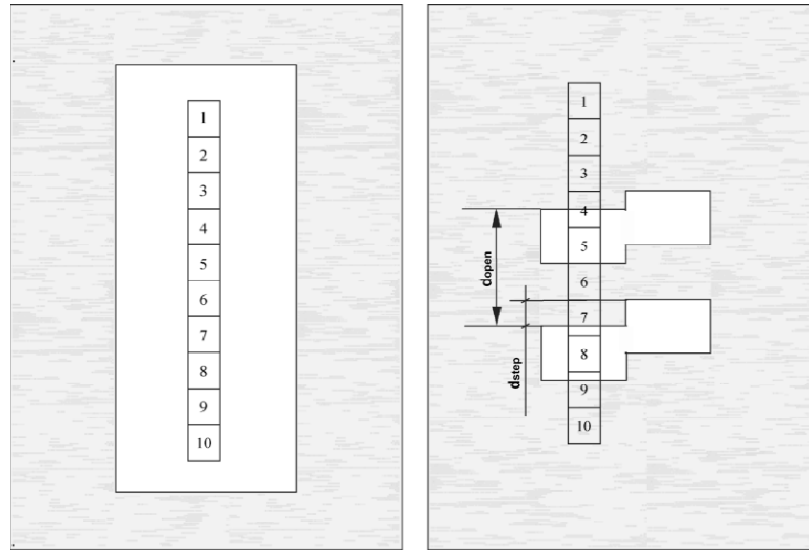
Figure 7.3: SRCA spatial mode reticles. (a) reticle along-scan; (b) reticle along-track (Source: Xiong et al., 2005).

7.1.3 MODIS spatial characterization using ground target approach

Not all sensors, however, have an onboard calibrator like the SRCA that provides instrument on-orbit spatial calibration and characterization. Using ground measurements over specific sites for sensor on-orbit spatial characterization is one of the alternative approaches (Xie et al., 2008). For example, two targets including burning areas in the agricultural fields at the Maricopa Agricultural Center, Arizona and the Lake Pontchartrain Causeway, Louisiana are applied for spatial characterization of the NASA EO-1 advanced land imager sensor by Schowengerdt et al. (2002). Moreover, he and his coworkers selected Mackinaw Straits Bridge in Michigan and the Chesapeake Bay Bridge at Annapolis, Maryland to measure spatial characterization for HYDICE (Schowengerdt et al, 1996). The same ground target, Pontchartrain Causeway, was applied to spatial characterization by the Landsat sensor (Storey, 2001). Nelson et al. (2001) used several ground scenes including edges from glaciers as well as several

bridges to determine the modulation transfer function for the Hyperion sensor. Nevertheless, these kinds of small ground targets are not appropriate for the MODIS spatial characterization in view of its moderate spatial resolution. Consequently, a desert area with a series of regularly arranged dark targets is chosen in this study for the MODIS on-orbit spatial characterization. Compared to the approach of using its on-board calibrator, this approach can provide more frequent characterization of the MODIS BBR as it requires no light sources. The deficiency is that it cannot provide spatial characterization for all bands, only for some RSBs (bands 1-11 and 17-19) and TEBs (bands 20, 22, 23, 29, 31, and 32).

7.1.3.1 Site for Spatial Characterization Using Ground Measurements

The ground targets selected for sensor spatial characterization must have high contrast features. Therefore, different types of ground targets could be used for measuring the BBR shift, such as a dark target, water body, coastline, snow coverage, and island. The site selected for the MODIS on-orbit spatial characterization is located at the Sahara desert in Libya, Africa. The latitude of this site is from 26.5^0 North to 28.0^0 North and the longitude is from 21.5^0 East to 22.5^0 East. Within this area, more than one hundred dark targets are arranged regularly in several rows. Each dark target has a circular shape with a diameter of approximately 1 km. The RGB image of this site from MODIS remote sensing measurements is shown in Fig. 7.4(a). The other three images, Figs. 7.4(b), (c), and (d), are taken from Google images with different spatial enlargements.

7.1.3.2 Date Source

MODIS L1B data at three spatial resolutions are used to calculate the spatial deviation: 250 m for band 2 (40 detectors / band), 500 m for band 3-7 (20 detectors / band), and 1 km for other bands (10 detectors / band). The L1B data used is the version 5 issued by NASA. Each MODIS L1B data set (referred to as a "granule") collects consecutive measurements within five minutes, typically 203 scans. In each scan, 1,354 data frames are recorded for each detector. For 500 m resolution band, 2 sub-frames or samples per frame (1 km) are recorded for its 20 detectors, and 4 sub-frames for each 250 m band and its 40 detectors (Xiong et al., 2003). Thus, each granule typically contains 2030 rows (along-track) × 1354 columns (along-scan) for 1 km resolution bands, 8120 rows × 5416 columns for 250 m resolution bands, and 4060 rows × 2708 columns for 500 m resolution bands.
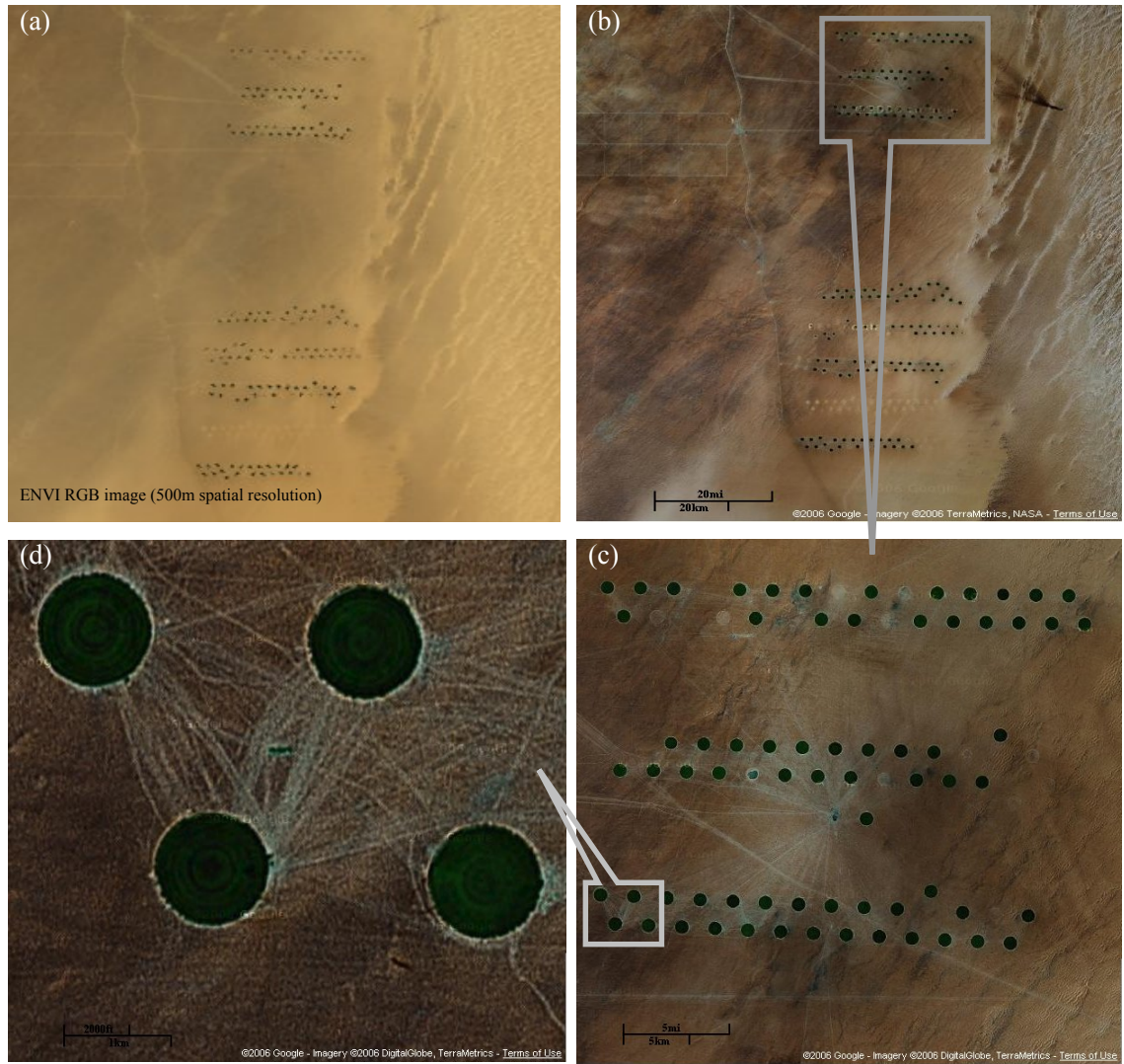
Figure 7.4: The color images of selected site for spatial characterization. (a) The MODIS RGB image (Latitude: 26.5^0N-28.0^0N, Longitude: 21.5^0E-22.5^0E) with 500 m resolution measurement; (b), (c), and (d) are Google images with difference enlargements for the same site (Courtesy of Google).

The consecutive measurements over the selected targets with high contrast features

can be used to track the BBR shifts for MODIS spectral bands during the entire mission.

Only daytime measurements are used in this spatial characterization study for both RSB

and TEB. Not all the measurements, however, are qualified for the sensor spatial

characterization. Only the measurements that satisfy two basic requirements are selected in this study for calculating the band-to-band spatial deviation. One requirement is that the measurements are from a clear scene free of clouds, dust storms, and snow in order to improve the accuracy. The other requirement is that the selected site must be located at the nadir area (sensor scan angle less than ±15 degrees) in the images. Otherwise there will be large distortion of the shape of circular dark targets due to the bowtie effect (Wolfe et al., 2002).

7.1.3.3 Algorithm

The same target will be mapped by each band at different positions in the MODIS images because of the mis-registration between bands. The location difference of the same target between two bands is equivalent to the spatial deviation. Therefore, the core process of this ground target approach is to find the discrepancy of centroid locations of the same dark target observed by different spectral bands. When the scan mirror scans across the selected dark targets, the response of each band will change rapidly and form a series of signal valleys. Only those valleys with high signal contrast are collected for the determination of the spatial shift in order to improve the accuracy of the algorithm. For a given valley, the centroid position difference between band a and b, ΔP_{ab}, can be computed using Eq. 7.1.

$$\Delta P_{ab} = \frac{\sum_{i=1}^{k} p_b(i) \cdot R_b(v_b, p_b(i))}{\sum_{i=1}^{k} R_b(v_b, p_b(i))} - \frac{\sum_{i=1}^{k} p_a(i) \cdot R_a(v_a, p_a(i))}{\sum_{i=1}^{k} R_a(v_a, p_a(i))}$$

(7.1)

where $p(i)$ is the position given in pixel number, $R(v,p(i))$ is the response at the position $p(i)$ for a given band and valley v, k is the total pixels of one valley used for calculation. The spatial shift, P_{ab} between band a and band b is the average of all the centroid location differences, ΔP_{ab}, within defined time range, expressed in Eq. 7.2.

$$P_{ab} = \frac{\sum_{N}\sum_{M} \Delta P_{ab}}{NM}$$

(7.2)

where M is the total number of the valleys in one qualified L1B measurement (one event or one pass) and N is the total events in defined time range such as one day, one month, or one year. The value of M varies from event to event due to the fixed threshold. Instead of using the number of pixels or the fraction of a pixel, the distance given in meters is adopted for expressing spatial shift, which is equivalent to the spatial shift multiple with spatial resolution.

7.1.3.4 Results

The average spatial deviations, from launch till the end of year 2007, for both reflective solar bands and thermal emissive bands relative to band 1 are calculated with qualified L1B measurements, and listed in the Table 7.1. However, not all bands can be used to retrieve spatial shift with this approach such as some ocean color bands, water vapor bands, cloud bands, and ozone bands. Most ocean color bands need the high scene contrast, or signal-to-noise ratio, so that they are normally in the saturation status. Some TEBs primarily focused on the properties of atmosphere, clouds, water vapor, and ozone may not have enough response to the ground targets. Consequently, only the BBR shift of

these bands, including reflective solar bands 1-11 (excluding Aqua band 6 due to a number of inoperable detectors) and 17-19 and thermal emissive bands 20, 22, 23, 29, 31, and 32 are listed in Table 7.1.

All the values represent the BBR shifts relative to band 1 in two directions. The positive spatial shift means that certain band observes the same Earth target earlier than band 1, while the negative sign indicates the reverse case. In the table, bands located in the same NIR FPA as band 1 have small spatial shifts. The spatial shift of the VIS FPA is also small except for bands 8-11 whose shifts are up to108 m in scan direction for Terra MODIS. For the cold FPA, the maximum spatial shift of Terra MODIS is 85 m along-scan and 122 m along-track while it is 277 m along-scan and 270 m along-track for Aqua MODIS. The standard deviation varies significantly with the spatial resolution of each band. The higher resolution bands have smaller standard deviation, consequently, higher accuracy of results. The results in Table 7.1 clearly show that the BBR shifts are much larger in Aqua MODIS for any band pair with one on the cold FPA and the other on the warm FPA. For example, the BBR shift between Aqua band 5 and band 4 in track direction is estimated to be 333m.

Table 7.1: The average spatial deviation for Terra and Aqua MODIS during sensor operation year (year 2000-2007 for Terra MODIS and year 2002-2007 for Aqua MODIS). All values are given in meters.

Band	Terra				Aqua			
	Track	std[1]	Scan	std	Track	std	Scan	std
2	6	8	-2	5	-5	5	3	4

3	6	11	-25	7	-59	10	-7	10
4	3	5	-18	3	-63	6	-24	6
5	38	18	9	10	270	31	-277	12
6	48	10	16	8	N.A.[2]	N.A.	N.A.	N.A.
7	53	12	16	9	251	29	-240	11
8	43	55	-108	55	29	52	84	61
9	41	40	-92	27	31	33	71	26
10	22	76	-78	74	1	78	58	77
11	-4	91	-53	124	-27	105	38	135
17	3	37	37	22	-13	27	-27	27
18	-4	54	3	24	-30	62	-32	37
19	-2	45	-4	18	-29	34	-40	27
20	21	76	-88	87	170	94	-208	110
22	-6	87	-122	93	136	122	-204	116
23	-26	90	-116	89	116	124	-159	114
29	38	118	-99	108	253	133	-78	133
31	-85	115	-94	136	146	135	-235	152
32	-67	111	-32	135	168	131	-198	127

1. std: stands for Standard Deviation
2. Not applicable for Aqua band 6 because of striping phenomena

7.2 Impact Assessment of MODIS Spatial Characterization

Based on the theoretical analysis, mis-registration or the BBR shift could impact the

quality of MODIS L1B measurements and dust detection results. If measurements of

different spectral bands are slightly mismatching, it will lead to undesired effects when they are combined together and consequently less accurate data products.

7.2.1 Impact on the L1B measurements

7.2.1.1 Uncertainty from SZA correction

Solar Zenith Angle (SZA) is the angle between the local zenith and the line of sight to the sun. As one of important parameters in MODIS Level 1A (L1A) geo-location measurement (MOD03 for Terra/MODIS and MYD03 for Aqua/MODIS), SZA is usually used for L1B response (radiance or reflectance) correction of RSBs. The SZA is the function of latitude and longitude, not identical in scan and track directions. Fig. 7.5 provides a case to describe the model of the SZA change, in which the first, middle, and last row/column are selected as representative for scan/track direction. In the Fig., the SZA changes non-linearly with the frame in scan direction because of bow-tie effect (Wolfe et al., 2002); rapidly at both ends while slowly in the middle frame. On the other hand, the SZA change shows a proximately linear model for all rows in track direction.

The correction is executed by dividing the cosine of SZA with original L1B measurement for corresponding pixel in one granule (Barbieri et al., 1997), given in Eq. (7.3)

$$R' = R / \cos(SZA') \tag{7.3}$$

where R and R' are the response of given RSB before and after correction respectively, and SZA' is the s corresponding SZA stored in MODIS L1A dataset. However, SZA' is a incorrect angle due to the mis-registration. The real response R'' should be computed

with Eq. (7.4) in which the symbol *SZA"* assumes to be the correct SZA,

$$R'' = R / \cos(SZA'') \tag{7.4}$$

Therefore, the relative error between two responses *R'* and *R"* could be calculated with Eq. (7.5).

$$\frac{R'' - R'}{R'} = \frac{R''}{R'} - 1 = \frac{\cos(SZA')}{\cos(SZA'')} - 1 = \frac{\cos(SZA')}{\cos(SZA' + \Delta SZA)} - 1 \tag{7.5}$$

where *ΔSZA* is the difference between two solar zenith angles *SZA"* and *SZA'*.

The theoretical impact of mis-registration on L1B measurement for both directions is plotted in Fig. 7.6, with one, two, or three -pixel BBR shift. In scan direction, the impact changes rapidly at both ends but slowly in the middle. Since the change of SZA is quasi-linear in track direction, the impact of BBR shift along-track on L1B measurement has almost the same quasi-linear trend.

The SZA in one granule is different with geo-location and seasons, the largest relative error could be estimated with the curves in Fig. 7.7 by defining the largest SZA of one granule and corresponding BBR shift. The curves computed with Eq. (7.5) by setting *ΔSZA* as 0.01^{o}, 0.03^{o}, 0.05^{o}, or 0.1^{o} show that the relative error increases with the positive *ΔSZA* and decreases with negative *ΔSZA*. The curve changes slowly at the small SZA range while rapidly at the large SZA range. The relative error could reach to 0.5%, if there is 0.1^{o} *ΔSZA,* when SZA is about 65°.
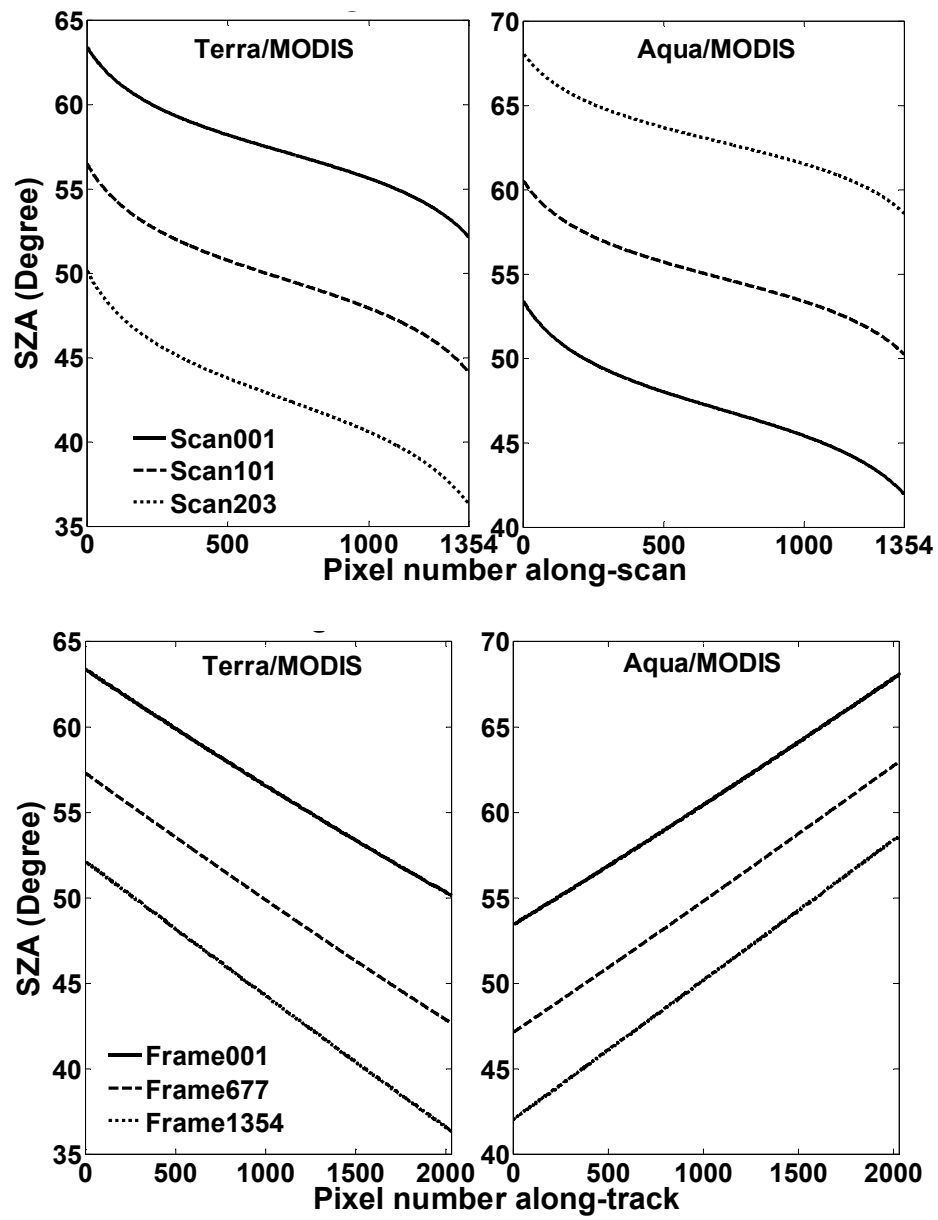
Figure 7.5: TOP: the change of SZA with frame in scan direction; Bottom: the change of SZA with sub-scan in track direction

110
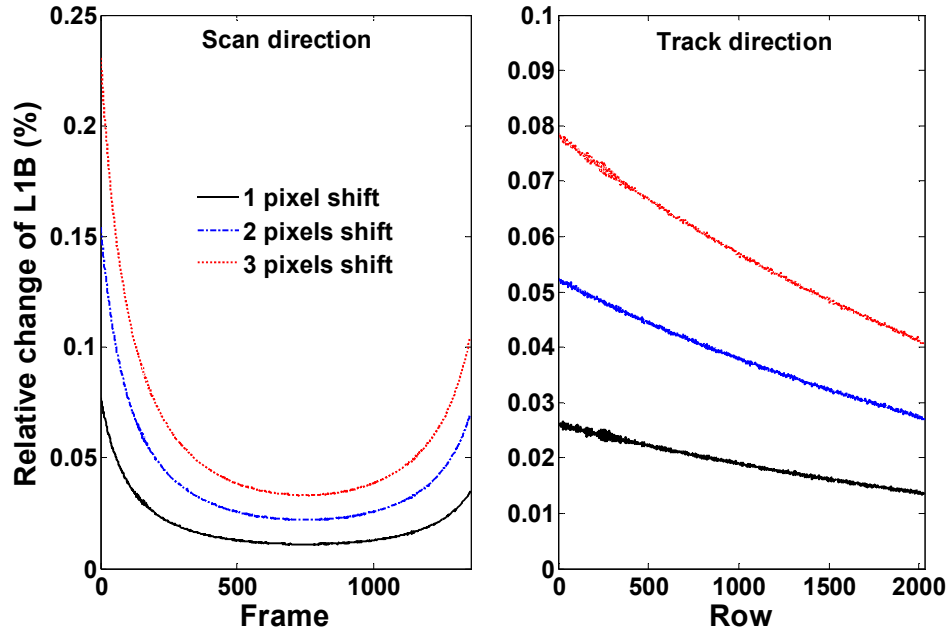
Figure. 7.6: The relative change of L1B measurements with different BBR shift (1, 2, and 3 pixels).
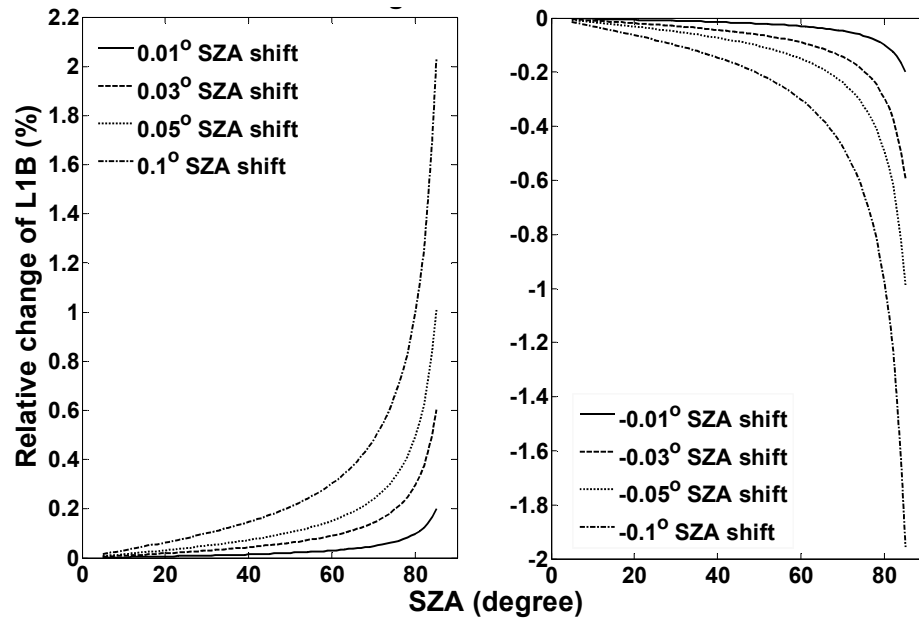
Figure. 7.7: The relative change of L1B measurement in the percentage with various SZA shift (left image: positive SZA shift; right image: negative SZA shift)

7.2.1.2 Real Impact on L1B Measurement

The SZA science dataset in the L1A file usually has a 1 km spatial resolution. The interpolation is necessary because on-orbit BBR shifts of all bands are less than one pixel in both MODIS instruments. The simplest method, linear interpolation, is adopted. The relative errors of L1B dataset caused by using uncorrected SZA for all Aqua MODIS RSBs except band 1 are listed in Table 7.2, where the largest SZA is up to 68^0. The third and fourth columns provide the relative errors in scan or track direction individually, and the last column presents the relative errors by combining errors in two directions together. Since the relative error is proportional to the spatial BBR shift, those SMIR bands which have larger BBR shifts also have larger relative errors. The relative errors of Terra MODIS bands are less than those of Aqua MODIS bands due to their smaller BBR shifts. The largest relative error of L1B dataset is less than 0.1%. The error is small enough to be ignored, so far, in real applications for both MODIS instruments.

7.2.2 Impact analysis of mis-registration on science data products

The MODIS is of great importance in science research field, widely used for applications in atmosphere, land, ocean, biosphere, and solid earth (Justice et al., 1998; Esaias et al, 1998; King ea al., 2003; Parkinson et al., 2003). A series of data products have been developed so far for various applications including a bunch of normalized indices and products generated with the linear or non-linear combination of responses from several spectral bands. The spatial mis-registration between different bands or FPAs impacts obviously the precision of science data products when several bands combined

together in the algorithm, especially at the boundary of mixed scene types where the response may change rapidly so that the mismatching response will be used in the algorithm (Xie et al, 2007; Wang et al., 2007).

Table 7.2: The largest impact of all Aqua RSBs based on the on-orbit results from the SRCA with the largest SZA up to 68^0.

Band	FPA	Scan (%)	Track (%)	Scan/Track (%)
2	NIR	1.5×10^{-3}	6.0×10^{-4}	2.0×10^{-3}
3	VIS	5.8×10^{-3}	3.0×10^{-4}	7.4×10^{-3}
4	VIS	8.4×10^{-3}	3.0×10^{-4}	7.2×10^{-3}
5	SMIR	7.3×10^{-2}	9.8×10^{-2}	8.6×10^{-2}
6	SMIR	8.0×10^{-2}	9.7×10^{-2}	8.9×10^{-2}
7	SMIR	6.3×10^{-2}	9.4×10^{-2}	7.8×10^{-2}
8	VIS	2.4×10^{-3}	5.1×10^{-3}	5.6×10^{-3}
9	VIS	4.0×10^{-4}	7.9×10^{-3}	7.2×10^{-3}
10	VIS	2.2×10^{-3}	1.5×10^{-2}	1.4×10^{-2}
11	VIS	1.0×10^{-2}	1.5×10^{-2}	1.9×10^{-2}
12	VIS	1.3×10^{-2}	2.0×10^{-2}	2.4×10^{-2}
13	NIR	2.2×10^{-3}	3.9×10^{-3}	4.5×10^{-3}
14	NIR	1.5×10^{-3}	1.2×10^{-3}	2.1×10^{-3}
15	NIR	1.9×10^{-3}	1.8×10^{-3}	3.0×10^{-3}
16	NIR	4.5×10^{-3}	3.9×10^{-3}	6.8×10^{-3}
17	NIR	2.6×10^{-3}	6.0×10^{-4}	3.3×10^{-3}
18	NIR	4.1×10^{-3}	2.7×10^{-3}	5.8×10^{-3}
19	NIR	3.2×10^{-3}	8.2×10^{-3}	8.5×10^{-3}
26	SMIR	6.6×10^{-2}	8.2×10^{-2}	7.5×10^{-2}

7.2.2.1 Theoretical impact analysis of science data products by mis-registration

The normalized indices (*NI*) are the normalization of two or more spectral bands. They are usually used for the scene identification with general formula shown in Eq. (7.6), where R_a and R_b are responses of bands *a* and *b* respectively. Commonly, one band in *NI* is sensitive to a given matter class and the other band is insensitive to it, such as Normalized Difference Vegetation Index (NDVI) (Rouse et al., 1973; Huete et al., 1994), Normalized Difference Snow Index (NDSI) (Hall et al., 2002), Normalized Difference Water Index (NDWI) (Gao, 1996), and Normalized Difference Dust Index (NDDI) (Qu et al., 2006). In some indices, R_a or R_b can be the response combination of several spectral bands, such as Normalized Multi-band Drought Index (NMDI) (Wang et al., 2007).

$$NI = \frac{R_a - R_b}{R_a + R_b} \qquad (7.6)$$

If there is a small response deviation of two bands, ΔR_a and ΔR_b, the change of *NI* value, *ΔNI*, is approximately equal to the first order partial derivative with respect to two variables, R_a and R_b. Practically, one of bands is designated as reference band in most cases to simplify the calculation by setting ΔR_a=0 (or ΔR_b=0). The *ΔNI* can be computed with Eq. (7.7)

$$\Delta NI \approx \frac{-2R_a}{(R_a + R_b)^2} \Delta R_b{'} \qquad (7.7)$$

where *ΔRb'* is the minute response change of band *b* caused by its spatial mis-registration relative to band *a*.

Fig. 7.8 shows that the *NI* value varies with the reflectance of two bands at a given reflectance change of band *b*. The x and y axes represent the reflectances of bands *a* and *b*, and z axis (vertical axis) stands for the variation of index value. The change of *NI* value decreases with the increasing difference between R_a and R_b. The maximum variation of *NI* value is up to 0.0527 if R_b has a negative ten percent response shift. The *NI* value change could reach to 0.1779 if there is a negative 30% response shift of R_b.
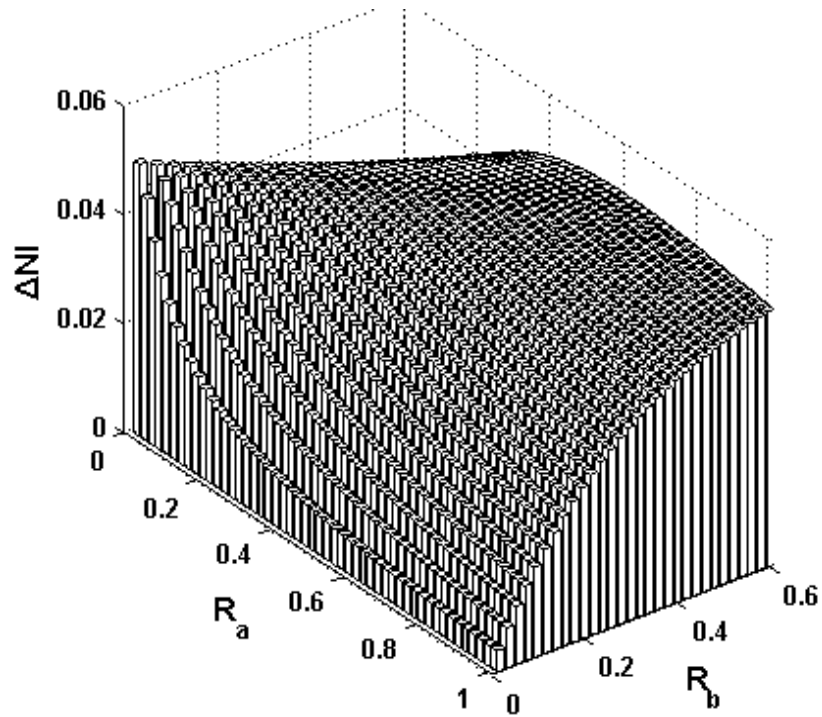

Figure 7.8: *NI* change with negative 10% response change of band *b*

7.2.2.2 Impact on detection of dust aerosol

The NDDI is an index proposed for the identification of dust aerosol. It is the normalized ratio of band 3 and band 7, in which the former band is located on the warm FPA and the latter one is located on the cold FPA. With the results of the SRCA on-orbit

spatial characterization, the biggest mis-registration is observed between the warm FPA and the cold FPA. The existence of spatial shift between these two bands, up to 320 m along-track and 265 m along scan, will produce undesired effects, and consequently, lead to less accurate NDDI value and dust aerosol detection product.

If the NDDI is calculated with 500 m resolution measurements, the mis-registration between two bands is up to 0.64 pixels in track direction and 0.53 pixels in scan direction. The tentative correction is performed by shifting one pixel in track direction while keep unchanged in scan direction since the mis-registration is more serious along-track. A dust storm is displayed in Fig. 7.9 (only part of dust storm) by MODIS true color image. The dust storm is prevalent in the left and right sides of the image, divided by the cloud in the middle. Fig. 7.10 and Fig. 7.11 present the difference of NDDI values and dust aerosol detection. The three subplots in Figs. 7.10 and 7.11, from left to right, are the results with and without correction and their comparison difference.

In Fig. 7.11, the total number of dust aerosol pixels detected is 15,622 in the sampled area, listed in Table 7.3. After correction, the number of detected dust aerosol pixels decrease to 15,455. There are 15,270 pixels are labeled as dust aerosol in two results, equaling 97.747%. About 185 non-dust aerosol pixels (cloud and other pixels) are labeled as dust aerosol pixels after correction, and correspondingly 352 dust aerosol pixels are identified as non-dust pixels in the corrected results. The difference is up to 3%. The correlation coefficients, r^2, of all three surface scenes increase after spatial correction. This increase demonstrates that the quality of science data products can be improved by spatial correction.

116

It is worth mentioning that the difference (or uncertainty) varies with the coverage of selected area. The differences are relative small at the homogenous or semi-homogenous area, and large at the non-homogenous areas. Based on this analysis, it is reasonable to conclude that the impacts on most of science products caused by spatial mis-registration are concentrated in the non-homogenous areas or mixed areas.

Table 7.3: The difference between dust aerosol detection results with and without spatial correction

	No correction			With correction		
	Dust	Cloud	Others	Dust	Cloud	Others
Classification	15,622	10,697	3,681	15,455	10,721	3,824
r^2	0.9825	0.5636	0.9700	0.9831	0.5811	0.9706

		With correction		
		Dust	Cloud	Other
NO correction	Dust	15,270	0	352
	Cloud	0	10,475	222
	Other	185	246	3,250
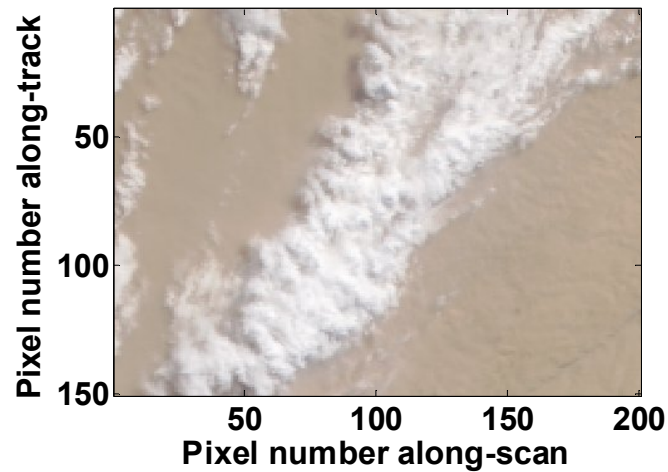
Figure 7.9: The MODIS true color image of selected case with dust plume.
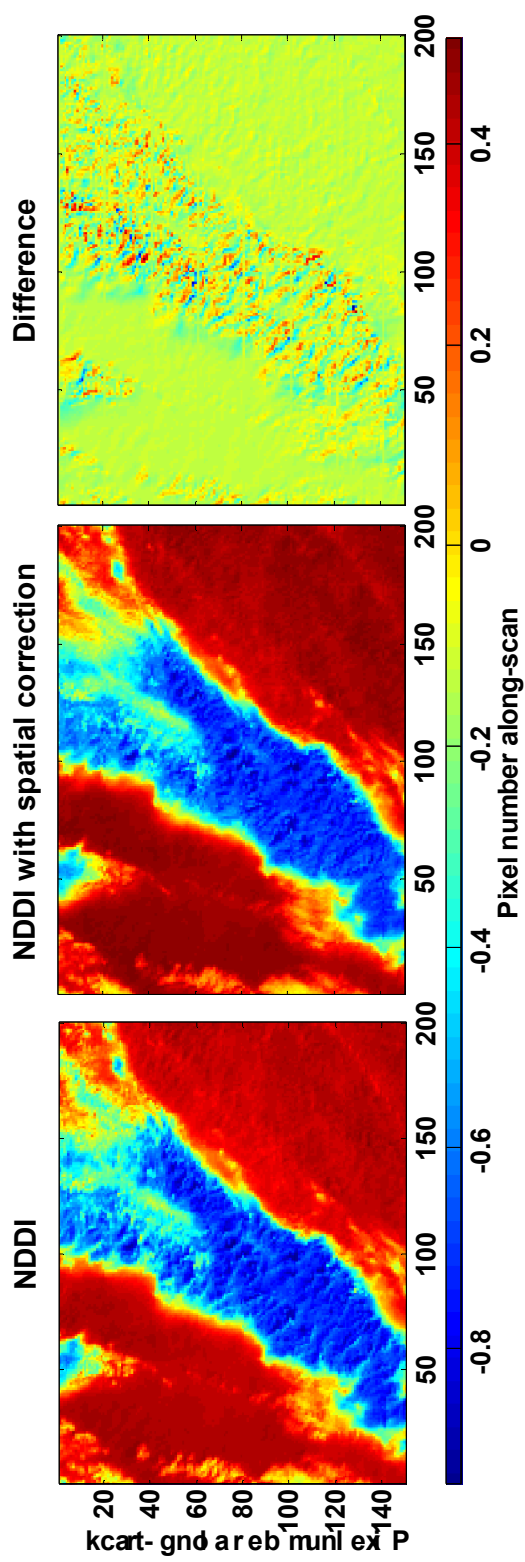
Figure 7.10: NDDI value with and without correction, and their difference.
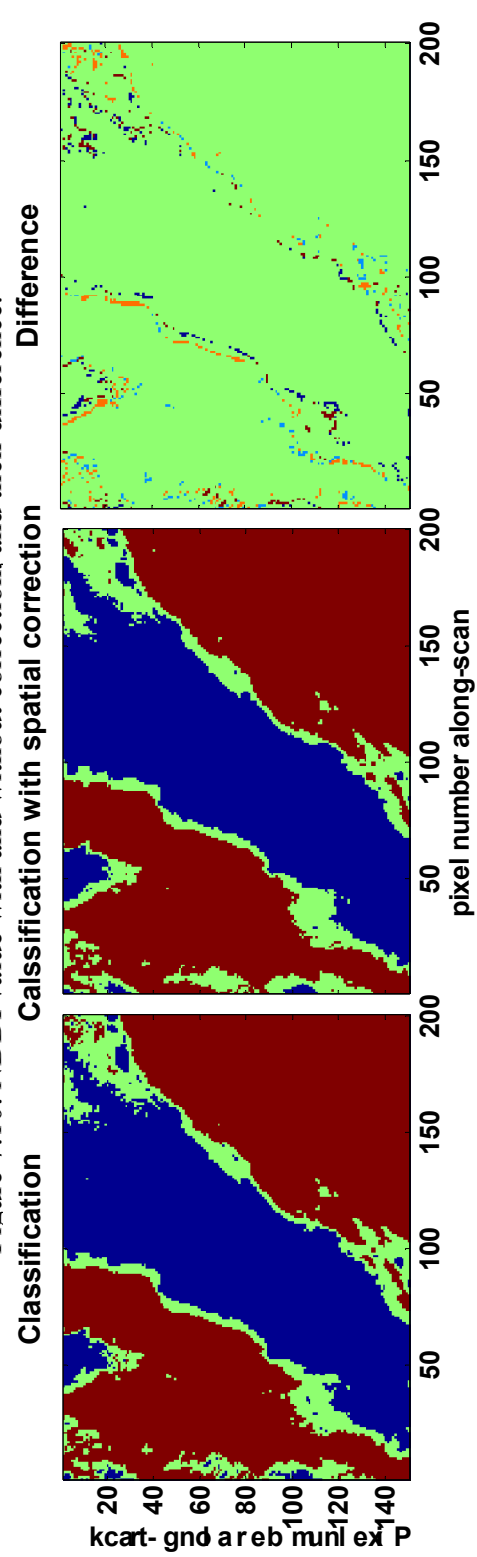
Figure 7.11: Dust detection product with and without correction, and their difference.

118

7.3 Chapter Summary

The mis-registration, or the BBR shift, has been observed between the bands and FPAs by the ground target approach and by the Spectro-Radiometric Calibration Assembly (SRCA). The impact analysis of MODIS BBR shift on MODIS L1B data and science data products is performed based on the SRCA on-orbit spatial characterization results. The quality of L1B data could be lessened by executing the SZA correction using mismatch SZA due to mis-registration. The impacts are different between two directions due to the strong bow-tie effect in scan direction. The practically largest relative errors of all RSBs for Aqua MODIS are less than 0.1% in the select case, which are negligible in actual applications. The spatial correction of L1B data is necessary if the BBR shift is too large to reduce the data quality significantly.

The theoretical analysis shows that the influence of mis-registration on science data products is generally larger than that on L1B data. The NDDI, an index for dust aerosol identification, is selected to estimate the impact of mis-registration on science data product since. The influence on dust aerosol detection results is small at the homogenous or semi-homogenous areas but relative large at the mixed areas. The increase of correlation coefficient demonstrates that the quality of science data product can be improved by shifting a pixel in track direction.

This study provides valuable information for sensors without spatial characterization capability and also for the specification design of future sensors.

CHAPTER 8

CONCLUSIONS AND DISSCUSIONS

8.1 Conclusions

In this dissertation, the multi-spectral algorithm for observing and monitoring smoke and dust aerosols over both bright and dark surfaces is developed by combining measurements of MODIS solar and thermal bands. Since the algorithm uses its own cloud module to separate the cloud, the algorithm can detect the smoke/dust at the areas close to or mixed with clouds. In the algorithm, the spectral curves of several major scene types in both solar and thermal spectrum, such as smoke, dust, cloud, and vegetated surface and non-vegetated surface, are derived statistically from large quantity of training data. According to spectral analysis, the algorithm is divided into land and ocean branches for smoke detection, and into bright surface and dark surface branches for dust detection. In the algorithm, the thermal bands are mainly used for filter out cloud, as well as a water vapor band, while the RSBs are selected for separating smoke/dust from other scene types. Some indices well developed in others previous studies are adopted directly. And some tests are proposed first time, including the pseudo-NDVI, the reflectance of blue band, and the normalized of two blue bands used for smoke detection; and the reflectance of red band used for dust detection. The spatial resolution of smoke/dust detection results

is up to 1 km. By comparing with MODIS true color image, the core part of smoke/dust pixels are identified correctly except some missing pixels which have relatively low intensity. Since the quality of MODIS AOD products is not good enough for validating products in sample areas, measurements of multiple other sensors operated in the A-train orbit are selected for quantitative validation. Validated with OMI UVAI product, most smoke plumes are detected accurately. One main factor impacting the accuracy of algorithm may attribute to the spatial resolution difference between two sensors. The validation of dust aerosol monitoring with CALIPSO VFM product is also performed. More than 90% dust aerosol pixels are identified correctly in the select case. Although there are some pixels misclassified, most of them concentrate at the edge of dust storm with light dust aerosol loading. The algorithm also works well in the areas close to cloud or mixed with cloud. On the other hand, the deficiency of detecting small smoke aerosol by MODIS is found by comparing with ASTER and Hyperion measurements.

Since both CALIPSO and Aqua MODIS are operated in the A-train orbit with similar local equatorial crossing time, a simple approach is developed to detect dust aerosols combing their measurements. The MODIS BTD (12, 11) is an effective index that can be used for differentiating dust aerosol and cloud in both day and night time. After spatial registration, the overlapped areas are divided into two categories according to MODIS BTD (12, 11) values. With the comparison between measurements of two sensors, if a aerosol layer is labeled as cloud in CALIPSO VFM product it located in the area having positive BTD (12, 11μm) values, it is corrected and identified as dust aerosol.

Based on the detection results, the vertical and horizontal information about several dust aerosols occurred in 2008 spring season are summarized.

The MODIS spatial characterization with the SRCA and ground target approach is introduced and the impact of BBR shift, or mis-registration, on MODIS L1B measurements and dust aerosol detection is assessed. The impacts on L1B are generally small and are different in both directions due to the strong bow-tie effect in scan directions. The largest relative error of all RSBs in Aqua MODIS is less than 0.1% in the select case, which is negligible in real applications. The theoretical analysis shows that the influence of mis-registration on dust detection is larger than on L1B measurements. The influence on dust aerosol detection results is small at the homogenous or semi-homogenous areas but relative large at the mixed areas. The increase of correlation coefficient demonstrates that the quality of science data product can be improved by shifting a pixel in track direction. This study provides valuable information for the sensors without spatial characterization capability and also for the specification design of future sensors.

8.2 Limitations

This dissertation is executed in some limited condition due to the data availability in time and space. In the absence of suitable laboratory and field data, such as the spectral curves of the smoke, some results are thus mainly based on the model simulation and limited available datasets. Statistical analysis of the training data is a primary ways in this research to achieve the desired spectral features of the smoke/dust. Although the

statistical can provide reasonable results, its accuracy depends on the number of training data. Moreover, the thresholds used in the algorithm are usually site-specific, which limit the application of the algorithm.

One of the significant achievements of this dissertation is to assess the impacts on the L1B measurements and corresponding science data products caused by the instrument itself. However, only the influence from the spatial characterization change is performed in this dissertation. It is very beneficial to estimate the impacts from all three kinds of characterization changes.

8.3 Future Works

The approach for detecting smoke and dust aerosol with satellite remote sensing could be enhanced with further studies. Recommendations for future researches fall into four categories, showing as follow:

1) Adding more precise site-specific information. Currently, the surface is only separated into land and ocean for smoke detection, and divided into dark and bright surface for dust storm monitoring. The more strict classification of surface features and site-specific thresholds can enhance the accuracy of algorithm significantly. It is very valuable to build up a lookup table to store the site-specific thresholds for whole global.

2) Enhancing the algorithm by using multi-sensor measurements. In this dissertation, only CALIPSO and MODIS are combined for dust detection. Integrating more sensors can enhance the detection approach and improve the detection accuracy.

3) Validating aerosol detection quantitatively with ASTER measurements and ground measurements. Since ASTER instrument is boarded on the Terra spacecraft, same platform as MODIS, it can provide more rigorously quantitative validation. Additionally, the sunphotometer offers trustable ground measurements for validation.

4) Assessing the impact of sensor radiometric and spectral characterization on aerosol detection. After a long term operation in its orbit, the radiometric and spectral characterization of instrument may have small changes which could cause uncertainties on L1B data and consequently on science data products. Sensitivity analysis helps us understand more about the impact from instrument itself.

On the other hand, some useful researches need to be implemented based on this dissertation in near future include: 1) tentative retrieving the AOD based on the detection results; 2) gathering the smoke/dust information in a long time range. With long term aerosol information, it is feasible to analyzing their distribution, the motion, height, and width, even the seasonal variation.

REFERENCES

REFERENCES

Ackerman, S. A., 1989, Using the radiative temperature difference at 3.7 and 11 μm to track dust outbreaks, *Remote Sensing Environment*, vol.27, 129-133.

Ackerman, S. A., 1997, Remote Sensing aerosols using satellite infrared observation, *Journal of Geophysical Research*, vol.102, 17069-17079.

Ackerman, S., Strabala, K., Menzel, P., Frey, R., Moeller, C., Gumley, L., Baum, B., Seeman, S.W., and Zhang, H., 2002, Discriminating Clear-sky from cloud with MODIS, *MODIS Algorithm Theoretical Basis Document (MOD35)*: NASA, Version 4.0.

Ahmad, S. P., Levelt, P. F., Bhartia, P. K., Hilsenrath, E., Leppelmeierd, G. W., and Johnson. J. E., 2003, Atmospheric products from the ozone monitoring instrument (OMI). *Proceedings of SPIE*, vol. 5151, 619-630.

Austin, C. C., Goyer, N., 2007, Respiratory protection for wildland firefighters – Much ado about nothing or time to revisit accepted thinking?, post session, Wildfire, Sevilla, Espana.

Barbieri, R., H.Montgomery, S. Qiu, B.Barnes, B. Guenther, and V. V., Salomonson, 1997, Draft of the MODIS Level 1B Algorithm Theoretical Basis Document, Version 2.0.

Barnes, W. L., Xiong, X., and Salomonson, V. V., 2002, Status of Terra MODIS and Aqua MODIS, Geoscience and Remote Sensing Symposium, *Proceedings of IGARSS*, vol. 2, No. 24-28, 970-972.

Baum, B. A., and Trepte, Q., 1999, A grouped threshold approach for scene identification in AVHRR imagery, *Journal of Atmospheric and Oceanic Technology,* vol.16, 793–800.

Carlson, T. N., 1978, Atmospheric turbidity in Saharan Dust Outbreaks as Determined by Analyses of Satellite Brightness Data, *Monthly Weather Review*, vol. 107, 322-335.

Cavtenet, G., Legrand, M., Cautene, S., Bonnel, B., and Brognie, G., 1992, Thermal Impact of Saharan Dust Land. Part I: Simulation, *Journal of applied meteorology*, vol. 31, 166-180.

Che, N., Xiong, X., Guenther, B., Barnes, W. L., Salomonson, V. V., 2005, Five years of Terra MODIS on-orbit spatial characterization, *Proceedings of SPIE*, vol. 5882, 58821A.

Christopher, S. A., Kliche, D.V., Chou, J. and Welch, R. M., 1996, First estimates of the radiative forcing of aerosols generated from biomass burning using satellite data, *Journal of Geophysical Research*, vol. 101, 21265-21273.

Christopher, S. A. and Chou, J. 1997, The potential for collocated AGLP and ERBE data for fire, smoke and radiation budget studies, *International Journal of Remote Sensing*, vol.18, 2657-2676.

Chrysoulakis, N. and Opie, C., 2004, Using NOAA and FY imagery to track plumes caused by 2003 bombing of Baghdad, *International Journal of Remote Sensing*, vol.25, 5247-5254.

Chrysoulakis, N., and Cartalis, C., 2003, A new algorithm for the detection of plumes caused by industrial accidents, based on NOAA/AVHRR imagery, *International Journal of Remote Sensing*, vol.24, 3353-3367.

Chrysoulakis, N., Herlin, I., Prastacos, P., Yahia, H., Grazzini, J., Cartalis, C., 2007, An improved algorithm for the detection of plumes caused by natural or technological hazards using AVHRR imagery, *Remote Sensing of Environment*, vol. 108, 393-406.

Chu, D. A., Kaufman, Y. J., Chern, J. D., Mao, J.M., Li, C., and Holben, B. N., 2003, Global monitoring of air pollution over land from EOS Terra MODIS, *Journal of Geophysical Research*, vol. 108, No. D21, 4661.

Chung, Y. S., aand Le, H.V., 1984, Detection of forest-fire smoke plumes by satellite

imagery, *Atmospheric Environment*, vol.18, 2143-2151.

Currey. J. C., Anselmo, T., Clifton, R., Hunt, W., Lee, K. P., Murray, T., Powell, K., Rodier, S. D., Vaugham, M., Chomette, O., Viollier, M., Hagolle, O., Lifermann, A., Garnier A., Pelon, J., Pitts, M., Winker, D., 2007, Cloud-aerosol LIDAR infrared pathfinder satellite observations-data management system and data products catalog, ATBD, document NO: PC-SCI-503.

Dunion, J. P., and Velden, C. S., 2004, The impact of the Saharan air layer on Atlantic tropical cyclone activity, *Bulletin of American Meteorological Society*, vol. 85, 353-365.

Eatelles, V., Martinez-Lozano, J. A,, Utrillas, M. P., and Campanelli, M., 2007, Columnar aerosol properties in Valencia by ground-based Sun photometry, *Journal of Geophysical Research*, vol. 112, D11201.

El-Askary, H.; Kafatos, M., Xue, L., El-Ghazawi, T., 2003, Introducing new approaches for dust storms detection using remote sensing technology, *Geoscience and Remote Sensing Symposium, Proceedings of IGARSS, IEEE International*, vol. 4, No. 21-25, 2439-2441.

Esaias, W. E., Abbott, M. R., Barton, I., Brown, O. W., Campbell, J. W., Carder, K. L., Clark, D. K., Evans, R. L., Hoge, F. E., Gordon, H. R., Balch, W. P., Letelier, R., and Minnett, P. J., 1998, An overview of MODIS capabilities for ocean science observations, *IEEE Transactions on Geoscience and Remote Sensing*, vol.36, 1250-1265.

Gao, B. C., Goetz, A. F. H., and Wiscombe, W. J., 1993, Cirrus cloud detection from airborne imaging spectrometer data using the 1.38 μm water vapor band, *Geophysical Research Letters*, vol. 20, No. 4, 301-304.

Gao, B. C., 1996, NDWI – A Normalized Difference Water Index for Remote Sensing of Vegetation Liquid Water from Space, *Remote Sensing of Environment*, vol. 58, 257-266.

Gao, B. C., Yang, P., Han, W., Li, R., and Wiscomber, W. J., 2002, An Algorithm Using Visible and 1.38 μm Channels to Retrieve Cirrus Cloud Reflectance from Aircraft and Satellite Data, *IEEE Transactions on Geoscience and Remote Sensing*, vol. 40,

1659-1668.

Hall, D. K., Riggs, G. A., Salomonson, V. V., Giromamo, N. D., and Bayr, K. J., 2002, MODIS snow-cover products, *Remote Sensing of Environment*, vol. 83, 181-194.

Han, T., Li, Y., Han, H., Zhang, Y., and Wang, Y., 2005, Automatic detection of dust storm in the northwest of China using decision tree classifier based on MODIS visible bands data, *Geoscience and Remote Sensing Symposium, Proceedings of IGARSS, IEEE International*, vol. 5, NO. 25-29, 3603-3606.

Hao, X., Qu, J. J., 2007, Saharan dust storm detection using MODIS thermal infrared bands, *Journal of Applied Remote Sensing*, vol. 1, 013510.

Herman, J. R., Bhartia, P. K., Torres, O. et al., 1997, Global distribution of UV-absorbing aerosols from Nimbus7/TOMS data, *Journal of Geophysical Research*, vol. 102, 911-922

Hsu, N. C., Tsay, S.-C., King, M. D., and Herman, J. R., 2004, Aerosol properties over bright-reflecting source regions, *IEEE Transactions on Geoscience and Remote Sensing*, vol. 42, 557-569.

Huang, S., and Siegert, F., 2004, ENVISAT multisensor data for fire monitoring and impact Assessment, *International Journal of Remote Sensing*, vol. 25, 4411-4416.

Huete, A., Justice, C., and Liu, H., 1994, Development of vegetation and soil indices for MODIS-EOS, *Remote Sensing of Environment*, vol. 49, 224-234.

InciWeb: Ranch Fire Wildland Fire, InciWeb Incident Information System.

Isaacman, A., Toller, G., Guenther, B., Barnes, W. L., and Xiong, X., 2003, MODIS Level 1B Calibration and Data Products, *Proceedings of SPIE*, vol. 5151, 552-562.

James, T. K., Chuang, C. C., and Anthony, S. W., 2007, Influence of dust composition on cloud droplet formation, *Atmospheric Environment*, vol.41, No. 14, 2904-2916.

Justice, C. O., Vermote, E., Townshend, J. R. G., Defries, R., Roy, D. P., Hall, D. K.,

Salomonson, V. V., Privette, J. L., Riggs, G., Strahler, A., Lucht, W., Myneni, R. B., Lewis, P., and Barnsley, M. J., 1998, The Moderate Resolution Imaging Spectroradiometer (MODIS): Land remote sensing for global change research, *IEEE Transactions on Geoscience and Remote Sensing*, vol.36, 1228-1249.

Kaufman, Y. J., Tucker, C. J., and Fung, I., 1990, Remote sensing of biomass burning in the tropics, *Journal of Geophysical Research*, vol. 95, 9927-9939.

Kaufman, Y. J., Wald, A. E., Remer, L. A., Gao, B. C., Li, R. R., and Flynn, L. , 1997, The MODIS 2.1μm channel—Correlation with visible reflectance for use in remote sensing of aerosol, *IEEE Transactions on Geoscience and Remote Sensing*, vol. 35, No. 5, 1286-1298.

Kaufman, Y. J., Tanré, D., Remer, L. A., Vermote, E. F., Chu, D. A., and Holben, B. N., 1997, Operational remote sensing of tropospheric aerosol over land from EOS Moderate Resolution Imaging Spectroradiometer, *Journal of Geophysical Research*, vol. 102, No. D14, 17051-17067.

Kaufman, Y. J., Ichoku, C., Giglio, L., Korontzi, S., Chu, D. A., Hao, W. M., Li, R. R., and Justice, C. O., 2003, Fire and smoke observed from the Earth Observing System MODIS instrument—products, validation, and operational use, *International Journal of Remote Sensing*, vol.24, No. 8, 1765-1781.

Kaufman, Y. J., and Fraser, R. H., 1997, The effect of smoke particles on clouds and climate forcing, *Science*, vol.277, 1636-1639.

King, M. D., Menzel, W. P., Kaufman, Y. J., Tanre, D., Gao, B. C., Platnick, S., Ackerman, S. A., Remer, L. A., Pincus, R., and Hubanks, P. A., 2003, Cloud and aerosol properties, precipitable water, and profiles of temperature and water vapor from MODIS, *IEEE Transactions on Geoscience and Remote Sensing*, vol.41, 442-458.

Legrand, M., Desbois, M. and Vovor, K., 1987, Satellite Detection of Saharan Dust：Optimized Imaging during Nighttime, *Journal of Climate*, vol. 1, 256-264.

Legrand, M., Bertrand, J. J., Desbois, M., Menenger, L., and Fouquart, Y., 1989, The Potential of Infrared Satellite Data for the Retrieval of Sahara-Dust Optical Depth over Africa, *Journal of Applied Meteorology*, vol. 28, 309-319.

130

Legrand, M., Cautenet, G. and Burie, J. C., 1992, Thermal Impact of Saharan Dust over Land. Part 11: Application to Satellite IR Remote Sensing, *Journal of Applied Meteorology*, vol.31, 181-193.

Legrand, M., Plana-Fattori, A. and N'doumé, C., 2001, Satellite detection of dust using the IR imagery of Meteosat: 1. Infrared difference dust index, *Journal of Geophysical Research*, vol.106, No. D16, 18,251-18,274.

Levelt, P. F., Van Den Oord, B., Hilsenrath, E., Stammes, P., Kelder, H., Van Der A, R., 2000, Science Objectives of EOS-AURA's Ozone Monitoring Instrument (OMI), *Proceedings of the Quadrennial Ozone Symposium*, 127-128.

Levelt, P. F., van den Oord, G. H. J., Dobber, M. R., Malkki, A., Visser, H., de Vries, J., Stammes, P., Lundell J. O. V., and Saari, H., 2006, The Ozone Monitoring Instrument, *IEEE Transactions on Geoscience and Remote Sensing*, vol. 44, No. 5, 1093-1101.

Li, Z., 1998, Influence of absorbing aerosols on the inference of solar surface radiation budget and cloud absorption, *Journal of Climate*, vol. 11, 5-17.

Li, Z., Khananian, A., Fraser, R. H., Cihlar, J., 2001, Automatic Detection of Fire Smoke Using Artificial Neural Networks and Threshold Approaches Applied to AVHRR Imagery, *IEEE Transactions on Geoscience and Remote Sensing*, vol. 39, 1859-1870.

Liou, K.N., An introduction to Atmospheric Radiation, second edition, Chapter 7, Elsevier Science (USA), 2002.

Liu, Z., Vaughan, M., Winker, D., Hostetler, C.A., Poole, L. R., Hlavka, D. L., Hart, W.D., McGill, M. J., 2004, Use of probability distribution functions for discriminating between cloud and aerosol in lidar backscatter data, *Journal of Geophysical Research*, vol. 109, D15202.

Livingston, J., Redemann, J., Russell, P., Johnson, R., Zhang, Q., Remer, L., Kahn, R., Torres, O., Smirnov, A., Holben, B., 2007, Comparison of Airborne Sunphotometer and Satellite Sensor Retrievals of Aerosol Optical Depth during MILAGRO/INTEX-B, *Geophysical Research Abstracts*, vol. 9, 04687.

Martinez, A., and Gros, G., 2007-10-22, Witch fire roars west across Rancho Bernardo and Poway, SignOnSanDiego.com, San Diego Union Tribune. http://www.signonsandiego.com/news/metro/20071022-0934-bn22fire3new.html

Miller, S. D., 2003, A consolidated technique for enhancing desert dust storms with MODIS, *Journal of Geophysical Research Letter*, vol.30, 2071-2074.

Montgomery, H., Che, N., Bowser, J., 2000, Determination of MODIS Band-to-band Co-registration On-orbit Using the SRCA, *Geoscience and Remote Sensing Symposium, IGARSS international*, vol. 5, 2203-2205.

Nelson, N. R., Barry, P. S., 2001, Measurement of Hyperion MTF from On-Orbit Scenes, *Proceedings of IGARSS*, vol. 7, 2967-2969.

Nishihama, M., Wolfe, R. E., Fleig, A. J., Blanchette, J., and Kuyper, J., 2000, MODIS Geolocation Algorithm and Error Analysis Tools, *Geoscience and Remote Sensing Symposium,IEEE international*, vol. 5, 2053-2055.

Norton, C. C., Mosher, F. R., Hinton, B., Martin, D. W., Santek, D. and Kuhlow, W, 1980, A Model for Calculating Desert Aerosol Turbidity over the Oceans from Geostationary Satellite Data, *Journal of Applied Meteorology*, vol. 19, 633-644.

Parkinson, C. L., 2003, Aqua: An Earth-Observing Satellite mission to examine water and other climate variables, *IEEE Transactions on Geoscience and Remote Sensing*, vol.41, 173–183.

Qu, J. J., Hao, X., Kafatos, M., and Wang, L., 2006, Asian Dust Storm Monitoring Combining Terra and Aqua MODIS SRB Measurements, *IEEE Geoscience and Remote Sensing Letter*, vol. 3, No. 4, 484-486, Front Cover.

Randriambelo, T., Baldy, S., Bessafi, M., Petit, M. and Despinoy, M., 1998, An improved detection and characterization of active fires and smoke plumes in south-eastern Africa and Madagascar, *International Journal of Remote Sensing*, vol.19, 2623-2638.

Remer, L. A., Tanre, D., Kaufman, Y. J., Ichoku, C., Mattoo, S., Levy, R., Chu, D. A., Holben, B., Dubovik, O., Smirnov, A., Martins, J. V., Li, R. R., and Ahmad, Z.,

2002, Validation of MODIS aerosol retrieval over ocean, *Geophysical Research Letter*, vol. 29, No.12, 8008.

Rouse, J. W., Haas, R. H., Schell, J. A., and Deering, D. W., 1973, Monitoring vegetation systems in the Great Plains with ERTS, 3rd ERTS Symp. NASA SP-351 I, 309-317.

Salomonson, V. V., Barnes, W. L., Xiong, X., Kempler, S. and Masuoka, E., 2002, An Overview of the Earth Observing System MODIS Instrument and Associated Data Systems Performance, Geoscience and Remote Sensing Symposium, *Proceedings of IGARSS*, vol. 2, 1174-1176.

Schowengerdt, R. A., Basedow, R. W., and Colwell, J. E., 1996, Measurement of the HYDICE System MTF from Flight Imagery, *Proceedings of SPIE*, vol. 2821, 127-136.

Schowengerdt, R. A., 2002, Spatial response of the EO-1 Advanced Land Imager (ALI), *Proceedings of IGARSS*, vol. 1, 9-13.

Storey, J., 2001, Landsat 7 on-orbit modulation transfer function estimation, *Proceedings of SPIE*, vol. 4540, 50-61.

Torres, O., Tanskanen, A., Veihelmann, B., Ahn, C., Braak, R., Bhartia, P.K., Veefkind, J.P., Levelt, P.F., 2007, Aerosols and surface UV products from ozone monitoring instrument observations: an overview, *Journal of Geophysical Research*, vol. 112, D24S47.

Trovinkere, V. R., Penaloza, M., Logar, A., Lee, J., Weger, R., BERENDES, T. A., and WELCH, R. M., 1993, An intercomparison of artificial intelligence approaches for polar scene identification, *Journal of Geophysical Research*, vol.98, 5001-5016.

Wang, L., Xiong, X., Qu, J. J., Xie, Y., Hao, X., and Che, N., 2007, Impact Assessment of Aqua MODIS Band-to-band Misregistration on Snow Index, *Journal of Applied Remote Sensing*, vol. 1, 013531.

Wang, L., J. J. Qu, 2007, NDMI: A Normalized Multi-band Drought Index for Monitoring Soil and Vegetation Moisture with Satellite Remote Sensing, *Geophysical Research Letters*, vol. 32, L20405.

Wang W., Qu, J. J., Liu, Y., Hao, X., and Sommers, W., 2007, An Improved Algorithm for Small and Cool Fire Detection Using MODIS Data: a preliminary study in the southeastern United States, *Remote sensing of Environment*, vol. 108, No.2, 163-170.

Welch, R. H., Sengupta, S. K., and Chen, D. W., 1988, Cloud field classification based upon high spatial resolution textural features. Part I: Gray level concurrence matrix approach, *Journal of Geophysical Research*, vol. 93, 12663-12681.

Winker, D. M., Pelon, J., McCormick, M. P., 2003, The CALIPSO mission: spaceborne lidar for observation of aerosols and clouds, *Proceedings of SPIE*, vol. 4893, 1–11.

Wolfe, R. E., Nishihama, M., Fleig, A. J., Kuyper, J. A., Roy, D. P., Storey, J. C., and Patt, F. S., 2002, Achieving Sub-pixel Geolocation Accuracy in Support of MODIS Land Science, *Remote Sensing of Environment*, vol. 83, 31-49.

Wong, J., Li, Z., Retrieval of optical depth for heavy smoke aerosol plumes: uncertainties and sensitivities to the optical properties, *Journal of Atmospheric Science*, vol. 59, No.3, 250-261.

Wu, L., Braun, S. A., Qu, J. J., and Hao, X., 2006, Simulating the formation of Hurricane Isabel with AIRS data, *Geophysical Research Letter*, vol.33, No. 4, L04804.

Xie, Y., Xiong, X., Qu, J. J., Che, N., Wang, L., 2006, MODIS on-orbit spatial characterization results using ground measurements, *Proceedings of SPIE*, vol.6296, 62961L.

Xie, Y., Qu, J. J., Xiong, X., Hao, X., Che, N., and Sommers, W., 2007, Smoke plume detection in the eastern United States using MODIS, *International Journal of Remote Sensing*, vol. 28, 2367-2374.

Xie, Y., Xiong, J., Qu, J. J., Che, N., and Wang, L., 2007, Sensitivity Analysis of MODIS Band-to-Band Registration Characterization and Its Impact on the Science Data Products, *Proceedings of SPIE*, vol. 6679, 6679E.

Xie, Y, Xiong, X., Qu, J. J., Che, N., and Wang, L., 2008, MODIS On-Orbit Spatial Characterization with Ground targets, *IEEE Transactions on Geoscience and*

Remote Sensing, vol. 46, issue 9, 2666-2674.

Xiong, X., K. Chiang, J. Esposito, B. Guenther, W. L. Barnes, 2003, MODIS on-orbit calibration and characterization, *Metrologia*, vol 40, s89-s92.

Xiong, X., Che, N., Barnes, W., 2005, Terra MODIS on-orbit spatial characterization and performance, *IEEE Transaction on Geoscience and Remote Sensing*, vol. 43, no. 2, 355-365.

Xiong, X., Che, N., Barnes, W., Xie, Y. Wang, L., and Qu, J. J., 2006, Status of Aqua MODIS Spatial Characterization and Performance, *Proceeding of SPIE*, vol.6361, 63610T.

CURRICULUM VITAE

Yong Xie is a Ph.D. candidate in George Mason University (GMU), majored in Geography and Geoinformation Sciences. He received the M.S. degree in Physics Electronics from NanJing Normal University (NJNU), NanJing, China, in 2004. He is currently working on aerosol and hazard related researches at the EastFIRE Lab in GMU, Fairfax, VA, and on instrument calibration and characterization of EOS Terra/Aqua MODIS with the MODIS Calibration Support Team (MCST). Before he focused on remote sensing, he had also worked in the field of physics, electric circuit design, and multi-layered waveguide memory in NJNU.